

分 类 号\_\_\_\_\_

学号\_\_\_\_\_D201277241\_\_\_\_\_

学校代码\_\_\_\_\_10487\_\_\_\_\_

密级\_\_\_\_\_

# 华中科技大学

# 博士学位论文

## 太阳能光热梯级发电系统设计 及其特性研究

学位申请人： 张成

学 科 专 业： 热能工程

指 导 教 师： 高伟 教授

Inmaculada Arauzo 教授

张燕平 副教授

答 辩 日 期： 2017 年 9 月 1 日

A Thesis Submitted in Partial Fulfillment of the  
Requirements for the Ph.D

Cascade solar thermal power system design and research  
of the key features

Student : Cheng Zhang

Major : Thermal Engineering

Supervisor : Prof. Wei Gao

Prof. Inmaculada Arauzo

Associate Prof. Yanping Zhang

**Huazhong University of Science & Technology**

**Wuhan 430074, P. R. China**

**September 1, 2017**

## 独创性声明

本人声明所呈交的学位论文是我个人在导师的指导下进行的研究工作及取得的研究成果。尽我所知,除文中已标明引用的内容外,本论文不包含任何其他人或集体已经发表或撰写过的研究成果。对本文的研究做出贡献的个人和集体,均已在文中以明确方式标明。本人完全意识到本声明的法律结果由本人承担。

学位论文作者签名:

日期: 年 月 日

## 学位论文版权使用授权书

本学位论文作者完全了解学校有关保留、使用学位论文的规定,即:学校有权保留并向国家有关部门或机构送交论文的复印件和电子版,允许论文被查阅和借阅。本人授权华中科技大学可以将本学位论文的全部或部分内容编入有关数据库进行检索,可以采用影印、缩印或扫描等复制手段保存和汇编本学位论文。

本论文属于 ☐ 保密,在 \_\_\_\_ 年解密后适用本授权书。  
☐ 不保密。

(请在以上方框内打“√”)

学位论文作者签名:

日期: 年 月 日

指导教师签名:

日期: 年 月 日

## 摘要

随着化石能源的消耗和环境问题的凸显,太阳能作为一种新能源,具有分布广泛、总量巨大、取之不竭、无污染的特点,越来越受到世界各国的重视,被广泛认为是未来最有潜力替代传统化石能源的清洁能源。在发电领域,太阳能光热发电是除了太阳能光伏发电之外的另一种发电形式。与光伏发电相比,光热发电因具有发电平稳,电网兼容性友好,易于与现有化石燃料电厂组合等优点而受到越来越多的关注。已经商业应用的太阳能光热发电技术分为槽式集热发电、碟式集热发电和塔式集热发电三种。三种发电技术各有优缺点:槽式集热发电应用最广,成本较低,但效率也较低;碟式集热发电规模较小,多用于分布式发电;塔式集热发电规模较大,成本较高,目前处于快速发展阶段。综合利用现有发电技术的优缺点,在能量梯级收集和能量梯级利用的思想下,提出采用多种集热发电方式和多种热功循环的梯级系统,是实现大规模太阳能光热发电的一种新颖的可行的技术方案。

本课题以国家国际合作项目专项“太阳能梯级集热发电系统关键技术合作研究”为背景,目标是研究太阳能光热发电装置,利用各种传统型式的太阳能光热发电系统的优缺点以及热力特性,提出并组建、优化太阳能梯级集热发电系统,为探索出可大规模高效率利用太阳能的光热发电技术提供新的方案。主要研究内容和结论包括:

首先,提出太阳能光热梯级集热发电系统的拓扑结构。通过热力特性分析,结合系统中各部件的工作特点,合理布局太阳能光热梯级集热发电系统,利用不同热功循环实现不同品位的能量的梯级利用。合理的梯级发电系统方案才能充分利用发电系统中各部件的性能特点,为创建高效率的太阳能光热梯级发电系统提供基础。本文针对系统中的各组件,组建了多种可行的梯级集热系统拓扑结构。经过系统评估、参数选取、初步计算、方案比较,确定了两种具有代表性的太阳能光热梯级发电系统方案。一种方案同时选用水工质朗肯循环和斯特林循环,利用给水来冷却斯特林机冷腔,回收利用斯特林机放出的热量;另一种方案选用多级有机工质朗肯循环,利用上一级的凝集热来加热下一级的循环工质,实现能量的梯级利用。

其次,针对太阳能光热梯级集热发电系统的各部件建立机理模型。依据目标对象的运行机理,根据物理平衡方程,对系统中的各部件,尤其是系统中的关键部件,如集热器、蒸汽产生系统、汽轮机、斯特林机等,建立起数学模型。各部件的数学模型是由经典理论或是大量实验数据验证的模型,是组建光热梯级集热发电系统模型的基础。对于槽式集热器的集热管和碟式集热器的集热器,建立了热损失模型;对于斯特林机,基于合理的简化和假设,推导出了考虑了各种热损失和不可逆因素的斯特林机

模型。各部件模型使用 **MATLAB** 语言编写,采用面向对象的方法,充分利用了继承、多态等特性,保证了各部件之间既具有独立性又具有关联性。

再次,组建太阳能光热梯级集热发电系统模型。根据所选择的太阳能光热梯级发电系统方案,基于建立好的系统中各部件的模型,利用面向对象语言的继承、组合、多态等特点,组建起梯级集热发电系统模型。研究系统在外部的耦合作用下主要参数及性能指标的变化规律,掌握其变化机理,建立其性能特性的计算方法。经过组建部件,设置参数,编译环境,完成了各系统方案的系统组建工作,最终完成了拥有自主计算机软件著作权的基于 **MATLAB** 的太阳能光热梯级发电的模拟系统。系统中各部件相对独立,便于更换或改进部件模型;各系统模型的计算结果可以以单个对象的方式方便地查看系统中各个部件的关键参数。

然后,模拟并优化太阳能光热梯级集热发电系统模型。在太阳能光热梯级发电系统性能特性研究的基础上,对系统进行流程优化、结构重构。具体地,通过对系统的蒸汽发生系统进行分析,提出了分阶段加热方法,通过改变导热油的质量流量降低蒸汽发生系统中的传热温差,有效降低了蒸汽发生系统中换热过程中产生的烟损,进而可以提高整个系统的效率。针对梯级系统中的斯特林机组,总结了斯特林机组所具有的五种基本排列形式,并分析了各种排列形式下机组的效率和输出功率的差异,得到了给定冷热源流体条件下斯特林机组最佳的排列方式。

最后,优化太阳能光热梯级集热发电系统的运行参数。针对特定结构方案和运行模式,以梯级发电系统的性能参数和经济指标为目标函数,选择合理的可调节参数,确立各种约束条件,利用现代优化方法,如基因算法、蚁群算法,完成系统的参数优化分析,以及对于独立系统的对比分析。分析结果表明,太阳能光热梯级集热发电系统在一定的参数条件下,相比其对应的独立系统,具有更高的总体光电转换效率。在太阳直射强度为  $700 \text{ W/m}^2$ ,碟式集热器出口空气温度为  $800^\circ\text{C}$  的条件下,方案 1 所选用的太阳能光热梯级集热发电系统比对应的独立系统效率提升 5.2%,方案 2 所选用的太阳能光热梯级集热发电系统比对应的独立系统效率提升 15.3%。

**关键词：** 槽式集热器,碟式集热器,朗肯循环,斯特林循环,斯特林机组,梯级发电

## Abstract

With the increasing awareness of problem of fossil energy consumption and environmental pollution, solar energy as a renewable energy, which has the advantages of widely distribution, huge amount, inexhaustible and no pollution, has received much attention by many countries and been regarded as the best potential candidate of the fossil energy. Concentrating solar thermal power generation is another form of power generation technology except solar photovoltaic power generation. Compared to solar photovoltaic, solar thermal power is gaining more attention for its advantages as smooth power generation, good grid compatibility, easy to integrate with existing fossil power plant.

Commercial solar thermal power generation technology is divided into trough collector power generation, dish collector power generation and solar tower power generation. These three types of power generation technologies have their own advantages and disadvantages: trough collector power generation is the most widely used one, its cost is low, however its efficiency is also low; dish collector power generation has high efficiency and smaller capacity, it is used for distributed generation widely; solar tower generation, which has large scales, high efficiency and high cost, is currently in rapid development stage. Based on the idea of energy cascade collection and energy cascade utilization, this paper proposed a cascade system that uses different collector power generation methods and different thermodynamic cycles, which may be a new and feasible technology to realize large-scale solar thermal power generation.

The research is based on the national cooperation project "Collaborative research on key technologies to produce electricity by cascade utilization solar thermal energy" as the background. The objective of this project is to research the equipment of solar thermal power generation system, to propose, develop and optimize a solar thermal cascade system depending on the advantages and disadvantages of the solar thermal power generation system, and to explore a new feasible technology for large-scale solar thermal power generation. The main contents and conclusions of this paper are as follows:

Firstly, the topological structure of solar thermal cascade power generation system was proposed. According to the analysis of thermal characteristics and the working characteristics of each component in the system, rationally arranged topological structures of cascade system were proposed. These systems use different thermodynamic cycles to utilize energy

in different temperature zones. A reasonable cascade generation system can make full use the performance characteristics of the components in the power generation system and provide the foundation for higher efficiency solar thermal cascade generation systems. In this paper, several schemes of feasible topological structures of solar thermal cascade system were set up according to the components in the system. After system evaluation, parameter selection, preliminary calculation and scheme comparison, two representative typical schemes were determined. In one scheme, both Rankine cycle (water as the working fluid) and Stirling cycle are used for power generation. Cooling water of the Rankine cycle is used to cool the hot end of the Stirling engines to recover the released heat. In the other scheme, multiple organic Rankine cycles are used for power generation. Condensation heat of upper cycle is absorbed by lower cycle for energy cascade utilization.

Secondly, mechanism models were established for the components of solar thermal power generation system. The mechanism mathematical models were developed according to the operation mechanism of the target object and physical equations. The key components in the system, such as collectors, steam generating system, steam turbine and Stirling engine, were modeled with details. The mathematical model of each component is a model verified by the classical theory or a large number of experimental data, which is the basic of the model of the cascade solar thermal power generation system. Heat loss models were established for the receivers of trough collector and dish collector. For the Stirling engine, based on the reasonable simplification and hypothesis, the model of the Stirling machine considered various losses and irreversibilities was developed. The component models were developed in MATLAB by using object-oriented method. It makes full use of inheritance and polymorphism to ensure both the independence and the relevance of the components.

Thirdly, the solar thermal cascade generation system models were developed. Based on the selected solar thermal cascade generation systems, solar thermal cascade generation system models were established based on the model of each component in the systems. The object-oriented features of inheritance, combination and polymorphism were used for the model development. The change rules of the main parameters and the performance indexes under the coupling of external and internal factors were studied. The change mechanism was studied and the calculation method of its performance characteristics was established. After setting up the components, setting the parameters and compiling the environment, the paper completes the system construction of each system scheme, and finally completes the simulation system of solar thermal cascade generation based on MATLAB with the copyright of independent computer software. The system components are relatively independent, easy

to replace or improve the parts model; the results of the calculation of the system model can be a single object to easily view the various components of the system key parameters.

Then, simulation and optimization of cascade solar thermal power generation system model. Based on the study of the performance characteristics of solar thermal cascade generation system, the system is optimized and the structure is reconstructed. In particular, by analyzing the steam generation system of the system, a method of staged heating is proposed to reduce the heat transfer temperature difference in the steam generating system by changing the mass flow rate of the heat conduction oil, effectively reducing the heat generated during the heat exchange process in the steam generating system. Which can improve the efficiency of the whole system. Based on Stirling unit in cascade system, five kinds of basic arrangement forms of Stirling unit are summarized, and the difference of unit efficiency and output power under various arrangement forms is analyzed, and a given cold and heat source fluid Stirling unit under the conditions of the best arrangement.

Finally, the operating parameters of solar thermal cascade power generation system are optimized. According to the specific structural scheme and operation mode, the performance parameters and economic indexes of the cascade generation system are taken as the objective function, reasonable adjustable parameters are selected, various constraints are established, and modern optimization methods such as genetic algorithm and ant colony algorithm are used to complete the system Parameter optimization analysis, as well as the independent system for comparative analysis. The results show that solar thermal cascade power generation system has higher overall photoelectric conversion efficiency under certain parameter conditions than its corresponding independent system. Under the condition of direct solar radiation intensity of  $700 \text{ W/m}^2$  and dish type collector outlet air temperature of  $800^\circ\text{C}$ , the solar thermal cascade power generation system of Scheme 1 is better than the corresponding The efficiency of stand-alone system is increased by 5.2%. The solar thermal cascade power generation system selected in Scheme 2 is 15.3% more efficient than the corresponding independent system.

**Key words:** parabolic trough collector, parabolic dish collector, Rankine cycle, Stirling cycle, Stirling engine array, cascade powering



## Contents

<b>Abstract</b>	<b>I</b>
<b>List of Figures</b>	<b>IX</b>
<b>List of Tables</b>	<b>XI</b>
<b>1 Introduction</b>	<b>1</b>
1.1 Research background and significance . . . . .	1
1.2 State of the art . . . . .	3
1.3 Research content . . . . .	19
<b>2 System topology</b>	<b>22</b>
2.1 System topology design . . . . .	22
2.2 System topology selection . . . . .	31
<b>3 System modeling</b>	<b>32</b>
3.1 Component modeling . . . . .	32
3.2 Stirling engine array . . . . .	55
3.3 Component connection . . . . .	58
<b>4 Optimization of Stirling engine array</b>	<b>59</b>
4.1 Connection types of SEA . . . . .	59
4.2 Modeling of the SEAs . . . . .	60
4.3 Result Analysis . . . . .	62
4.4 Conclusion . . . . .	67
<b>5 Optimization of steam generating system</b>	<b>70</b>
5.1 Steam generator subsystem . . . . .	70
5.2 Multi-stage exergy loss reduction system . . . . .	72
5.3 Comparison . . . . .	75

<b>6 Cascade system performance evaluation</b>	<b>79</b>
6.1 System description . . . . .	79
6.2 Determination of system parameters . . . . .	81
6.3 System simulation . . . . .	81
6.4 Stand-alone system selection . . . . .	81
6.5 Comparison with stand-alone system . . . . .	82
6.6 System analysis . . . . .	82
<b>7 Conclusion and outlook</b>	<b>83</b>
7.1 Conclusion . . . . .	83
7.2 Innovation . . . . .	83
7.3 Outlook . . . . .	83
<b>Acknowledge</b>	<b>84</b>
<b>Bibliography</b>	<b>85</b>
<b>Appendix A Heat transfer under constant temperature</b>	<b>91</b>
<b>Appendix B Thermal gradient under constant heat flux</b>	<b>93</b>
<b>Appendix C Publication</b>	<b>95</b>

## Nomenclature

### Abbreviations

ANN	Artificial Neural Network
CCHP	Combined cooling, heating and power
CFD	Computational Fluid Dynamics
CRTEn	Research and Technologies Centre of Energy in Borj Cedria
DSG	Direct Steam Generation
HTF	Heat Transfer Fluid
LM	Levenberge Marguardt
LSSVM	Least squares support vector machine
MCRT	Monte Carlo Ray Tracing
ORC	Organic Rankine Cycle
PCG	Pola-Ribiere Conjugate Gradient
PTC	Parabolic Trough Collector
PTSTPP	Parabolic Trough Solar Thermal Power Plant
SCG	Scaled Conjugate Gradient
SNL	Sandia National Laboratory
SPC	Solar parabolic concentrator
SRC	Steam Rankine Cycle

## List of Figures

Figure 1-1	Alpha-Trough-350, a parabolic trough product made by Alpha-E .	3
Figure 1-2	A 38 kW prototype Stirling engine product of XEMC . . . . .	4
Figure 1-3	Overall view of Solar Two power tower . . . . .	5
Figure 2-1	Schematic diagrams of a parabolic trough system and a parabolic dish system . . . . .	22
Figure 2-2	Collector and Rankine cycle efficiency variation with operating temperature . . . . .	23
Figure 2-3	Collector and Rankine cycle efficiency variation with operating temperature . . . . .	24
Figure 2-4	Schematic diagram of a typical steam Rankine cycle solar system	26
Figure 2-5	Schematic diagram of a typical organic Rankine cycle solar system	26
Figure 2-6	Schematic diagram of a solar chimney power plant . . . . .	27
Figure 2-7	Schematic diagram of a combined solar trough and chimney power system . . . . .	28
Figure 2-8	Schematic diagram of a cascade system using collector series connection . . . . .	30
Figure 2-9	schematic diagram of a typical solar system using receiver vapor generator . . . . .	30
Figure 3-1	Some of the optical parameters of a parabolic trough . . . . .	34
Figure 3-2	Schematic diagram of the absorber pipe . . . . .	34
Figure 3-3	The structure of the dish receiver . . . . .	36
Figure 3-4	Thermal network of dish receiver . . . . .	37
Figure 3-5	$T$ - $s$ diagram of a Stirling cycle . . . . .	41
Figure 3-6	An example of steam generating system in a cascade system . . .	50
Figure 3-7	$T$ - $s$ diagram of the water circuit and $h$ - $s$ diagram of the process 2a-2b . . . . .	51
Figure 3-8	$T$ - $s$ diagram of water and a typical organic fluid . . . . .	54

Figure 3-9	The schematic diagram of an ORC system with regenerator . . .	54
Figure 3-10	Layout of Stirling engines . . . . .	56
Figure 3-11	Heat transfer diagram of parallel flow and counterflow . . . . .	56
Figure 3-12	Heat transfer diagram of counterflow . . . . .	57
Figure 4-1	Five basic connection types of SEA . . . . .	60
Figure 4-2	An instance of connection type of an SEA . . . . .	61
Figure 4-3	Influence of $T_{i,h}$ on efficiency and power of SEA . . . . .	64
Figure 4-4	Influence of $q_{m,h}c_{p,h}$ on efficiency and power of SEA . . . . .	65
Figure 4-5	Influence of $q_{m,c}c_{p,c}$ on efficiency and power of SEA . . . . .	66
Figure 4-6	Influence of $n_{se}$ on efficiency and power of SEA . . . . .	68
Figure 5-1	An typical solar parabolic trough system . . . . .	70
Figure 5-2	The steam generating process in countertlow heat exchangers . .	71
Figure 5-3	The tradeoff to choose $\dot{m}_3$ . . . . .	72
Figure 5-4	Change $\dot{m}_3$ in the heat exchangers to reduce the temperature dif- ference . . . . .	73
Figure 5-5	The schematic diagram of the MERS . . . . .	74
Figure 5-6	$T_{3b}$ in the $T$ - $Q$ diagram of the heat transfer processes . . . . .	76
Figure 6-1	Sketch of the cascade system . . . . .	79
Figure 6-2	Diagrams of water circuit and $2e-2f$ process . . . . .	80
Figure 6-3	Sketch of the stand-alone systems . . . . .	81
Figure 1-1	Diagram of heat transfer under constant temperature . . . . .	91
Figure 2-1	Diagram of heat transfer with one constant temperature heat source and constant heat flux . . . . .	93

## List of Tables

Table 2.1	Results of SEA models under specified parameters . . . . .	29
Table 3.1	Key parameters of the dish collector . . . . .	37
Table 3.2	Design specifications of the GPU-3 Stirling engine <sup>[1,2]</sup> . . . . .	46
Table 3.3	Thermal efficiency of the models and experimental data (at $T_{hw} =$ 922 K and $T_{cw} = 288$ K) . . . . .	47
Table 3.4	Output power of the models and experimental data (at $T_{hw} = 922$ K and $T_{cw} = 288$ K) . . . . .	48
Table 4.1	Parameters of SEA models . . . . .	62
Table 4.2	Results of SEA models under specified parameters . . . . .	62
Table 5.1	Main parameters used for both SGSS and MERS . . . . .	76
Table 5.2	Main parameters used for both SGSS and MERS . . . . .	77

## Chapter 1 Introduction

Saving our planet, lifting people out of poverty, advancing economic growth... these are one and the same fight. We must connect the dots between climate change, water scarcity, energy shortages, global health, food security and women's empowerment. Solutions to one problem must be solutions for all.

---

*Ban Ki-moon*

This dissertation considers a way to solve the global problems of energy shortage and environment problem.

### 1.1 Research background and significance

REN21, a global renewable energy policy multi-stakeholder network, published the most comprehensive annual overview of renewable energy of 2016.<sup>[3]</sup> Renewables are now established around the world as mainstream sources of energy. Rapid growth, particularly in the power sector, is driven by several factors, including the improving cost-competitiveness of renewable technologies, dedicated policy initiatives, better access to financing, energy security and environmental concerns, growing demand for energy in developing and emerging economies, and the need for access to modern energy.

Solar energy, which has the advantages of widely distribution, huge amount, inexhaustible and no pollution, has received much attention by many countries and been regarded as the best potential candidate of the fossil energy. The International Energy Agency projected in 2014 that under its "high renewables" scenario, by 2050, solar photovoltaics and concentrating solar power would contribute about 16 and 11 percent, respectively, of the worldwide electricity consumption, and solar would be the world's largest source of electricity.<sup>[4]</sup>

Concentrating solar thermal power generation is another form of power generation technology except solar photovoltaic power generation. Concentrating Solar Power (CSP) energy system uses mirrors to converge sunlight onto a receiver that absorbs the solar energy and transfer it to a heat transfer fluid (HTF) such as a synthetic oil, molten salt or air. The HTF then directly or indirectly used as the heat source in a power cycle. Compared to solar photovoltaic, solar thermal power is gaining more attention for its advantages as higher energy density, smooth power generation, good grid compatibility, easy to integrate with existing fossil power plant.

Concentrating solar power technologies use different mirror configurations to concentrate the sun's light energy onto a receiver and convert it into heat. The heat can then be used to create steam to drive a turbine to produce electrical power or used as industrial process heat. There are three types of CSP technologies being commercially applied: parabolic trough, parabolic dish and power tower.

A parabolic trough is a type of solar thermal collector whose mirror type is straight in one dimension and curved as a parabola in the other two. The reflector follows the sun during the daylight hours by tracking along a single axis. The energy of sunlight is reflected by the mirror and focused on the pipe positioned at the focal line. HTF (e.g. synthetic oil) runs through the pipe to absorb the heat generated by the focused sunlight, then used as the heat source for heating process or power generation. Figure 1-1 shows a parabolic trough product made by Alpha-E.

A parabolic dish is a type of solar thermal collector whose mirror type is part of a circular paraboloid, that can converging the incoming sunlight traveling along the axis to the focus. A receiver or Stirling engine is put at the focal point to absorb the converged energy. Figure 1-2 shows a 38 kW prototype Stirling engine product of Xiangtan Electric Manufacturing Group Co., Ltd. (XEMC).

A solar power tower is a type of solar furnace using a tower to receive the focused sunlight. It uses an array of flat, movable mirrors (called heliostats) to focus the sun's rays upon a collector tower (the target). Figure 1-3 shows the Solar Two power tower.

Among the three solar thermal power technologies, parabolic trough is the most mature and commercially deployed technology. However, it has a low concentration ratio, the receiver's temperature is relatively low, the solar-to-electric efficiency is relatively low. Parabolic dish can obtain high temperature thermal energy, it's solar-to-electric can be higher





Figure 1-1 Alpha-Trough-350, a parabolic trough product made by Alpha-E

than parabolic trough. Besides, one advantage of parabolic trough is that it requires much less water for power generation. However, solar parabolic dish is not a large-scale application, it's mainly applied for distributed power generation for its compact structure and easy installation. Solar power tower has a very high concentration ratio when more mirrors (also called heliostats) are used, the receiver's temperature can be very high and it can be applied for large-scale application. However, it has some disadvantages such as high investment. It is currently in rapid development stage.

It is very important to find out a way the utilize the advantages of existing solar thermal power technologies and overcome their disadvantages. In other words, to find out a new technology with higher efficiency lower cost is urgent. This research is trying to achieve this by proposing a cascade system that uses different collector power generation methods and different thermodynamic cycles, which may be a new and feasible technology to realize large-scale solar thermal power generation.

## 1.2 State of the art

### 1.2.1 Parabolic trough

Parabolic trough solar technology is the most proven and lowest cost large-scale solar power technology available.<sup>[5]</sup>



Figure 1-2 A 38 kW prototype Stirling engine product of XEMC

Padilla<sup>[6]</sup> performed a detailed one dimensional numerical heat transfer analysis of a PTC (Parabolic Trough Collector). To solve the mathematical model of heat transfer of the PTC model, the partial differential equations were discretized and the nonlinear algebraic equations were solved simultaneously. The numerical results was validated to the data from Sandia National Laboratory (SNL).

To understand the thermal performance of the collector and identify the heat losses from the collector, Mohamad<sup>[7]</sup> analyzed the temperature variation of the working fluid, tube and glass along the collector.

Guo<sup>[8]</sup> investigated the energy efficiency and exergy efficiency of the parabolic trough collector. The result shown that there exists an optimal mass flow rate of working fluid for



Figure 1-3 Overall view of Solar Two power tower

exergy efficiency, and the thermal efficiency and exergy efficiency have opposite changing tendencies under some conditions.

Guo<sup>[9]</sup> implemented a multi-parameter optimization of parabolic trough solar receiver based on genetic algorithm where Exergy and thermal efficiencies were employed as objective function.

Padilla<sup>[10]</sup> performed a comprehensive exergy balance of a parabolic trough collector based on the previous heat transfer model<sup>[6]</sup>. The results shown that inlet temperature of heat transfer fluid, solar irradiance, and vacuum in annulus have a significant effect on the thermal and exergetic performance, but the effect of wind speed and mass flow rate of heat transfer fluid is negligible. It was obtained that inlet temperature of heat transfer fluid cannot be optimized to achieve simultaneously maximum thermal and exergetic efficiency because they exhibit opposite trends. Finally, it was found that the highest exergy destruction is due to the heat transfer between the sun and the absorber while for exergy losses is due to optical error.

Huang<sup>[11]</sup> proposed an analytical model for optical performance which employed a mod-

ified integration algorithm.

Wang<sup>[12]</sup> proposed a mathematical model for the optical efficiency of the parabolic trough solar collector and selected three typical regions of solar thermal utilization in China for the model. The model is validated by comparing the test results in parabolic trough power plant, with relative error range of 1% to about 5%.

Al-Sulaiman<sup>[13]</sup> presented the exergy analysis of selected thermal power systems driven by PTSCs. The power of the thermal power system is produced using either a steam Rankine cycle (SRC) or a combined cycle, in which the SRC is the topping cycle and an organic Rankine cycle (ORC) is the bottoming cycle.

Hachicha<sup>[14]</sup> presented a detailed numerical heat transfer model based on the finite volume method for the parabolic trough collector. This model is based on finite volume method and ray trace techniques and takes into account the finite size of the Sun. The model is thoroughly validated with results from the literature and it shows a good agreement with experimental and analytical results.

Ashouri<sup>[15]</sup> coupled a small scale parabolic trough collector and a thermal storage tank along with an auxiliary heater to a Kalina cycle to study the performance of the system throughout the year, both thermodynamically and economically.

Guo<sup>[16]</sup> developed a nonlinear distribution parameter model to model the dynamic behaviors of direct steam generation parabolic trough collector loops under either full or partial solar irradiance disturbance.

Bader<sup>[17]</sup> developed a numerical model of a tubular cavity-receiver that uses air as the heat transfer fluid. Four different receiver configurations are considered, with smooth or V-corrugated absorber tube and single- or double-glazed aperture window. The different types of energy loss by the collector have been quantified, and the temperature distribution inside the receiver has been studied. The pumping power required to pump the HTF through the receiver has been determined for a 200 m long collector row.

Good<sup>[18]</sup> proposed solar trough concentrators using air as heat transfer fluid at operating temperatures exceeding 600 °C. It consists of an array of helically coiled absorber tubes contained side-by-side within an insulated groove having a rectangular windowed opening. Secondary concentrating optics are incorporated to boost the geometric concentration ratio to 97×.

Boukelia<sup>[19]</sup> investigated the feed-forward back-propagation learning algorithm with three different variants; Levenberg Marquardt (LM), Scaled Conjugate Gradient (SCG),

and Pola-Ribiere Conjugate Gradient (PCG), used in artificial neural network (ANN) to find the best approach for prediction and techno-economic optimization of parabolic trough solar thermal power plant (PTSTPP) integrated with fuel backup system and thermal energy storage.

Kaloudis<sup>[20]</sup> investigated a PTC system with nanofluid as the HTF in terms of Computational Fluid Dynamics (CFD). Syltherm 800 liquid oil was used as the HTF, and  $\text{Al}_2\text{O}_3$  nanoparticles with the concentrations ranges from 0% to 4% was investigated. A boost up to 10% on the collector efficiency was reported for  $\text{Al}_2\text{O}_3$  concentration of 4%.

Tan<sup>[21]</sup> proposed a two-stage photovoltaic thermal system based on solar trough concentration is proposed, in which the metal cavity heating stage is added on the basis of the PV/T stage, and thermal energy with higher temperature is output while electric energy is output. The experimental platform of the two-stage photovoltaic thermal system was established, with a 1.8 m<sup>2</sup> mirror PV/T stage and a 15 m<sup>2</sup> mirror heating stage, or a 1.8 m<sup>2</sup> mirror PV/T stage and a 30 m<sup>2</sup> mirror heating stage. The results showed that with single cycle, the long metal cavity heating stage would bring lower thermal efficiency, but temperature rise of the working medium is higher, up to 12.06 °C with only single cycle. With 30 min closed multiple cycles, the temperature of the working medium in the water tank was 62.8 °C, with an increase of 28.7 °C, and thermal energy with higher temperature could be output.

Al-Sulaiman<sup>[22]</sup> proposed a novel system based on PTC and ORC for combined cooling, heating and power (CCHP). Performance assessment, including efficiency, net electrical power, and electrical to heating and cooling ratios, of the system shown that when CCHP is used, the efficiency increases significantly. This study reveals that the maximum electrical efficiency for the solar mode is 15%, for the solar and storage mode is 7%, and for the storage mode is 6.5%. The maximum CCHP efficiency for the solar mode is 94%, for the solar and storage mode is 47%, and for the storage mode is 42%.

Lobon<sup>[23]</sup> introduced a computational fluid dynamic simulation approach to predict the behavior of a solar steam generating system, which is located at the Plataforma Solar de Almeria, Spain. The CFD package STAR-CCM+ code has been used to implement an efficient multiphase model capable of simulating the dynamics of the multiphase fluid in parabolic-trough solar collectors. Numerical and experimental data are compared in a wide range of working conditions.

Xu<sup>[24]</sup> presented a method to compensate the end loss effect of PTC. An optical analysis

on the end loss effect of PTC with horizontal north-south axis (PTC-HNSA) is performed and a five-meter PTC-HNSA experimental system was built. The increased thermal efficiency of the experimental system is measured, and the result that the experimental value (increased thermal efficiency) substantially agreed with the theoretical value (increased optical efficiency) is gained.

Liu<sup>[25]</sup> developed a mathematical model of PTC using the least squares support vector machine (LSSVM) method. Numerical simulations are implemented to evaluate the feasibility and efficiency of the LSSVM method, where the sample data derived from the experiment and the simulation results of two solar collector systems with 30 m<sup>2</sup> and 600 m<sup>2</sup> solar fields, and the complicated relationship between the solar collector efficiency and the solar flux, the flow rate and the inlet temperature of the heat transfer fluid (HTF) is extracted.

### 1.2.2 Parabolic dish

One of the main goals of the BIOSTIRLING-4SKA project, funded by the European Commission, is the development of a hybrid Dish-Stirling system based on a hybrid solar-gas receiver, which has been designed by the Swedish company Cleanergy<sup>[26]</sup>.

Craig<sup>[27]</sup> proposed two types of cooking sections of the solar parabolic dish system: the spiral hot plate copper tube and the heat pipe plate. A conical cavity of copper tubes were put on the focus of the collectors to collect heat and the heat is stored inside an insulated tank which acts both as storage and cooking plate. The use of heat pipes to transfer heat between the oil storage and the cooking pot was compared to the use of a direct natural syphon principle which is achieved using copper tubes in spiral form like electric stove. An accurate theoretical analysis for the heat pipe cooker was achieved by solving the boiling and vaporization in the evaporator side and then balancing it with the condensation and liquid-vapor interaction in the condenser part while correct heat transfer, pressure and height balancing was calculated in the second experiment. The results show and compare the cooking time, boiling characteristics, overall utilization efficiencies and necessary comparison between the two system and other existing systems.

Flux distribution of the receiver is simulated successfully by Mao<sup>[28]</sup> using MCRT method. The impacts of incident solar irradiation, aspect ratio (the ratio of the receiver height to the receiver diameter), and system error on the radiation flux of the receiver are investigated.



Mawire<sup>[29]</sup> investigated the thermal performance of a cylindrical cavity receiver for an SK-14 parabolic dish concentrator. The receiver exergy rates and efficiencies are found to be appreciably smaller than the receiver energy rates and efficiencies. The exergy factor is found to be high under conditions of high solar radiation and under high operating temperatures. An optical efficiency of around 52% for parabolic dish system is determined under high solar radiation conditions.

Reddy<sup>[30,31]</sup> performed the theoretical thermal performance analysis of a fuzzy focal solar parabolic dish concentrator with modified cavity receiver. Total heat loss from the modified cavity receiver is estimated considering the effects of wind conditions, operating temperature, emissivity of the cavity cover and thickness of insulation. Time constant test was carried out to determine the influence of sudden change in solar radiation at steady state conditions. The daily performance tests were conducted for different flow rates.

Vikram<sup>[32]</sup> investigated the total heat losses of modified cavity receiver of SPD with three configurations using 3D numerical model. The effects of various parameters such as diameter ratio, angle of inclination, operating temperature, insulation thickness and emissivity of the cavity cover on the heat losses from the modified cavity receiver are investigated. An ANN model is developed to predict the heat loss for a large set of influencing parameters. Based on ANN modeling, improved Nusselt number correlations are proposed for convective, radiative and total heat losses from the modified cavity receiver. The convective heat losses are greatly influenced by receiver inclination whereas the radiation heat losses are influenced by the cavity cover emissivity. The diameter ratio also plays a major role in heat losses from the cavity receiver. The present method predicts the heat losses more accurately compared with the existing models.

Atul<sup>[33]</sup> proposed a low-cost solar dish water heating system and investigated the effect of variation of mass flow rate on performance of the heater prototype. A novel truncated cone-shaped helical coiled receiver made up of copper is put at the focal point of SP.

CRTEn developed a solar parabolic concentrator (SPC) using four types of absorbers: flat plat, disk, water calorimeter and solar heat exchanger.<sup>[34]</sup> For the system different types of absorbers, experiments were conducted to obtain the mean concentration ratio and both energy and exergy efficiency. Results shown that thermal energy efficiency of the system varies from 40% to 77%, the concentrating system reaches an average exergy efficiency of 50% and a concentration factor around 178.

Blazquez<sup>[26]</sup> studied the optimization of the concentrator and receiver cavity geometry of parabolic dish system. Ray-tracing analysis has been performed with the open source software Tonatiuh, a ray-tracing tool specifically oriented to the modeling of solar concentrators.

Uma<sup>[35]</sup> carried out the simulation of the structural, thermal and CFD analysis of the dish with varying metallic properties (Aluminium, Copper and StainlessSteel) under different wind conditions. Computational Fluid Dynamics (CFD) was done to simulate the thermal performance of the dish at two different wind velocities.

Patil<sup>[36]</sup> described the development of automatic dual axis solar tracking system for solar parabolic dish. Five light dependent resistors were used to sense the sunlight and Two permanent magnet DC motors are used to move the solar dish. A controller software were developed to control the motors using the data sensed by the resistors.

Pavlovic<sup>[37]</sup> presented a procedure to design a square facet concentrator for laboratory-scale research on medium-temperature thermal processes. A parabolic collector made up of individual square mirror panels (facets) were investigated. These facets can deliver up to 13.604 kW radiative power over a 250 mm radius dish receiver with average concentrating ratio exceeding 1200.

### 1.2.3 Power tower

Besarati and Yogi<sup>[38]</sup> developed a new and simple method to improve the calculation speed and accuracy for shading and blocking computation of the heliostat field. The Sassi method<sup>[2]</sup> is used for the shading and blocking efficiency. A 50 MWth heliostat field in Dagget, California, USA was used as a case study for the proposed method.

Haroun<sup>[39]</sup> proposed a novel system combines both solar chimney and solar tower. The solar tower receiver was installed at the top of the chimney. Theoretical study of this novel system was conducted. The results shown that the new system generates more power than conventional system with the same parameters of solar irradiance, collector radius, height of chimney, and height of solar tower. The inlet air speed of the chimney is higher than that of the conventional, and it increases with the solar irradiance. Moreover, the results indicated that there exists a optimum ratio of solar tower height to solar chimney height for the maximum overall power.

Franchini et al.<sup>[40]</sup> developed a computing procedure for solar tower system under both nominal and part load conditions. A Siemens gas turbine product, SGT-800, was considered



as a study case for the solar tower system. The turbine has a dual pressure heat recovery steam generator, which can be used for the Integrated Solar Combined Cycle (ISCC) plant. A model of Solar Rankine Cycle (SRC) driven by PTCs was also developed for comparison. A highest solar-to-electric efficiency of 21.8% can be achieved by the designed ISCC plant. And in all conditions, the global solar energy conversion efficiency of the ISCC is higher than that of the SRC.

Kim et al.<sup>[41]</sup> investigated the heat loss of solar central receiver. Numerical simulations using CFD (Computational Fluid Dynamics) with the consideration of four different receiver shapes were carried out to get the influence on convection and radiation heat losses. Different opening ratio between cavity aperture area and receiver aperture area, receiver temperatures, wind velocities and wind directions (head-on and side-on) were considered for the simulations. Results were used to get a simplified correlation model which gets the fraction of convection heat loss. The correlation obtained showed good agreements with the simulation results. The correlation was also validated with experimental data from three central receiver systems (Martin Marietta, Solar One and Solar Two).

Lara et al.<sup>[42]</sup> presented a novel modeling tool for calculation of central receiver concentrated flux distributions. The modeling tool is based on a drift model that includes different geometrical error sources in a rigorous manner and on a simple analytic approximation for the individual flux distribution of a heliostat. The model is applied to a group of heliostats of a real field to obtain the resulting flux distribution and its variation along the day. The distributions differ strongly from those obtained assuming the ideal case without drift or a case with a Gaussian tracking error function. The time evolution of peak flux is also calculated to demonstrate the capabilities of the model. The evolution of this parameter also shows strong differences in comparison to the case without drift.

Wei et al.<sup>[43]</sup> proposed a new method for the design of the heliostat field layout for solar tower power plant. In the new method, the heliostat boundary is constrained by the receiver geometrical aperture and the efficiency factor which is the product of the annual cosine efficiency and the annual atmospheric transmission efficiency of heliostat. With the new method, the annual interception efficiency does not need to be calculated when places the heliostats, therefore the total time of design and optimization is saved significantly. Based on the new method, a new code for heliostat field layout design (HFLD) has been developed and a new heliostat field layout for the PS10 plant at the PS10 location has been designed

by using the new code. Compared with current PS10 layout, the new designed heliostats have the same optical efficiency but with a faster response speed. In addition, to evaluate the feasibility of crops growth on the field land under heliostats, a new calculation method for the annual sunshine duration on the land surface is proposed as well.

Wei et al.<sup>[44]</sup> developed a new code for the design and analysis of the heliostat field layout for power tower system. In the new code, a new method for the heliostat field layout is proposed based on the edge ray principle of nonimaging optics. The heliostat field boundary is constrained by the tower height, the receiver tilt angle and size and the heliostat efficiency factor which is the product of the annual cosine efficiency and the annual atmospheric transmission efficiency. With the new method, the heliostat can be placed with a higher efficiency and a faster response speed of the design and optimization can be obtained. A new module for the analysis of the aspherical heliostat is created in the new code. A new toroidal heliostat field is designed and analyzed by using the new code. Compared with the spherical heliostat, the solar image radius of the field is reduced by about 30% by using the toroidal heliostat if the mirror shape and the tracking are ideal. In addition, to maximize the utilization of land, suitable crops can be considered to be planted under heliostats. To evaluate the feasibility of the crop growth, a method for calculating the annual distribution of sunshine duration on the land surface is developed as well.

Xu et al.<sup>[45]</sup> created a model of the 1 MW Dahan solar thermal power tower plant using the modular modeling method. The dynamic and static characteristics of the power plant are analyzed based on these models. Response curves of the system state parameters are given for different solar irradiance disturbances. Conclusions in this paper are good references for the design of solar thermal power tower plant.

Xu et al.<sup>[46]</sup> built the thermal energy storage model of Badaling 1 MW solar power tower plant using the modular modeling method. This model can accurately simulate the recharge and discharge processes of thermal energy storage system. The dynamic and static characteristics of the thermal energy storage system are analyzed based on the model response curves of the system state parameters that are obtained from different steam flow disturbances. Conclusions of this paper are good references for the design, operating, and control strategy of solar thermal power plant.

## 1.2.4 Cascade solar system

### 1.2.4.1 Cascade collection

Suzuki<sup>[47]</sup> analyzed the solar thermal systems with two different types of collectors connected in series. A key value of the collectors was revealed to be the key factor to determine whether a cascade system is better than either one of the collectors alone. The value is the product of the collector efficiency factor and the optical efficiency. If the value of the lower concentration ratio collector is larger than that of the higher concentration ratio, the cascade system is more effective. Furthermore, to obtain the maximum energy gain, there exists the optimum operating conditions.

Oshida and Suzuki<sup>[48]</sup> presented the idea of optical cascade heat collection of solar energy. Two absorbers, one warm and the other hot, are used in the cascade system. The warm absorber is heated by the Fresnel lenses and the hot absorber is heated by CPC. HTF flows into the warm absorber firstly and then flows into the hot absorber. The temperature of HTF can increase more effectively.

Kribus et al.<sup>[49]</sup> proposed an idea of using separate aperture stages for different irradiance distribution.

A high-temperature solar thermal receiver is subject to temperature-dependent emission and convection losses. Minimizing these losses is essential to realization of high temperature, high efficiency systems. Dividing the aperture into separate stages according to the irradiance distribution has been shown theoretically to significantly reduce these losses. In such a partitioned system, the working fluid is gradually heated as it passes through a sequence of receiver elements with increasing irradiance levels. An experiment to demonstrate this principle using two heating stages has been constructed at the Weizmann Institute's Solar Tower. The high-temperature receiver stage is the Directly Irradiated Annular Pressurized Receiver (DIAPR). The low-temperature stage is implemented as a partial ring of intermediate-temperature cavity tubular receivers (Preheaters) surrounding the central high-temperature stage. Following initial concentration by a part of the Weizmann Institute heliostat field, the light enters the receivers via secondary concentrators constructed as approximate CPCs. We present recent test results with the two-stage system. Air exit temperatures of up to 1000°C were obtained, with the low-temperature stage supplying up to 750°C. The power output was up to 55 kWth. Heat transfer in the high-temperature receiver, losses due

to the partitioning, and future plans for partitioned receivers are discussed.

Collado2016<sup>[50]</sup>

In solar power tower (SPT) systems, selecting the optimum location of thousands of heliostats and the most profitable tower height and receiver size remains a challenge. Given the complexity of the problem, breaking the optimisation process down into two consecutive steps is suggested here; first, a primary, or energy, optimisation, which is practically independent of the cost models, and then a main, or economic, optimisation. The primary optimisation seeks a heliostat layout supplying the maximum annual incident energy for all the explored combinations of receiver sizes and tower heights. The annual electric output is then calculated as the combination of the incident energy and the simplified (annual averaged) receiver thermal losses and power efficiencies. Finally, the figure of merit of the main optimisation is the levelised cost of electric energy (LCOE) where the capital cost models used for the LCOE calculation are reported by the System Advisor Model (SAM)-NREL and Sandia. This structured optimisation, splitting energy procedures from economic ones, enables the organisation of a rather complex process, and it is not limited to any particular power tower code. Moreover, as the heliostat field layout is already fully optimised before the economic optimisation, the profiles of the LCOE versus the receiver radius for the tower heights explored here are sharp enough to establish optima easily. As an example of the new procedure, we present a full thermo-economic optimisation for the design of the collector field of an actual SPT system (Gemasolar, 20 MWe, radially staggered surrounding field with 2650 heliostats, 15 h of storage). The optimum design found for Gemasolar is reasonably consistent with the scarce open data. Finally, optimum designs are strongly dependent on the receiver cost, the electricity tariff and the assumed maximum receiver surface temperature.

Reddy<sup>[51]</sup>

Numerical analysis of solar dish modified cavity receiver with Cone, CPC and Trumpet reflectors is presented. Three-dimensional modeling is carried out to estimate the convective and radiative heat loss from the receiver for different angles of inclination and operating temperatures. Incorporating reflectors in the modified cavity receiver for second stage concentration, the natural convection heat losses are reduced by 29.23, 19.81 and 19.16%, respectively. The receiver with the trumpet reflector has shown better performance as compared to other configurations.

Mills<sup>[52]</sup>

Maximally concentrating collectors include the class of ideal concentrating collectors, but are a more general class offering many more practical possibilities. By evaluating such configurations using the concept of maximal flux concentration, based upon average radiation flux concentration over the acceptance angle, clear ray trace comparisons may be made between different collector configurations. These comparisons allow the most effective configuration to be selected for a given application. An example of a comparatively simple and practical two-stage concentrator having equal or better maximal performance than previous work for high rim angle primaries is given. This uses an unusual straight section of reflector and allows rays to cross from one reflector segment of the secondary to another. Versions which allow concentration up to 90% of maximal are described, as are versions achieving 80% with high collection efficiency. Use of the geometrical concentration criterion based upon aperture ratios is suggested to be inappropriate for comparisons.

Collado<sup>[50]</sup>

Abstract In solar power tower (SPT) systems, selecting the optimum location of thousands of heliostats and the most profitable tower height and receiver size remains a challenge. Given the complexity of the problem, breaking the optimisation process down into two consecutive steps is suggested here; first, a primary, or energy, optimisation, which is practically independent of the cost models, and then a main, or economic, optimisation. The primary optimisation seeks a heliostat layout supplying the maximum annual incident energy for all the explored combinations of receiver sizes and tower heights. The annual electric output is then calculated as the combination of the incident energy and the simplified (annual averaged) receiver thermal losses and power efficiencies. Finally, the figure of merit of the main optimisation is the levelised cost of electric energy (LCOE) where the capital cost models used for the {LCOE} calculation are reported by the System Advisor Model (SAM)-NREL and Sandia. This structured optimisation, splitting energy procedures from economic ones, enables the organisation of a rather complex process, and it is not limited to any particular power tower code. Moreover, as the heliostat field layout is already fully optimised before the economic optimisation, the profiles of the {LCOE} versus the receiver radius for the tower heights explored here are sharp enough to establish optima easily. As an example of the new procedure, we present a full thermo-economic optimisation for the design of the collector field of an actual {SPT} system (Gemastar, 20 MWe, radially staggered surrounding

field with 2650 heliostats, 15 h of storage). The optimum design found for Gemasolar is reasonably consistent with the scarce open data. Finally, optimum designs are strongly dependent on the receiver cost, the electricity tariff and the assumed maximum receiver surface temperature.

Gordon and Saltiel<sup>[53]</sup>

We present an analytic method for predicting the long-term performance of solar energy systems with more than one collector brand (“multi-stage” systems). This procedure enables the designer to determine the most cost-effective method of combining different collector brands for a given load. Although our derivations pertain to solar systems for constant load applications and/or near constant collector operating threshold, they can also be used for conventional multi-pass designs. The problems of excess energy delivery, and of various collector on/off control strategies, are taken into account. Our results are simple closed-form expressions whose evaluation requires readily-available average climatic data, and load and collector characteristics. The analytic method is illustrated by a solved example which shows that significant savings can be realized by combining different collector brands for a given application (multi-staging).

空气槽式集热器

Good et al.<sup>[18]</sup>

An entirely novel solar receiver design for solar trough concentrators is proposed using air as heat transfer fluid at operating temperatures exceeding 600 °C. It consists of an array of helically coiled absorber tubes contained side-by-side within an insulated groove having a rectangular windowed opening. Secondary concentrating optics are incorporated to boost the geometric concentration ratio to 97×. The multiple absorber tubes are connected via two axial pipes serving as feeding and collecting manifolds. The steady-state energy conservation equation coupling radiation, convection, and conduction is formulated and solved numerically using the finite volume technique. The solar flux distribution incident at each absorber tube is determined by Monte Carlo ray-tracing using spectrally and directionally dependent optical properties. Thermal radiative heat exchange is analyzed using the gray-band approximated radiosity method for an enclosure with a selective window. Model validation is accomplished by comparison to on-sun experiments with a 1 m-long solar receiver prototype composed of 7 absorber tubes, mounted on a 4.85 m-aperture solar trough concentrator. Feeding rates in the range of 5–20 l/min to each absorber tube led to air outlet temperatures

of 621–449 °C and a peak receiver efficiency of 64%.

Barder et al.<sup>[17]</sup>

A tubular cavity-receiver that uses air as the heat transfer fluid is evaluated numerically using a validated heat transfer model. The receiver is designed for use on a large-span (9 m net concentrator aperture width) solar parabolic trough concentrator. Through the combination of a parabolic primary concentrator with a nonimaging secondary concentrator, the collector reaches a solar concentration ratio of 97.5. Four different receiver configurations are considered, with smooth or V-corrugated absorber tube and single- or double-glazed aperture window. The collector's performance is characterized by its optical efficiency and heat loss. The optical efficiency is determined with the Monte Carlo ray-tracing method. Radiative heat exchange inside the receiver is calculated with the net radiation method. The 2D steady-state energy equation, which couples conductive, convective, and radiative heat transfer, is solved for the solid domains of the receiver cross-section, using finite-volume techniques. Simulations for Sevilla/Spain at the summer solstice at solar noon (direct normal solar irradiance:  $847 \text{ W} \cdot \text{m}^{-2}$ , solar incidence angle:  $13.9^\circ$ ) yield collector efficiencies between 60% and 65% at a heat transfer fluid temperature of  $125^\circ\text{C}$  and between 37% and 42% at  $500^\circ\text{C}$ , depending on the receiver configuration. The optical losses amount to more than 30% of the incident solar radiation and constitute the largest source of energy loss. For a 200 m long collector module operated between 300 and  $500^\circ\text{C}$ , the isentropic pumping power required to pump the {HTF} through the receiver is between 11 and 17 kW.

#### 多种集热器的混合利用

Some researchers have investigated the combination of different types of collectors for CSP. Desai et al.<sup>[54]</sup> presented an integrated CSP plant configuration with the combination of both PTC and LFC. Thermo-economic comparisons between PTC-based, LFC-based and integrated CSP plant configurations, without hybridization and storage, were analyzed. It is demonstrated that the cost of energy of an integrated CSP plant is 9.6 % cheaper than PTC-based CSP plant and 13.5 % cheaper than LFR-based CSP plant. Coco et al.<sup>[55]</sup> developed four different line-focusing solar power plant configurations integrated both direct steam generation and Brayton power cycle. In these configurations, collectors are divided into different solar fields to supply different heat demands. This provides the ability to use different types of collectors (parabolic trough and linear Fresnel) in the systems.

#### 1.2.4.2 Cascade utilization

Many researchers have done the work on the combination of different thermodynamic cycles for CSP. Lots of the work focused on integrated solar combined cycle (ISCC) with parabolic trough, where Rankine cycle is used as the bottom cycle. Li and Yang<sup>[56]</sup> proposed a novel two-stage ISCC system that could reach up to 30% of the net solar-to-electricity efficiency. In their research, the impact on the system overall efficiencies of how and where solar energy is input into ISCC system was investigated. Behar et al.<sup>[57]</sup> reviewed the R&D activities and published studies since the introduction of such a concept in the 1990s. One of the conclusions is that the higher the solar radiation intensity the better is the performance of the ISCCS than those of conventional CSP technologies. Gulen<sup>[58]</sup> used the exergy concept of the second law of thermodynamics to distill the complex optimization of ISCCS to its bare essentials. After the exergy analysis, physics-based, user-friendly guidelines were provided to help direct studies involving heavy use of time consuming system models in a focused manner and evaluate the results critically to arrive at feasible ISCC designs. Shaa-ban<sup>[59]</sup> introduced a novel ISCC with steam and organic Rankine cycles. The ORC was used in order to intercool the compressed air and produce a net power from the received thermal energy. The proposed cycle performance was studied and optimized with different ORC working fluids. Alqahtani and Dalia<sup>[60]</sup> quantified the economic and environmental benefits of an ISCC power plant relative to a stand-alone CSP with energy storage, and a natural gas-fired combined cycle plant. Results show that integrating the CSP into an ISCC reduces the LCOE of solar-generated electricity by 35-40% relative to a stand-alone CSP plant, and provides the additional benefit of dispatch ability. Manente<sup>[61]</sup> developed a 390 MWe three pressure level natural gas combined cycle to evaluate different integration schemes of ISCC. Both power boosting and fuel saving operation strategies were analyzed in the search for the highest annual efficiency and solar share. Result shown that, compared to power boosting, the fuel saving strategy shows lower thermal efficiencies of the integrated solar combined cycle due to the efficiency drop of gas turbine at reduced loads. Rovira et al.<sup>[62]</sup> compared the annual performance and economic feasibility of ISCC using two solar concentrating technologies: parabolic trough collectors (PTC) and linear Fresnel collectors (LFC). Different configurations were considered and results shown that only evaporative configuration is the most suitable choice. Compared with traditional ISCC design, two new conceptual hybrid designs for ISCC with parabolic trough were represented by Turchi et al.<sup>[63]</sup>. In the



first design, gas turbine waste heat is supplied for both heat transfer fluid heating and feed water preheating. In the second design, gas turbine waste heat is supplied for a thermal energy storage system. Mukhopadhyay and Ghosh<sup>[64]</sup> presented a conceptual configuration of a solar power tower combined heat and power plant with a topping air Brayton cycle. The conventional gas turbine combustion chamber is replaced with a solar receiver. A simple downstream Rankine cycle with a heat recovery steam generator and a process heater have been considered for integration with the solar Brayton cycle. Li et al.<sup>[65]</sup> presented a novel cascade system using both steam Rankine cycle (SRC) and organic Rankine cycle (ORC). Screw expander is employed in the steam Rankine cycle for its good applicability in power conversion with steam-liquid mixture. The heat released by steam condensation is used to drive the ORC. Al-Sulaiman<sup>[13]</sup> compared the produced power of an SRC-ORC combined cycle with traditional SRC cycle. The SRC is driven by parabolic trough solar collectors, and the ORC cycle is driven by the condensation heat of the SRC. Bahari et al.<sup>[66]</sup> considered the optimization of an integrated system using organic Rankine cycle to utilize the heat released by the Stirling cycle. However, the integrated system is a primitive design and it didn't consider the application in CSP field.

### 1.3 Research content

The research is based on the national cooperation project "Collaborative research on key technologies to produce electricity by cascade utilization solar thermal energy" as the background. The objective of this project is to research the equipment of solar thermal power generation system, to propose, develop and optimize a solar thermal cascade system depending on the advantages and disadvantages of the solar thermal power generation systems, and to explore a new feasible technology for large-scale solar thermal power generation. The main contents and conclusions of this paper are as follows:

Firstly, mechanism models were established for the components of solar thermal power generation system. The mechanism mathematical models were developed according to the operation mechanism of the target object and physical equations. The key components in the system, such as collectors, steam generating system, steam turbine and Stirling engine, were modeled with details. The mathematical model of each component is a model verified by the classical theory or a large number of experimental data, which is the basic of the model of the cascade solar thermal power generation system. Heat loss models were established for

the receivers of trough collector and dish collector. For the Stirling engine, based on the reasonable simplification and hypothesis, the model of the Stirling machine considered various losses and irrevisibilities was developed. The component models were developed in MATLAB by using object-oriented method. It makes full use of inheritance and polymorphism to ensure both the independence and the relevance of the components.

Secondly, the topological structure of solar thermal cascade power generation system was proposed. According to the analysis of thermal characteristics and the working characteristics of each component in the system, rationally arranged topological structures of cascade system were proposed. These systems use different thermodynamic cycles to utilize energy in different temperature zones. A reasonable cascade generation system can make full use of the mechanism models of the power generation system and provide the foundation for higher efficiency solar thermal cascade generation systems. In this paper, several schemes of feasible topological structures of solar thermal cascade system were set up according to the mechanism model of each component. After system evaluation, parameter selection, preliminary calculation and scheme comparison, two representative typical schemes were determined. In one scheme, both Rankine cycle (water as the working fluid) and Stirling cycle are used for power generation. Cooling water of the Rankine cycle is used to cool the hot end of the Stirling engines to recover the released heat. In the other scheme, multiple organic Rankine cycles are used for power generation. Condensation heat of upper cycle is absorbed by lower cycle for energy cascade utilization.

Thirdly, the solar thermal cascade generation system models were developed. Based on the selected solar thermal cascade generation systems, solar thermal cascade generation system models were established based on the model of each component in the systems. The object-oriented features of inheritance, combination and polymorphism were used for the model development. The change rules of the main parameters and the performance indexes under the coupling of external and internal factors were studied. The change mechanism was studied and the calculation method of its performance characteristics was established. After setting up the components, setting the parameters and compiling the environment, the paper completes the system construction of each system scheme, and finally completes the simulation system of solar thermal cascade generation based on MATLAB with the copyright of independent computer software. The system components are relatively independent, easy to replace or improve the parts model; the results of the calculation of the system model can

be a single object to easily view the various components of the system key parameters.

Then, simulation and optimization of cascade solar thermal power generation system model. Based on the study of the performance characteristics of solar thermal cascade generation system, the system is optimized and the structure is reconstructed. In particular, by analyzing the steam generation system of the system, a method of staged heating is proposed to reduce the heat transfer temperature difference in the steam generating system by changing the mass flow rate of the heat conduction oil, effectively reducing the heat generated during the heat exchange process in the steam generating system. Which can improve the efficiency of the whole system. Based on Stirling unit in cascade system, five kinds of basic arrangement forms of Stirling unit are summarized, and the difference of unit efficiency and output power under various arrangement forms is analyzed, and a given cold and heat source fluid Stirling unit under the conditions of the best arrangement.

Finally, the operating parameters of solar thermal cascade power generation system are optimized. According to the specific structural scheme and operation mode, the performance parameters and economic indexes of the cascade generation system are taken as the objective function, reasonable adjustable parameters are selected, various constraints are established, and modern optimization methods such as genetic algorithm and ant colony algorithm are used to complete the system Parameter optimization analysis, as well as the independent system for comparative analysis. The results show that solar thermal cascade power generation system has higher overall photoelectric conversion efficiency under certain parameter conditions than its corresponding independent system. Under the condition of direct solar radiation intensity of  $700 \text{ W/m}^2$  and dish type collector outlet air temperature of  $800^\circ\text{C}$ , the solar thermal cascade power generation system of Scheme 1 is better than the corresponding The efficiency of stand-alone system is increased by 5.2%. The solar thermal cascade power generation system selected in Scheme 2 is 15.3% more efficient than the corresponding independent system.

## Chapter 2 System topology

### 2.1 System topology design

#### 2.1.1 Basic systems

The objective of this research is to research the equipment of solar thermal power generation system, to propose, develop and optimize a solar thermal cascade system depending on the advantages and disadvantages of the solar thermal power generation systems. The research is based on the national cooperation project "Collaborative research on key technologies to produce electricity by cascade utilization solar thermal energy" as the background. There are three kinds of mature technologies been applied commercially – parabolic trough, parabolic dish and solar tower. Considering the future deployment of solar cascade demo system, two solar thermal technologies, parabolic trough and parabolic dish, are chosen as the basic systems for the design of cascade solar thermal power system. For the cascade utilization of the high temperature of the parabolic receiver, air (or nitrogen) is used as the HTF to transfer the heat collected. Figure 2-1 shows the schematic diagrams of a parabolic trough system and a parabolic dish system.

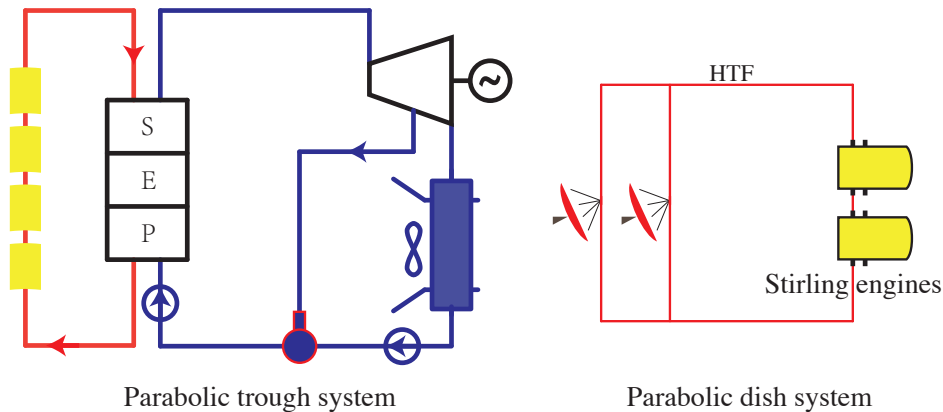


Figure 2-1 Schematic diagrams of a parabolic trough system and a parabolic dish system

With different considerations (such as water Rankine cycle or ORC, combination of different systems, connection types of collectors, etc) of the cascade system topology, multiple

combination topologies may be used for cascade systems. To get the most suitable system topology, these considerations will be analyzed in the following sections.

### 2.1.2 Rankine cycle fluid

There are two important aspects to consider when selecting the working fluid of the Rankine cycle solar power system:

1. Select the working fluid that is conducive to the optimization of the cycle efficiency  
For a Rankine cycle solar system, the collector efficiency reduces with operating temperature, and the Rankine cycle efficiency increases with operating temperature, there exists an optimal operating temperature as illustrated in Fig. 2-2. The working fluid should be conducive to achieve the optimal operating temperature.

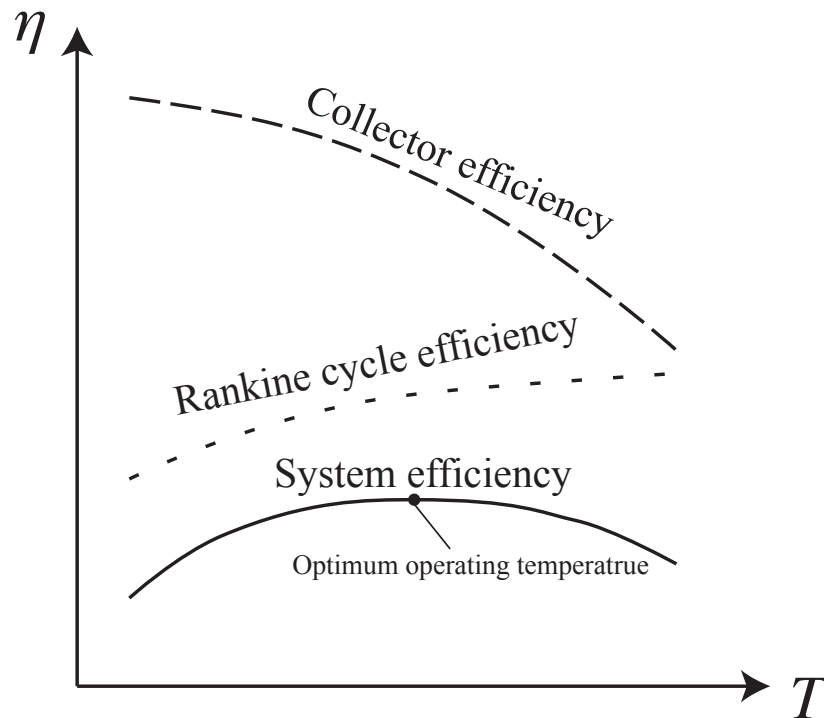


Figure 2-2 Collector and Rankine cycle efficiency variation with operating temperature

2. The working fluid state matches the heat transfer fluid state, if heat transfer fluid is used

On the one hand, the operating temperature of the working fluid should be lower than

the collecting temperature of the HTF. On the other hand, the operating temperature of the working fluid should not be much lower than the collecting temperature of the HTF, for this will cause large exergy loss during the heat exchange process.

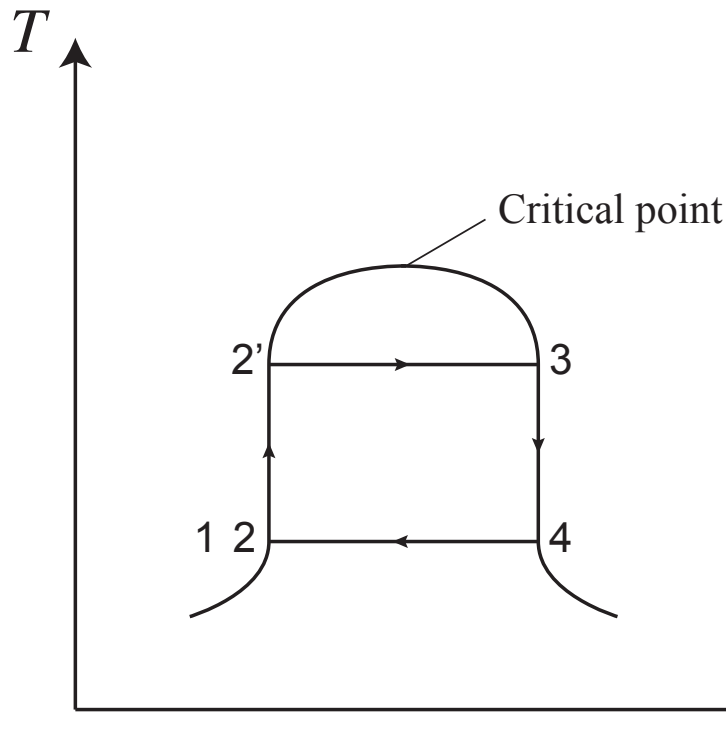


Figure 2-3 Collector and Rankine cycle efficiency variation with operating temperature

An ideal working fluid would have the temperature entropy diagram given in Fig 2-3. The following characteristics listed by Abbin and Leuenberger<sup>[67]</sup> describe this fluid:

- The heat capacity of the liquid phase should be small. This makes the curve 22' in Fig. 2-3 almost vertical.
- The critical point should be above the highest operating temperature to allow all heat to be added at that temperature.
- The vapor pressure at the highest operating temperature should be moderate for safety reasons and to reduce the cost of the equipment.
- The vapor pressure at the condensing temperature should be above atmospheric pressure to prevent air leakage into the system.
- The specific volume of the vapor at state 4 should be small to avoid large-diameter

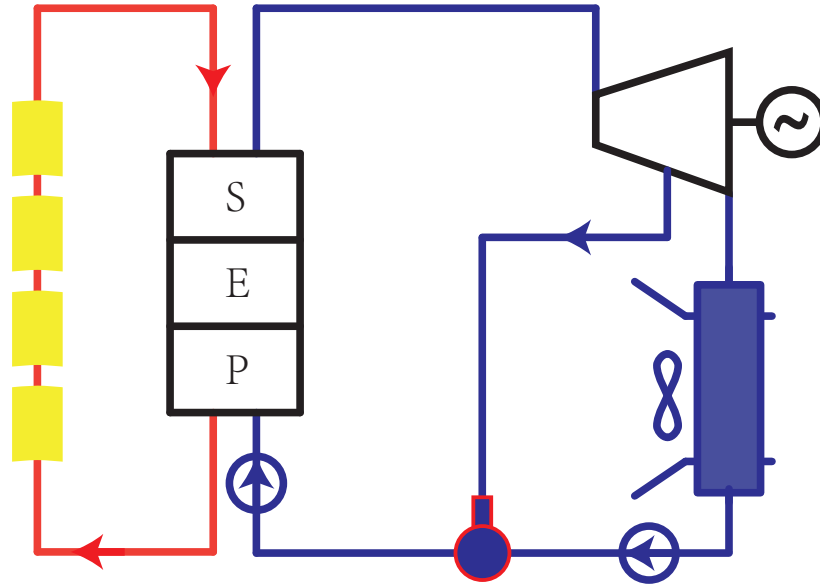
turbine wheels, casings, and heat exchangers.

- The saturated vapor curve 3-4 in fig. 2-3 should be vertical to avoid expansion into the wet vapor region (negative  $ds/dT$ ) or expansion into the superheat region (positive  $ds/dT$ ).
- For low-power turbine applications, the fluid should have a high molecular weight to minimize the rotational speed and/or the number of turbine stages and to allow for reasonable mass flow rates and turbine nozzle areas.
- The fluid should be liquid at atmospheric pressure and temperature for ease of handling and containment.
- The freezing point should be lower than the lowest ambient operating temperature.
- The fluid should have good heat-transfer properties, be inexpensive, thermally stable at the highest operating temperature, nonflammable, noncorrosive, nontoxic, and so on.

Water is the most commonly used fluid for Rankine cycle, it is more mature to design Rankine cycle components for steam systems than any other liquid. It is inexpensive to use (although boiler-grade water must be highly distilled and thus costs more than tap water), sealing of the high-pressure portions of a Rankine cycle using steam is not critical. Non-flammability and ready availability of steam are additional advantages. Because it has a critical temperature and pressure of 374 °C/22.1 MPa, it can be used for systems operating at fairly high temperatures with most of the heat addition (at constant temperature) and at moderate pressure. Figure 2-4 shows the schematic diagram of a typical steam Rankine cycle solar system.

There are some disadvantages for steam as the Rankine cycle fluid. The low temperature characteristics of steam are not ideal because the steam has a low vapor pressure (0.03 atm) and a very low density at ambient temperature. Therefore, sealing air from low pressure components is a major design problem.

The organic Rankine cycle can be used in the solar parabolic trough technology in place of the usual steam Rankine cycle. The ORC allows power generation at lower capacities and with a lower collector temperature, and hence the possibility for low-cost, small scale decentralized CSP units. Most organic fluids used in organic Rankine cycle are drying fluids. The vapor leaving the expander still contains heat that can be transferred to the compressed liquid stream because the turbine outlet temperature is above the condenser temperature. A



Parabolic trough system

Figure 2-4 Schematic diagram of a typical steam Rankine cycle solar system

vapor-to-liquid heat exchanger, known as a regenerator, is typically used for this purpose. Fig. 2-5 shows the schematic diagram of a typical organic Rankine cycle solar system.

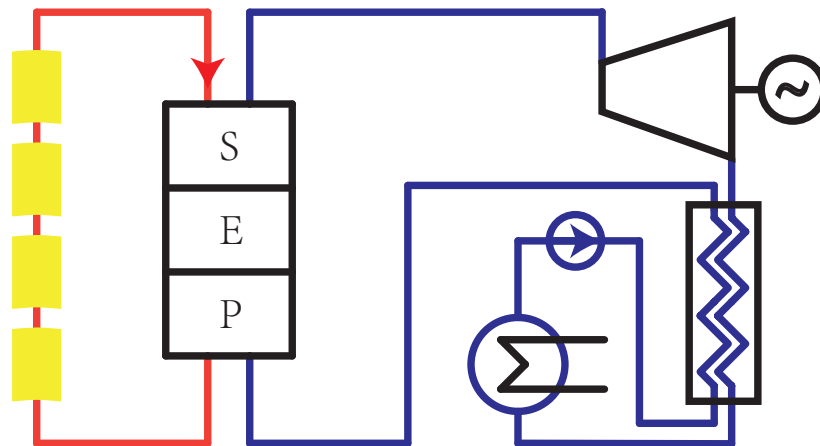


Figure 2-5 Schematic diagram of a typical organic Rankine cycle solar system

Compared with steam for the Rankine cycle, it has the following advantages:

- Small turbine head allows for moderate shaft speed and a single- or two-stage design.



- Low volume ratio facilitates the flow path design.
- High volume flow and low velocity of sound results in reasonable flow areas.
- Low temperature drop during expansion reduces thermal stress problems.
- Dry expansion avoids blade erosion caused by vapor wetness.
- Low system pressure facilitates housing design.

### 2.1.3 Solar chimney

Solar chimney, also known as solar updraft tower, directly (without concentration) uses the sun's heat to generate power. It uses solar radiation to increase the internal air temperature to form a flow to the chimney located at the middle of the roof. Fig. 2-6 shows the schematic of a typical solar chimney power plant. In this plant, air is heated by the green house effect under the translucent roof. As the roof is open at its periphery, air flows into the plant due to different density distribution. Hot air flows into the chimney because of buoyancy. An electricity-generating turbine is set in the path of the air current to convert the kinetic energy of the flowing air into electricity.

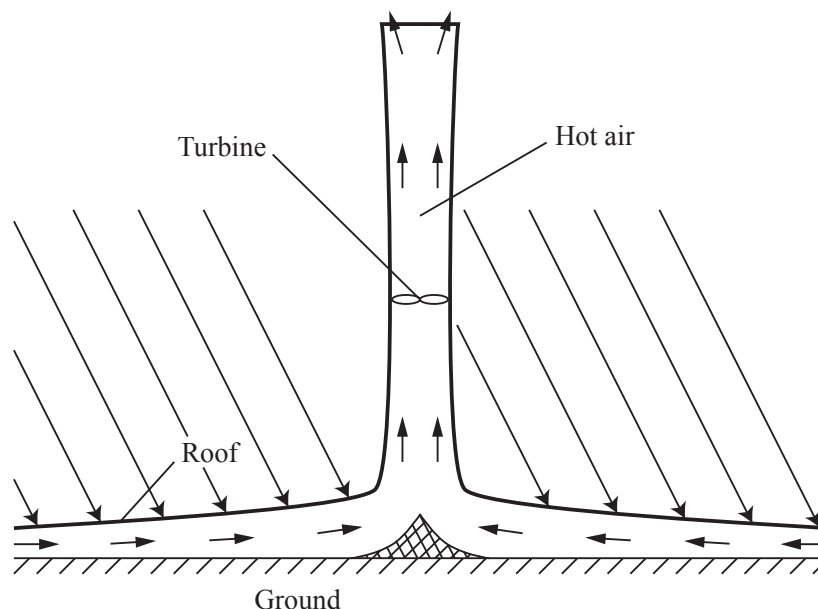


Figure 2-6 Schematic diagram of a solar chimney power plant

The solar chimney can use the low temperature (low grade energy) for power generation. So the combination of parabolic trough system and solar chimney is considered an

effective way for energy cascade utilization. In the combined system, the condenser in the Rankine cycle is air cooled. The fan blows the hot air that has cooled the condenser into the solar chimney power plant from its periphery. The hot air stream converges at the bottom of chimney, flows upward with the action of buoyancy and drives the turbine in the chimney. Energy of the hot air can be utilized by the solar chimney. Fig. 2-7 shows an example of the combined system.

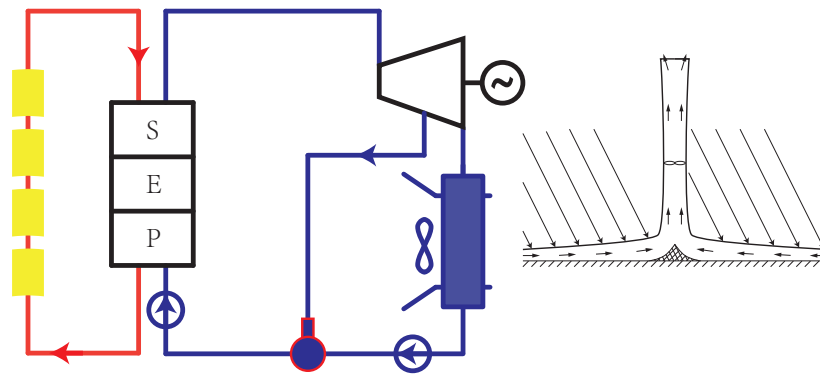


Figure 2-7 Schematic diagram of a combined solar trough and chimney power system

However, the efficiency of solar chimney system is very low. Primary design data of solar chimney power plants with different location, different chimney height and collector height are shown in Table 2.1<sup>[68]</sup>.

The preliminary design parameters in Table 2.1 are selected and determined for a nominal solar intensity of  $1000 \text{ W/m}^2$  and the nominal plant power of 5 MW. From the table, it can be found that the chimney efficiency and total efficiency are very low and the technology is still in the development stage.

#### 2.1.4 Collector series connection

Considering different heat collecting temperatures of different types of collectors, series connection of different types of collectors can be a feasible choice for solar cascade collection. Trough collectors and Fresnel collectors have better performance for lower temperature heat collection. Dish collectors and solar towers are more suitable for higher temperature heat collection. Serial connection utilize the advantages of different types of collectors. Figure 2-8 shows an example of a cascade system using collector series connection. In this system, air, the HTF, is preheated by parabolic collectors before it flows into the parabolic

Table 2.1 Results of SEA models under specified parameters

	Ottawa	Winnipeg	Edmonton	Schlaich
Collector diameter (m)	-	-	-	1110
Collector area (m <sup>2</sup> )	950000	950000	950000	950000
Chimney height (m)	123	60	35	547
Collector height (m)	848	975	1024	-
Chimney diameter (m)	54	54	54	54
Temperature rise in collector (°C)	25.9	25.9	25.9	25.9
Updraught velocity (m/s)	9.1	9.1	9.1	9.1
Total pressure head (Pa)	518.3	518.3	518.3	383.3
Average efficiency				
Collector (%)	56.00	56.00	56.00	56.24
Chimney (%)	1.82	1.82	1.82	1.45
Turbine (%)	77.0	77.0	77.0	77.0
Whole system (%)	0.79	0.79	0.79	0.63

dish collectors.

### 2.1.5 Direct steam generation

All commercial parabolic trough solar plants implemented to date use heat-transfer fluid (typically synthetic oil or melton salt) in the solar field. It leads to high pressure drop, limits the oil (or salt) related equipment operation, maintenance and cost. Besides, the highest temperature of the Rankine cycle is limited by the oil (or salt) temperature. So generating steam in the receiver tubes (direct steam generation, DSG) of the solar collector is one of the directions to reduce the cost and increase the efficiency of the PTC systems. Fig. 2-9 shows the schematic diagram of a typical DSG solar system.

Generating vapor in the receiver of the solar collector has the advantage of having fewer components and no loss of temperature required with an intermediate transfer. With both liquid and vapor in a receiver, however, extreme care must be taken in the design of the receiver

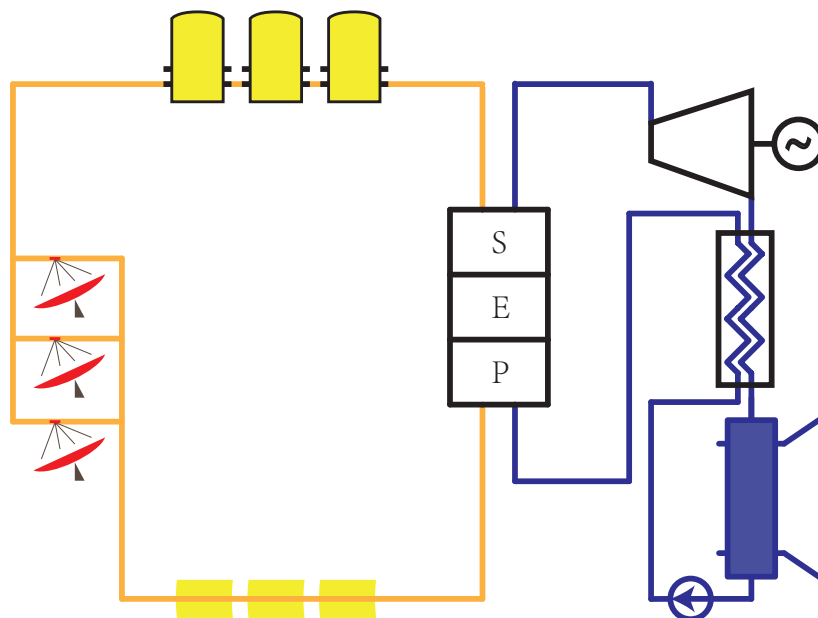


Figure 2-8 Schematic diagram of a cascade system using collector series connection

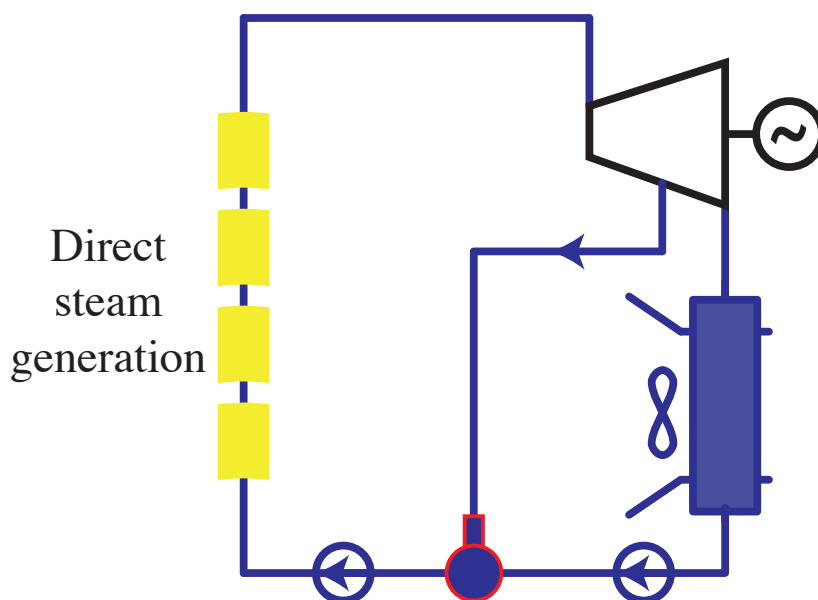


Figure 2-9 schematic diagram of a typical solar system using receiver vapor generator

to ensure that the radiant flux incident on that portion of the receiver containing vapor is less than the flux incident in the regions with liquid and where boiling is taking place. This is because the heat-transfer coefficient into a liquid is significantly higher than into super-

heated vapor. For similar values of solar flux, burnout of the receiver walls could occur in the regions where vapor exists on the other side of the receiver wall. Many concentrating collector designs require that the receiver change attitude while the collector tracks the sun. This change of attitude increases the chances of high flux on portions of the receiver containing vapor. Two examples of solar Rankine power systems where the engine working fluid vapor is generated directly in the receiver are the Solar One Pilot Plant at Barstow, CA and the solar organic Rankine cycle module built by Ford Aerospace and Communications Corporation. Because Solar One is a central receiver system, the vertical-tube receiver remains stationary and liquid level control is relatively easy. The vertical tubes of the receiver are made of a material with a high melting point and thus can withstand high temperatures in the upper regions where vapor is being superheated. Tube burnout is avoided in the Ford Aerospace receiver design because the inner wall of the receiver is a copper shell with tubes wound around its exterior. The high thermal conductivity of the copper shell provides an averaging effect on receiver temperature, and superheat is attained without burnout of the receiver walls.

### **2.1.6 Heat exchangers between different circuits**

Heat transfer between different circuits can be applied to cascade utilize the heat collected.

### **2.1.7 Heat recovery between different cycles**

## **2.2 System topology selection**

### **2.2.1 Rankine cycle fluid**

### **2.2.2 Solar chimney**

### **2.2.3 Collector series connection**

### **2.2.4 Direct steam generation**

### **2.2.5 Heat exchangers between different circuits**

## Chapter 3 System modeling

To investigate the performance of the proposed cascade systems, mechanism models of the systems were developed with EES (Engineering Equation Solver) and MATLAB. Bottom-up design method was used for the system modeling. Firstly, the mechanism models of the developed in EES to validate the theoretical relationships of the models. Secondly, the component models were developed in MATLAB by using object-oriented method. It makes full use of inheritance and polymorphism to ensure both the independence and the relevance of the components. Three circuits, air circuit, water circuit and oil circuit, were developed with some specific state parameters in some key components. Energy-based models of these key components were created on the basis of their thermodynamic behavior, heat transfer and the second law.

The following parts introduce models of some key components.

### 3.1 Component modeling

#### 3.1.1 Parabolic trough collector

Parabolic trough collector consists of a reflector and a receiver. The reflector (mirror) reflects direct solar radiation and concentrates it onto a receiver tube located in the focal line of the parabola. The receiver is typically a metal absorber tube with high absorption rate coating. An outer glass tube is used outside the absorber tube to reduce thermal losses and the space between the absorber tube and the glass tube is usually drawn into a vacuum to further reduce the thermal losses.

Optical loss exists in the reflection process due to optical efficiency terms. The reflection terms can be listed as bellow<sup>[5]</sup>:

- Shadowing factor
- Tracking error
- Geometry error
- Clean mirror reflectance
- Dirt on mirrors

- Unaccounted errors

Another term, incident angle modifier  $K(\theta)$ , should be concerned when the solar irradiation is not normal to the collector aperture. It is a function of the solar incidence angle to the normal of the collector aperture ( $\theta$ ).

The equation was determined from trough collector testing conducted at SNL<sup>[69]</sup>.

$$K(\theta) = \cos \theta + 0.000884\theta - 0.00005369\theta^2 \quad (3.1)$$

The optical losses are associated with five parameters (see fig. 3-1):

- Reflectivity,  $\rho$ : only a fraction of the incident radiation is reflected towards the receiver. The fraction is determined by the reflector type and dirt condition. Reflectivity of commercial parabolic trough mirrors can be assumed to be 0.9 for washed mirrors.
- Intercept factor,  $\gamma$ : a fraction of the direct solar radiation reflected by the mirrors does not reach the glass cover of the absorber tube due to either microscopic imperfections of the reflectors or macroscopic shape errors in the parabolic trough concentrators (e.g., imprecision during assembly). These errors cause reflection of some rays at the wrong angle, and therefore they do not intercept the absorber tube. These losses are quantified by an optical parameter called the intercept factor,  $\gamma$ , that is typically 0.95 for a collector properly assembled.
- Transmissivity of the glass tube,  $\tau$ : only a fraction of the direct solar radiation reaching the glass cover of the absorber pipe is able to pass through it. The ratio between the radiation passing through the glass tube and the total incident radiation on it, gives transmissivity  $\tau$ , which is typically 0.93.
- Absorptivity of the absorber selective coating,  $\alpha_{abs}$ : this parameter quantifies the amount of energy absorbed by the steel absorber pipe, compared with the total radiation reaching the outer wall of the steel pipe. This parameter is typically 0.95 for receiver pipes with a cermet coating, whereas it is slightly lower for pipes coated with black nickel or chrome.
- Soiling factor,  $F_e$ : because of the dirt on reflectors will reduce the reflectivity, it needs to concern the soiling factor. The soiling factor  $F_e$  takes into account the progressive soiling of mirrors and glass tubes after washing.

The energy pass through the glass tube to the receiver can be obtained by

$$P = I_r w_{tc} L_{tc} \rho \gamma \tau F_e K(\theta) \quad (3.2)$$

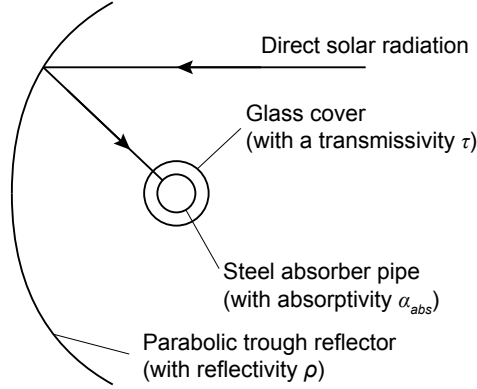


Figure 3-1 Some of the optical parameters of a parabolic trough

The solar energy absorbed by the absorber occurs very close to the outer surface, to simplify the absorption process, it is treated as a uniform heat flux  $q''$ .

$$q'' = \frac{P}{\pi d_o L_{tc}} = \frac{I_r w_{tc} \rho \gamma \tau F_e K(\theta)}{\pi d_o} \quad (3.3)$$

Assume overall heat transfer coefficient  $U(T_{abs})$  is uniform for whole length of the collector, and the heat transfer correlation in Appendix B can be used. Figure 3-2 shows the schematic diagram of the thermal analysis of the absorber pipe.

$$\frac{T_o - T_{amb} - \frac{q''}{U(T_{abs})}}{T_i - T_{amb} - \frac{q''}{U(T_{abs})}} = \exp\left(-\frac{U(T_{abs})PL}{\dot{m}c_p}\right) \quad (3.4)$$

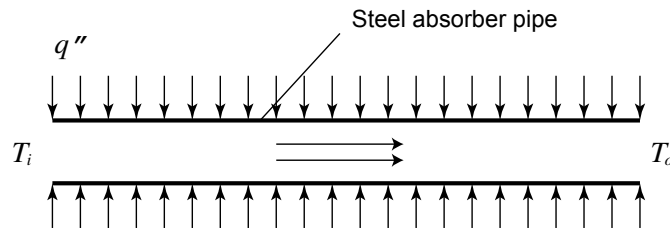


Figure 3-2 Schematic diagram of the absorber pipe

Since the Nusselt number  $Nu$  in the pipe is very large (about  $1 \times 10^4$ ), small temperature difference exists between the absorber and oil. So the average fluid temperature  $(T_i + T_o)/2$  can be used as the average value of  $T_{abs}$ , and  $U(T_{abs})$  can be obtained by the a second-order polynomial function given by Romero<sup>[70]</sup>. The length  $L$  required to get the required number of trough collectors in a row can be obtained from Equation (3.4).



### 3.1.2 Parabolic dish collector

Parabolic dish collector consists of a reflector and a receiver. The reflector (mirror) tracks the sun to reflect direct solar radiation and concentrates it onto a receiver located at the focal point of the reflector. Two axes tracking system needs to be applied for the reflector to continuously follow the daily path of the sun.

In a traditional dish-Stirling system, a Stirling engine is located at the focal point. The Stirling engine has a receiver to absorb the thermal energy from the concentrated sunlights. The receiver consists of an aperture and an absorber. The aperture in a Stirling receiver is located at the focal point of the reflector to reduce the radiation and convection losses. The absorber absorbs the solar radiation and transfers the thermal energy to the working gas of the Stirling engine. An electrical generator, directly connected to the crankshaft of the engine, converts the mechanical energy into electricity.

In the proposed cascade system, a volumetric receiver is located on the focal point. Spiral tube is located in the receiver to absorb the concentrated solar energy. Air (or nitrogen, is used as the heat transfer fluid) flows through the tube to transfer the absorbed energy as the heat source of Stirling engine(s).

The reflector is a key element of the systems. The curved reflective surface can be manufactured by attached segments, by individual facets or by a stretched membranes shaped by a continuous plenum. In all cases, the curved surface should be coated or covered by aluminum or silver reflectors.

Two different methods<sup>[71]</sup> are applied for the sun tracking systems:

- Azimuth elevation tracking by an orientation sensor or by calculated coordinates of the sun performed by the local control.
- Polar tracking, where the concentrator rotates about an axis parallel to the earth's axis rotation.

A dish reflector product of SES (Stirling Energy System) is used in this cascade system, and its key parameters can be found in Table 3.1. The structure of the receiver is shown in fig. 3-3.

The dish receiver model concerns the losses include: collector losses due to mirror reflectivity, receiver intercept losses, losses due to shading, and thermal losses. Thermal losses take the largest portion of all those losses, which are due to conduction, convection

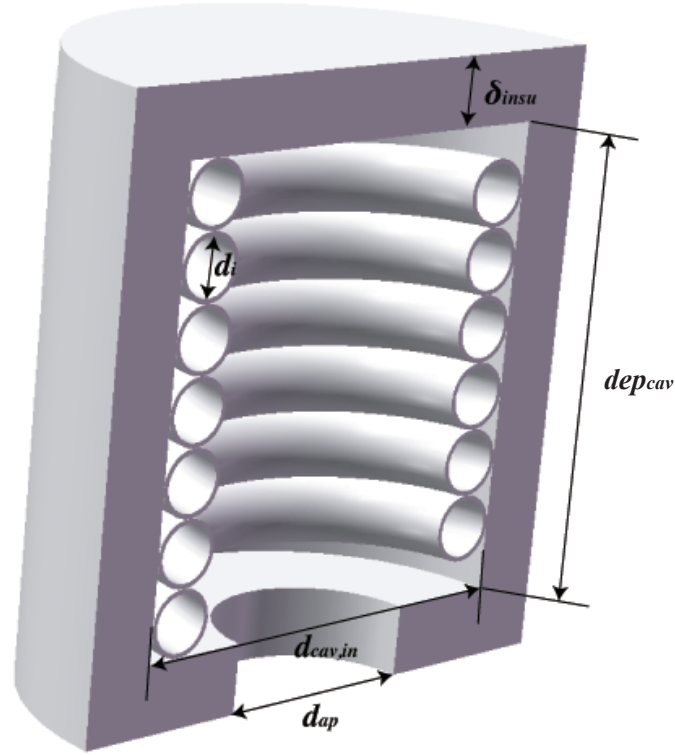


Figure 3-3 The structure of the dish receiver

and radiation. Figure 3-4 shows the thermal network of dish receiver, which concerns the losses:

- Radiation losses reflected off of the receiver cavity surfaces and out of the receiver through the aperture. ( $q_{rad,ref}$ )
- Conductive losses through the receiver insulating layer. ( $q_{cond,tot}$ )
- Free convection from the cavity in the absence of wind. ( $q_{conv,free}$ )
- Forced convection in the presence of wind. ( $q_{conv,forc}$ )
- Emission losses due to thermal radiation emitted from the receiver aperture. ( $q_{rad,emit}$ )

To solve the thermal network in fig. 3-4, correlations and relationships of the heat fluxes should be clear.

1. *Inlet energy from the reflector,  $q_i$*

To simplify the model, influences made by receiver blocking and imperfection track

Table 3.1 Key parameters of the dish collector

Parameter	Value	Parameter	Value	Parameter	Value
$d_{cav}$	0.46 m	$\epsilon_{insu}$	0.6	$\theta_{dc}$	45°
$\delta_{insu}$	0.075 m	$\alpha_{cav}$	0.87	$\gamma$	0.97
$dep_{cav}$	0.23 m	$\delta_a$	0.005 m	$\eta_{shading}$	0.95
$d_{ap}$	0.184 m	$d_{i,1}$	0.07 m	$\rho$	0.91
$\lambda_{insu}$	0.06 W/(m · K)	$A_{dc}$	87.7 m <sup>2</sup>		

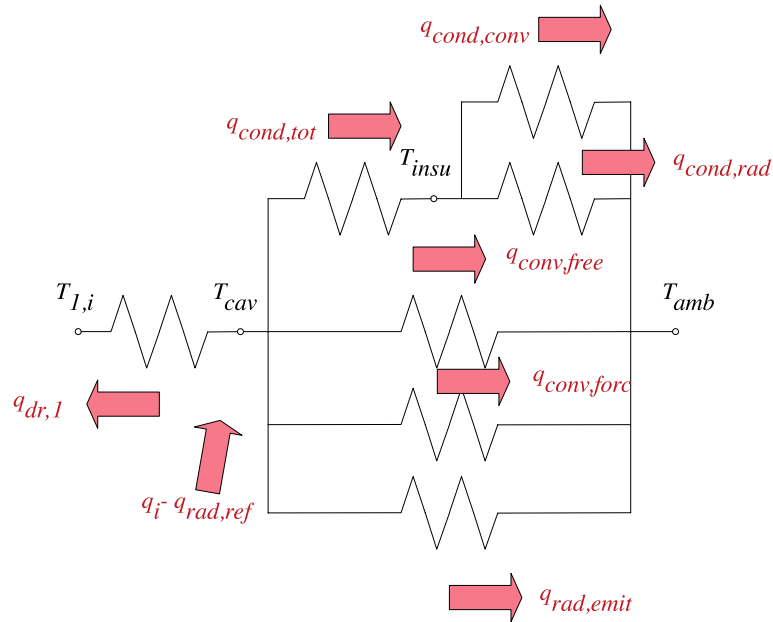


Figure 3-4 Thermal network of dish receiver

are ignored.

$$q_i = I_r A_{dc} \gamma \eta_{shading} \rho \quad (3.5)$$

In equation 3.5,  $\gamma$  is the intercept factor,  $\eta_{shading}$  is the shading factor between different collectors,  $\rho$  is the reflectivity of the reflector.

2. *Heat exchange between the HTF and the dish absorber,  $q_{dr,1}$*

The heat transfer process between the HTF and the dish absorber is simplified to a heat exchange process of a flow in a uniform temperature heat pipe. So  $q_{dr,1}$  can be written as

$$q_{dr,1} = h_{dr,1} A_{dr,1} \Delta T_{ln,dr,1} \quad (3.6)$$

where

$$h_{dr,1} = Nu_{tube} \lambda_{dr,1} / d_{i,1} \quad (3.7)$$

$$Nu_{tube} = c_r Nu'_{tube} \quad (3.8)$$

For helical spiral pipe, multiplier  $c_r$  based on curvature ratio can be written as<sup>[72]</sup>

$$c_r = 1 + 3.5 \frac{d_{i,1}}{d_{cav} - d_{i,1} - 2\delta_a} \quad (3.9)$$

$Nu'_{tube}$  is the Nusselt number of straight circular tube, which can be obtained by<sup>[73]</sup>

$$Nu'_{tube} = 0.027 Re_{tube}^{0.8} Pr_{tube}^{1/3} (\mu_{tube} / \mu_{tube,w})^{0.14} \quad (3.10)$$

and the logarithmic mean temperature difference  $\Delta T_{ln,dr,1}$  can be written as

$$\Delta T_{ln,dr,1} = \frac{(T_{cav} - T_{dc,i}) - (T_{cav} - T_{dc,o})}{\ln \frac{T_{cav} - T_{dc,i}}{T_{cav} - T_{dc,o}}} \quad (3.11)$$

3. *Radiation losses reflected off the receiver,  $q_{rad,ref}$*

$$q_{rad,ref} = (1 - \alpha_{eff}) q_i \quad (3.12)$$

where  $\alpha_{eff}$  is the effective absorptivity of the receiver.

$$\alpha_{eff} = \frac{\alpha_{cav}}{\alpha_{cav} + (1 - \alpha_{cav}) \frac{A_{ap}}{A_{cav}}} \quad (3.13)$$

$\alpha_{cav}$  is the absorptivity of the cavity,  $A_{cav}$  is the cavity area,  $A_{ap}$  is the aperture area.

4. *Conductive losses through the receiver insulating layer,  $q_{cond,tot}$*

$$q_{cond,tot} = 2\pi\lambda_{insu}dep_{cav} \frac{T_{cav} - T_{insu}}{\ln((d_{cav} + 2\delta_{insu})/d_{cav})} \quad (3.14)$$

where  $T_{cav}$  is the temperature of the cavity wall,  $T_{insu}$  is outside temperature of the insulation wall.

5. *Convection losses from the receiver insulating layer,  $q_{cond,conv}$*

$$q_{cond,conv} = h_{insu}A_{insu}(T_{insu} - T_{amb}) = \frac{k_{insu}Nu_{insu}A_{insu}(T_{insu} - T_{amb})}{d_{cav} + 2\delta_{insu}} \quad (3.15)$$

where  $Nu_{insu}$  can be obtained by the correlation for flow over a circular cylinder.<sup>[74]</sup>

6. *Radiation losses from the receiver insulating layer,  $q_{cond,rad}$*

$$q_{cond,rad} = \epsilon_{insu}A_{insu}\sigma(T_{insu}^4 - T_{amb}^4) \quad (3.16)$$

7. *Free convection from the cavity in the absence of wind,  $q_{conv,free}$*

Ma<sup>[75]</sup> conducted tests to determine the free convection losses from the receiver for alternative setups, and the data were consistent with Stine and McDonald's free convection correlation. It is assumed that forced convection is independent of free convection in the receiver, so the total convection losses can be represented as the total of the free and forced convection losses as shown in Figure 3-4.

$$q_{conv,free} = h_{free}A_{cav}(T_{cav} - T_{amb}) \quad (3.17)$$

where  $h_{free} = k_{film}Nu_{free}/\overline{d_{cav}}$ ,  $\overline{d_{cav}}$  is the effective diameter of the cavity,  $\overline{d_{cav}} = d_{cav} - 2d_i - 4\delta_a$ .  $d_i = 0.066$  m

8. *Force convection from the cavity in the presence of wind,  $q_{conv,forc}$*

$$q_{conv,forc} = h_{forc}A_{cav}(T_{cav} - T_{amb}) \quad (3.18)$$

Wu<sup>[76]</sup> present a comprehensive review and systematic summarization of convection heat loss from cavity receiver in parabolic dish solar thermal power system. And we choose the correlation presented by Leibfried<sup>[77]</sup>. This correlation gives an extended model of Koenig<sup>[78]</sup> and Stine<sup>[79]</sup> with better results.

For forced convection loss, side-on wind convection loss model given by Ma<sup>[75]</sup>, which is independent of the aperture orientation, is used

$$h_{forc} = 0.1967v_{wind}^{1.849} \quad (3.19)$$

9. *Emission losses due to thermal radiation emitted from the receiver aperture,  $q_{rad,emit}$*

The emissivity is set equal to the effective absorptivity of the cavity (gray body),

$$\epsilon_{cav} = \alpha_{eff} \quad (3.20)$$

$$q_{rad,emit} = \epsilon_{cav} A_{ap} \sigma (T_{cav}^4 - T_{amb}^4) \quad (3.21)$$

From fig 3-4, it can be found that

$$q_{dr,1} = q_i - q_{rad,ref} \quad (3.22)$$

$$q_{dr,1} = q_{cond,tot} + q_{conv,free} + q_{conv,forc} + q_{rad,emit} \quad (3.23)$$

$$q_{cond,tot} = q_{cond,conv} + q_{cond,rad} \quad (3.24)$$

So the temperature nodes in the thermal network can be solved by these equations.

$q_{dr,1}$  can be obtained by Equation 3.6.

### 3.1.3 Stirling engine

#### 3.1.3.1 Theoretical Stirling cycle

In a Stirling cycle, there are two isothermal processes that exchange heat with heating and cooling fluids, two isochoric processes that exchange heat with regenerator. In Figure 3-5, the heat absorbed by regenerator in process 4-1 is reused in process 2-3, but only able to heat the working gas from 2 to 3' due to the imperfect regeneration.  $e$  is defined as the regenerator effectiveness<sup>[80,81]</sup>,  $e = \frac{T_R - T_L}{T_H - T_L}$ , where  $T_H$  is the temperature in the hot space,  $T_L$  is the temperature in the cold space,  $T_R$  is the effective working fluid temperature in the regenerator.

In order to obtain a simplified analytical model, several simplifications were made:

- The working gas in Stirling engines obeys the idea gas law.
- No heat loss to the environment for Stirling engines.
- Overall heat transfer coefficients of the fluids are constant.

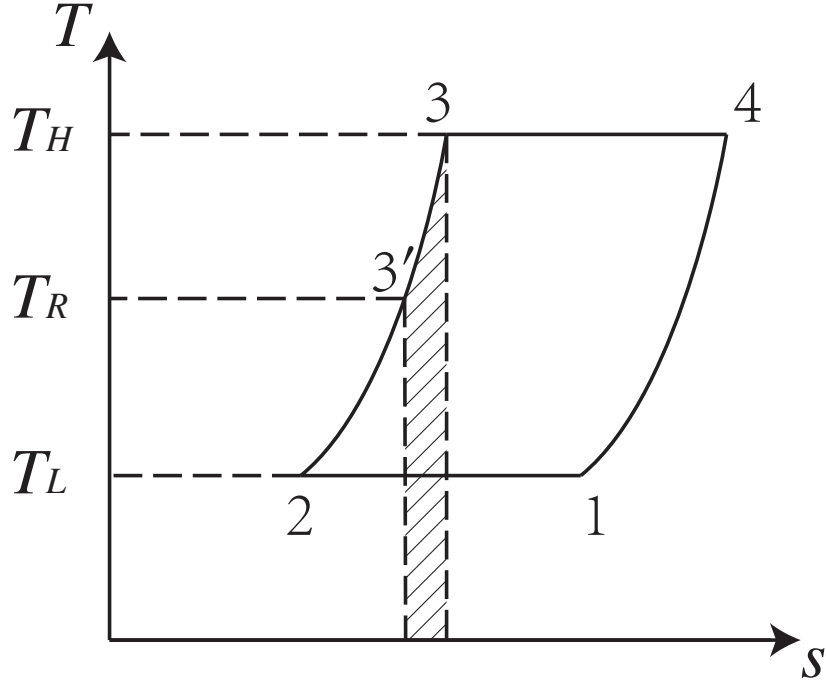


Figure 3-5  $T$ - $s$  diagram of a Stirling cycle

- A symmetrical regenerator behavior is assumed<sup>[80,81]</sup> so that a simple effectiveness can be obtain by  $T_R = \frac{T_H - T_L}{\ln(T_H/T_L)}$ .

To consider internal irreversibilities in Stirling cycle made by dead volumes, as described in Duan's paper<sup>[82]</sup>, total dead volume  $V_D$  is divided into heater dead volume  $V_{DH}$ , regenerator dead volume  $V_{DR}$  and cooler dead volume  $V_{DC}$ . There exists a factor  $K$  to describe the dead volumes under different temperatures.  $K$  is relevant with temperatures in the process and regenerator effectiveness.

$$K = \frac{V_{DH}}{T_H} + \frac{V_{DR}}{T_R} + \frac{V_{DC}}{T_L} \quad (3.25)$$

For the isothermal compression process 1-2, the output work

$$W_{12} = \int_{V_E+V_C}^{V_E} p_{12} dV = -mRT_L \ln \frac{V_E + V_C + KT_L}{V_E + KT_L} \quad (3.26)$$

For the isothermal expansion process 3-4, the output work

$$W_{34} = \int_{V_E}^{V_E+V_C} p_{34} dV = mRT_H \ln \frac{V_E + V_C + KT_H}{V_E + KT_H} \quad (3.27)$$

Define  $\gamma_H = \frac{V_E+V_C+KT_H}{V_E+KT_H}$ , and  $\gamma_L = \frac{V_E+V_C+KT_L}{V_E+KT_L}$ , so in a cycle, the theoretical output work

$$W_{th} = W_{12} + W_{34} = mR(T_H \ln \gamma_H - T_L \ln \gamma_L) \quad (3.28)$$

For the isochoric heating process 3'-3, the absorbed heat

$$Q_{3'3} = nc_v(T_H - T_L) = \frac{1-e}{k-1} mR(T_H - T_L) \quad (3.30)$$

For the the isothermal expansion process 3-4, the absorbed heat

$$Q_{34} = W_{34} = mRT_H \ln \gamma_H \quad (3.31)$$

In a cycle, the theoretical absorbed heat

$$Q_{th} = Q_{3'3} + Q_{34} = \frac{1-e}{k-1} mR(T_H - T_L) + mRT_H \ln \gamma_H \quad (3.32)$$

### 3.1.3.2 Irrevisibilities and losses

#### 1. Non-ideal heat transfer effect

Because of non-ideal heater and cooler, the working fluid temperature ( $T_H/T_L$ ) in these two heat exchangers is less/higher than the wall temperature ( $T_{hw}/T_{cw}$ ), respectively. And  $T_H$  and  $T_L$  can be corrected by the wall temperatures as follows:

$$T_H = T_{hw} - \frac{Q s_{se}}{h_h A_{hw}} \quad (3.33)$$

$$T_L = T_{cw} + \frac{(Q - W) s_{se}}{h_c A_{cw}} \quad (3.34)$$

The heat transfer coefficient can be obtained using the following correlation<sup>[1]</sup>:

$$h_{h,c} = \frac{\mu c_p f_{Re}}{2D_{h,c} Pr_{h,c}} \quad (3.35)$$



where  $f_{Re}$  is a Reynolds friction factor defined as:

$$f_{Re} = 0.0791 Re_{h,c}^{0.75} \quad (3.36)$$

$Re_{h,c}$ ,  $Pr_{h,c}$  and  $D_{h,c}$  are Reynolds number, Prandtl number and hydraulic diameter of the heater/cooler exchanger.

## 2. Effect of pressure drop

Pressure drops in the heat exchangers cause power losses of the Stirling engine. The pressure drops can be obtained by<sup>[83]</sup>:

$$\Delta p = -\frac{2f_{Re}\mu uV}{d^2A} \quad (3.37)$$

where  $u$  is the working gas speed,  $V$  is volume,  $A$  is flow cross-section area.

The net power loss of the Stirling engine due to pressure drop of the heat exchangers can be evaluated by:

$$W_{pd} = \oint \sum_{i=E,C} (\Delta p_i \frac{dV_i}{d\theta}) d\theta \quad (3.38)$$

## 3. Effect of finite speed of piston and mechanical friction

Due to the finite speed of piston, the pressure on the piston surface is different from the pressure of expansion and compression spaces. It has been demonstrated that the pressure on the piston surface in the expansion process is less than the mean pressure in the expansion space. Similarly, the pressure on the piston surface in the compression process is greater than the mean pressure in the compression space. This means the output work is less than the theoretical value. Besides, The output work also reduces due to mechanical friction. The output work loss due to finite speed of piston and mechanical friction can be obtained as follows<sup>[1]</sup>:

$$W_{fs} = \oint p(\pm \frac{au_p}{c} \pm \frac{\Delta p_f}{p}) dV \quad (3.39)$$

where the sign (+) is used in the compression space, and the sign (-) is used in the expansion space.  $p$  is the mean pressure in the compression/expansion space,  $u_p$  is velocity of the piston,  $c$  is the average speed of molecules and  $\Delta p_f$  is the pressure loss due to mechanical friction.  $\Delta p_f$ ,  $a$  and  $c$  can be obtained by<sup>[84]</sup>:

$$\Delta p_f = 0.97 + 0.009s_{se} \quad (3.40)$$

$$a = \sqrt{3k} \quad (3.41)$$

$$c = \sqrt{3RT} \quad (3.42)$$

#### 4. Energy losses due to internal conduction

The temperature differs from the heater and cooler, heat losses from heater to cooler exists due to internal conduction through the walls of regenerator.<sup>[85]</sup> The internal conduction loss in a cycle can be obtained by follows:

$$Q_{id} = \frac{k_r A_r}{L_r s_{se}} (T_{hw} - T_{cw}) \quad (3.43)$$

where,  $k_r$ ,  $A_r$  and  $L_r$  denote the regenerator matrix conductivity, regenerator length, and regenerator conductive area respectively.

#### 5. Energy losses due to shuttle conduction

The displacer shuttles between the expansion and compression space. It absorbs heat during the hot end of its stroke and releases it during the cold end of its stroke. This heat loss can be estimated as<sup>[86]</sup>:

$$Q_{sc} = 0.4 \frac{Z^2 k_p D_p}{J L_d s_{se}} (T_H - T_L) \quad (3.44)$$

where,  $Z$ ,  $k_p$ ,  $D_p$ ,  $J$  and  $L_d$  denote the displacer stroke, piston thermal conductivity, displacer diameter, gap between the displacer and the cylinder, and length of the displacer respectively.

So, in a Stirling engine, the total absorbed heat in a cycle

$$Q = Q_{th} + Q_{id} + Q_{sc} \quad (3.45)$$

the output work

$$W = W_{th} - W_{pd} - W_{fs} \quad (3.46)$$

Power of the Stirling engine

$$P = W s_{se} \quad (3.47)$$

Efficiency of the Stirling engine

$$\eta = W/Q \quad (3.48)$$

### 3.1.3.3 Model validation

Evaluation of the developed thermal model was performed by considering the GPU-3 Stirling engine as a case study. Design specifications of the GPU-3 Stirling engine are indicated in Table 3.2. The thermal efficiency and power of the proposed Stirling engine model was compared with previous thermal models and experimental data as shown in Table 3.3 and Table 3.4.

It can be found that the proposed model has much better agreement with the experimental results than previous thermal models at various rotation speeds and mean effective pressures. It is required to mention that in all thermal models both power  $W$  and input heat  $Q$  were determined by the thermal process of heat transfer between the wall and working gas. In the proposed model,  $W$  and  $Q$  are obtained by Equation 3.33 and 3.34. Therefore all the three parameters  $W$ ,  $Q$  and  $\eta$  are determined by the thermal model and input parameters to the model. These input parameters includes heater, cooler, mean effective pressure, type of working gas and geometrical specification of the engine.

Table 3.3 and 3.4 indicate that when mean effective pressure of the engine increases from 2.76 MPa to 6.90 MPa, best performance (efficiency and power) prediction of the proposed model exists. When rotation speed increases from 16.67 Hz to 58.33 Hz, error in prediction of performance of the proposed model increases. The proposed model may have the best performance prediction at a low rotation speed, with mean effective pressure between 4.14 MPa and 5.52 MPa.

However, there is still some discrepancy between the the simulation results of proposed model and the experimental data. In the future researches, more accurate models of Stirling engine may be developed by considering other irreversibilities such as heat loss to the environment, gas spring hysteresis, and etc. It is worth pointing that there are more accurate Stirling engine models. For example, polytropic simulation models of Stirling engine show higher accuracy than our proposed model<sup>[1,87]</sup>. However, the model needs more costly calculations and the polytropic indexes are engine-specific.

### 3.1.3.4 Heat transfer between the engine and the fluids

For a Stirling engine thermal process, the wall temperatures of the heater and cooler are considered to be uniform and constant. The heat transferred between the wall and the fluids

Table 3.2 Design specifications of the GPU-3 Stirling engine<sup>[1,2]</sup>

Parameter	Value
Engine type	$\beta$
Working gas	Helium
Mass of the working gas	1.136 g
<i>Heater</i>	
Number of tubes	40
Tube external diameter	$4.83 \times 10^{-3}$ m
Tube internal diameter	$3.02 \times 10^{-3}$ m
Tube length (cylinder side)	0.1164 m
Tube length (regenerator side)	0.1289 m
<i>Cooler</i>	
Number of tubes	312
Tube external diameter	$1.59 \times 10^{-3}$ m
Tube internal diameter	$1.09 \times 10^{-3}$ m
Average tube length	$4.61 \times 10^{-2}$ m
<i>Regenerator</i>	
Number of regenerator	8
Regenerator internal diameter	$2.26 \times 10^{-2}$ m
Regenerator length	$2.26 \times 10^{-2}$ m
Diameter of regenerator tube	$4 \times 10^{-5}$ m
Material	Stainless steel
<i>Volume</i>	
Swept Vol. (expansion/compression)	120.82/114.13 cm <sup>3</sup>
Clearance Vol. (expansion/compression)	30.52/28.68 cm <sup>3</sup>
Dead Vol. (heater/cooler/regenerator)	70.28/13.18/50.55 cm <sup>3</sup>

Table 3.3 Thermal efficiency of the models and experimental data (at  $T_{hw} = 922\text{ K}$  and  $T_{cw} = 288\text{ K}$ )

Rotation speed (Hz)	Mean effective pressure (MPa)	The simple analysis (variable $Pr^{[83]}$ )			The adiabatic analysis (simple $\Pi^{[85]}$ )			The proposed Stirling engine model			Experimental efficiency <sup>[1]</sup>
		Value (%)	Error (%)	Average error (%)	Value (%)	Error (%)	Average error (%)	Value (%)	Error (%)	Average error (%)	
16.67		38.72	18.22		32.48	11.98		28.16	7.66		20.50
25.00		36.16	15.46		31.21	10.51		27.75	7.05		20.70
33.33		33.79	15.79		29.45	11.45		27.43	9.43		18.00
41.67	2.76	31.48	16.28	17.90	27.45	12.25	12.85	27.17	11.97	12.10	15.20
50.00		29.12	17.32		25.21	13.41		26.94	15.14		11.80
58.33		29.74	24.34		22.89	17.49		26.74	21.34		5.40
25.00		35.65	10.85		32.29	7.49		27.29	2.49		24.80
33.33		33.52	9.62		30.40	6.50		26.94	3.04		23.90
41.67	4.14	31.48	10.18	11.46	28.39	7.09	8.28	26.65	5.35	6.65	21.30
50.00		29.45	11.25		26.33	8.13		26.39	8.19		18.20
58.33		27.40	15.40		24.21	12.21		26.17	14.17		12.00
41.67		31.20	8.70		28.59	6.09		26.24	3.74		22.50
50.00	5.52	29.33	10.53	10.82	26.62	7.82	8.11	25.97	7.17	7.48	18.80
58.33		27.44	13.24		24.62	10.42		25.73	11.53		14.20
50.00		29.07	10.37		26.61	7.91		25.62	6.92		18.70
58.33	6.90	27.29	13.09	11.73	24.67	10.47	9.19	25.37	11.17	9.05	14.20

Table 3.4 Output power of the models and experimental data (at  $T_{hw} = 922\text{ K}$  and  $T_{cw} = 288\text{ K}$ )

Rotation speed (Hz)	Mean pressure (MPa)	The simple analysis (variable Pr <sup>[83]</sup> )			The adiabatic analysis (simple II <sup>[85]</sup> )			The proposed Stirling engine model			Experiment (kW) <sup>[1]</sup>
		Value (kW)	Error (%)	Average error (%)	Value (kW)	Error (%)	Average error (%)	Value (kW)	Error (%)	Average error (%)	
16.67		1.796	119.02		1.772	116.10		0.861	4.98		0.82
25.00		2.555	128.13		2.500	123.21		1.253	11.88		1.12
33.33		3.215	165.70		3.117	157.60		1.632	34.88		1.21
41.67	2.76	3.769	211.49	272.03	3.615	198.76	254.71	2.001	65.37	104.84	1.21
50.00		4.195	303.37		3.973	282.08		2.362	127.12		1.04
58.33		4.505	704.46		4.203	650.54		2.715	384.82		0.56
25.00		3.844	114.75		3.761	110.11		1.818	1.56		1.79
33.33		4.856	120.73		4.708	114.00		2.362	7.36		2.20
41.67	4.14	5.734	136.94	259.70	5.501	127.31	158.41	2.890	19.42	39.83	2.42
50.00		6.462	174.98		6.126	160.68		3.405	44.89		2.35
58.33		7.030	306.36		6.573	279.94		3.908	125.90		1.73
41.67		7.645	133.08		7.334	123.60		3.742	14.09		3.28
50.00	5.52	8.655	163.87	180.02	8.206	150.18	164.91	4.401	34.18	43.68	3.28
58.33		9.470	243.12		8.858	220.94		5.045	82.79		2.76
50.00		10.788	174.50	287.04	10.223	160.13	263.63	5.362	36.44	97.75	3.93
58.33	6.90	11.840	399.58		11.071	367.13		6.140	159.07		2.37

is

$$(T_w - T)UdA = q_m c_p dT \quad (3.49)$$

with  $T(0) = T_i$ ,  $T(A) = T_o$ ,

$$\frac{T_o - T_w}{T_i - T_w} = \exp\left(-\frac{UA}{q_m c_p}\right) \quad (3.50)$$

For a Stirling engine,  $T_{hw}$  or  $T_{cw}$  can be used to substitute  $T_w$  to get the relationships between  $T_{i,h}$ ,  $T_{o,h}$  and  $T_{hw}$ , or  $T_{i,c}$ ,  $T_{o,c}$  and  $T_{cw}$  respectively.

$$\frac{T_{o,h} - T_{hw}}{T_{i,h} - T_{hw}} = \exp\left(-\frac{U_h A_h}{q_{m,h} c_{p,h}}\right) \quad (3.51)$$

$$\frac{T_{o,c} - T_{cw}}{T_{i,c} - T_{cw}} = \exp\left(-\frac{U_c A_c}{q_{m,c} c_{p,c}}\right) \quad (3.52)$$

Heat transferred from heating fluid to Stirling engine in a cycle

$$q_{m,h} c_{p,h} (T_{i,h} - T_{o,h}) / s_{se} = Q \quad (3.53)$$

Heat transferred from Stirling engine to cooling fluid in a cycle

$$q_{m,c} c_{p,c} (T_{o,c} - T_{i,c}) / s_{se} = Q - W \quad (3.54)$$

### 3.1.4 Steam generating system

The steam generating system can be divided into preheater, evaporator, superheater, they are collectively referred to as PES. They are all heat exchangers. It is assumed that, in these heat exchangers, the pressure of the fluid does not change significantly. It can be assumed to be equal to the pressure of the inlet pressure of the turbine. To clearly understand the modeling of these heat exchangers, an example of steam generating system as shown in fig 3-6 is used for explanation.

#### 1. Preheater

The outlet of the heated fluid is saturated liquid ( $x = 0$ ), so the outlet temperature  $T_{2i}$  and outlet enthalpy  $h_{2i}$  of the heated fluid are determined by the main pressure of the turbine,  $p_s$ .

$$\dot{m}_3 (h_{3c} - h_{3d}) = \dot{m}_2 (h_{2i} - h_{2h}) \quad (3.55)$$

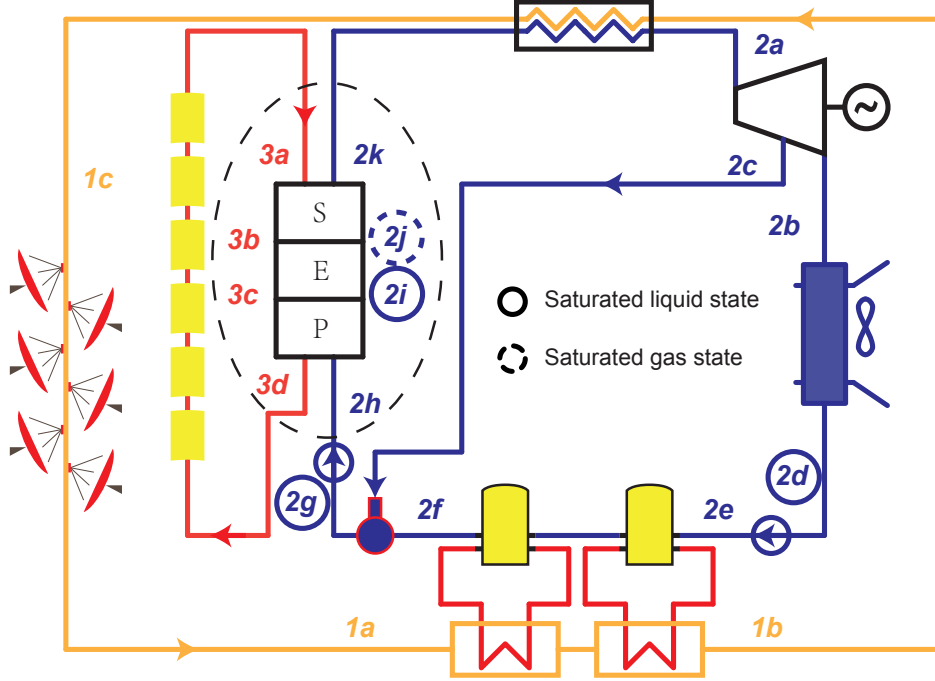


Figure 3-6 An example of steam generating system in a cascade system

## 2. Evaporator

The outlet of the heated fluid is saturated gas ( $x = 1$ ), so the outlet temperature  $T_{2j}$  and outlet enthalpy  $h_{2j}$  of the heated fluid are determined by the main pressure of the turbine,  $p_s$ .

$$\dot{m}_3(h_{3b} - h_{3c}) = \dot{m}_2(h_{2j} - h_{2i}) \quad (3.56)$$

## 3. Superheater

$$\dot{m}_3(h_{3a} - h_{3b}) = \dot{m}_2(h_{2k} - h_{2j}) \quad (3.57)$$

### 3.1.5 Rankine power generation system

The Rankine power generation system consists of turbine, condenser, deaerator, generator and pumps. Based on different working fluids, there are two different kinds of Rankine power generation systems, steam Rankine power generation system and organic Rankine power generation.



### 3.1.5.1 Steam Rankine cycle

For steam Rankine cycle, deaerator is used to remove the oxygen and other non-condensable gases in the feedwater to steam generating system. Dissolved oxygen in feedwater will cause serious corrosion damage in steam generating system by forming oxides (rust) of the metal pipes. Dissolved carbon dioxide combines with water to form carbonic acid will cause further corrosion. The accumulation of the non-condensable gases will increase the heat transfer resistance, which is harmful for the heat exchangers. The extraction of the steam turbine provides heat for the deaerator.

Figure 3-7a shows the  $T$ - $s$  diagram of the water circuit in the cascade system in fig 3-6. Process  $2a$ - $2c$ - $2b$  shows the heat process in the steam turbine. (see fig. 3-7b) State point  $2b$  and  $i, 2b$  have the same pressure, state point  $2c$  and  $i, 2c$ . To simplify the inner process  $2a$ - $2c$ - $2b$  of the turbine, same isentropic efficiency of steam turbine with different loads and in different stages is assumed, which means

$$\eta_{i,tb} = (h_{2a} - h_{2b}) / (h_{2a} - h_{i,2b}) = (h_{2a} - h_{2c}) / (h_{2a} - h_{i,2c}) \quad (3.58)$$

where  $h_{i,2b}$  is determined by  $s_{2a}$  and  $p_c$ ;  $h_{i,2c}$  is determined by  $s_{2a}$  and  $p_e$ .

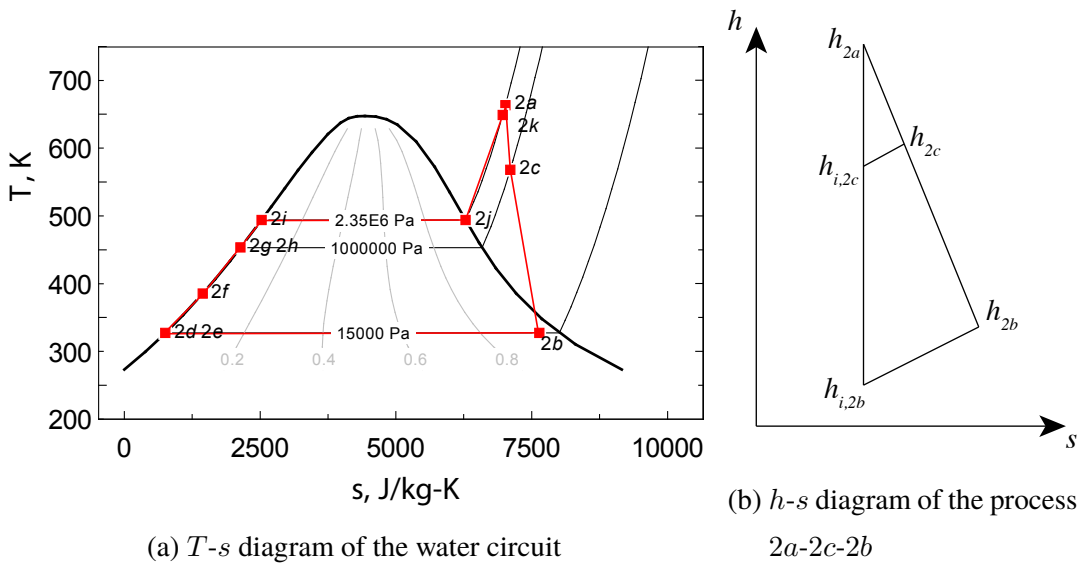


Figure 3-7  $T$ - $s$  diagram of the water circuit and  $h$ - $s$  diagram of the process  $2a$ - $2b$

The output power of the steam turbine

$$P_{tb} = (1 - y) \dot{m}_2 (h_{2a} - h_{2b}) + y \dot{m}_2 (h_{2a} - h_{2c}) \quad (3.59)$$

Process  $2b-2d$  shows the heat process in the condenser. The outlet water in the condenser is saturated water. The outlet temperature  $T_{2d}$  and outlet enthalpy  $h_{2d}$  are determined by the exhaust pressure of the turbine  $p_c$ . The released heat of the condenser

$$Q_{cd} = (1 - y) \dot{m}_2 (h_{2b} - h_{2d}) \quad (3.60)$$

State points  $2c$ ,  $2f$  and  $2g$  have the same pressure ( $p_e$ , 1 MPa). The water at the outlet of the deaerator is saturated fluid, its enthalpy is determined.

$$y h_{2c} + (1 - y) h_{2f} = h_{2g} \quad (3.61)$$

The total power of the pumps

$$P_{pu} = (1 - y) \dot{m}_2 (h_{2e} - h_{2d}) + \dot{m}_2 (h_{2h} - h_{2g}) \quad (3.62)$$

where  $h_{2e}$  can be obtained by  $\eta_{pu} = (h_{i,2e} - h_{2d}) / (h_{2e} - h_{2d})$ ,  $h_{2h}$  can be obtained by  $\eta_{pu} = (h_{i,2h} - h_{2g}) / (h_{2h} - h_{2g})$ .  $h_{i,2e}$  is determined by  $s_{2d}$  and  $p_e$ ,  $h_{i,2h}$  is determined by  $s_{2g}$  and  $p_s$ .

The outlet water of the deaerator is saturated water ( $x = 0$ ), so the outlet temperature  $T_{2g}$  and outlet enthalpy  $h_{2g}$  of the heated fluid is determined by pressure  $p_{2g}$ . For the deaerator, the outlet pressure equals to any of the inlet pressure.

$$p_{2g} = p_{2c} \quad (3.63)$$

Heat injected in the water circuit

$$Q_2 = (1 - y) \dot{m}_2 (h_{2f} - h_{2e}) + \dot{m}_2 (h_{2a} - h_{2h}) \quad (3.64)$$

The efficiency of Rankine cycle can be expressed as

$$\eta_{rk} = (P_{tb} - P_{pu} / \eta_{ge}) / Q_2 \quad (3.65)$$

### 3.1.5.2 ORC cycle

Compared with steam Rankine cycle, ORC has the following features:

1. Organic fluid has lower boiling point, and higher evaporation pressure. It is suitable for the recovery of low temperature waste heat. Besides, it has small density and specific heat capacity, the required size of turbine, pipes and heat transfer areas are small, which is beneficial for cost saving.
2. The exhaust fluid of the turbine is dry. So without overheat, the saturated gas can be used as the main gas for the turbine. The corrosion situation caused by the impact of the droplets to the high-speed rotating blades will not happen with ORC.
3. Organic fluid has lower sound speed than vapor, the turbine can achieve favorable aerodynamic performance with lower wheel speed.
4. Organic fluid has higher condensing pressure than water. It can condense under the pressure higher than the atmosphere. The system pressure can be maintained above the atmosphere pressure to prevent air leak into the system. This means a deaerator is no more necessary.
5. Organic fluid has low freezing point, no anti-freezing treatment is required even in the cold area.

The shapes of curves in the  $T$ - $s$  diagram of different fluids are different. According to the saturated vapor curve  $dT/ds$  in the  $T$ - $s$  diagram, the working fluid can be divided into three types:  $dT/ds > 0$  means drying fluid (moisture does not form when high-pressure saturated vapor expanded reversibly from a high pressure), most of the organic fluid are drying fluids;  $dT/ds < 0$  means wetting fluid (moisture forms when high-pressure saturated vapor expanded reversibly from a high pressure), such as water;  $dT/ds \rightarrow \pm\infty$  means isentropic fluid, such as R134a. For the high temperature high pressure drying fluid and isentropic fluid, since there is no droplets after work in the expansion turbine, no superheater is required. On the other hand, since the purpose of the ORC focuses on the recovery of low grade heat power, a superheated approach like the traditional Rankine cycle is not appropriate.

Figure 3-8 shows the  $T$ - $s$  diagram of steam Rankine cycle and ORC cycle. Figure 3-9 shows the schematic diagram of the ORC system. For a drying fluid, the cycle can be improved by the use of a regenerator: since the fluid has not reached the two-phase state at the end of the expansion, its temperature at this point is higher than the condensing temperature.

This higher temperature fluid can be used to preheat the liquid before it enters the evaporator. A counter-current heat exchanger is thus installed between the expander outlet and the evaporator inlet. The power required from the heat source is therefore reduced and the efficiency is increased.

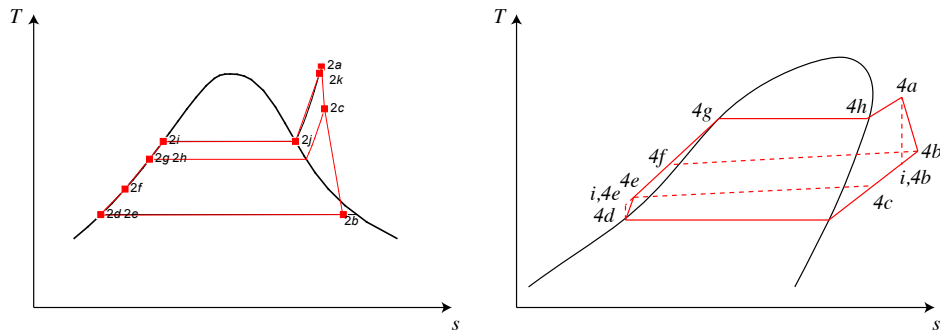


Figure 3-8  $T$ - $s$  diagram of water and a typical organic fluid

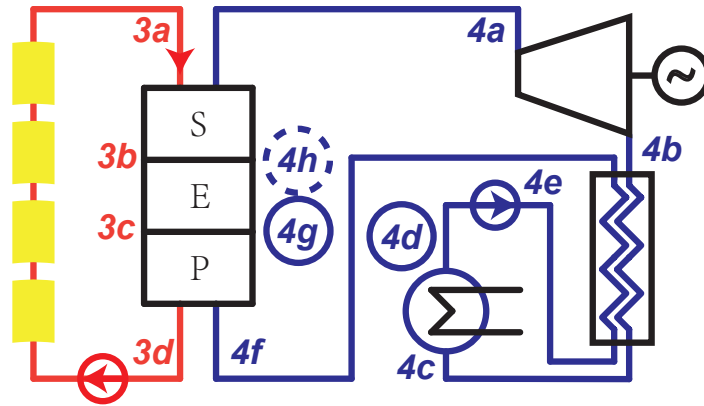


Figure 3-9 The schematic diagram of an ORC system with regenerator

The isentropic efficiency of the turbine

$$\eta_{i,tb} = (h_{4a} - h_{4b}) / (h_{4a} - h_{i,4b}) \quad (3.66)$$

where  $h_{i,4b}$  is determined by  $s_{4a}$  and  $p_c$ .

The output power of the turbine

$$P_{tb} = \dot{m}_4(h_{4a} - h_{4b}) \quad (3.67)$$

Process  $4c-4d$  shows the heat process in the condenser. The outlet fluid in the condenser is saturated liquid. The outlet temperature  $T_{4d}$  and outlet enthalpy  $h_{4d}$  are determined by the exhaust pressure of the turbine  $p_c$ .

For the regenerator,

$$h_{4b} - h_{4c} = h_{4f} - h_{4e} \quad (3.68)$$

The released heat of the condenser

$$Q_{cd} = \dot{m}_4(h_{4c} - h_{4d}) \quad (3.69)$$

The power of the pump

$$P_{pu} = \dot{m}_4(h_{4e} - h_{4d}) \quad (3.70)$$

where  $h_{4e}$  can be obtained by  $\eta_{pu} = (h_{i,4e} - h_{4d})/(h_{4e} - h_{4d})$ .  $h_{i,4e}$  is determined by  $s_{4d}$  and  $p_s$ .

Heat injected in the circuit

$$Q_4 = \dot{m}_4(h_{4a} - h_{4f}) \quad (3.71)$$

The efficiency of Rankine cycle can be expressed as

$$\eta_{rk} = (P_{tb} - P_{pu}/\eta_{ge})/Q_4 \quad (3.72)$$

### 3.1.5.3 Generator

The generator is relatively independent of the cascade system and its efficiency is assumed to be a constant, 0.975.

## 3.2 Stirling engine array

Stirling engine array is used in the cascade system, fig. 3-10 shows the layout of the Stirling engine array. Each Stirling engine in the Stirling engine array has the identical parameters:  $U_{se,1} = 30 \text{ W}/(\text{m}^2 \cdot \text{K})$ ,  $U_{se,2} = 150 \text{ W}/(\text{m}^2 \cdot \text{K})$ ,  $A_{se,1} = 6 \text{ m}^2$ ,  $A_{se,2} = 6 \text{ m}^2$ ,  $k_{se} = 1.4$ ,  $\gamma_{se} = 3.375$ ,  $n_g = 7.84 \times 10^{-2} \text{ mol}$ ,  $s_{se} = 10 \text{ s}^{-1}$ .

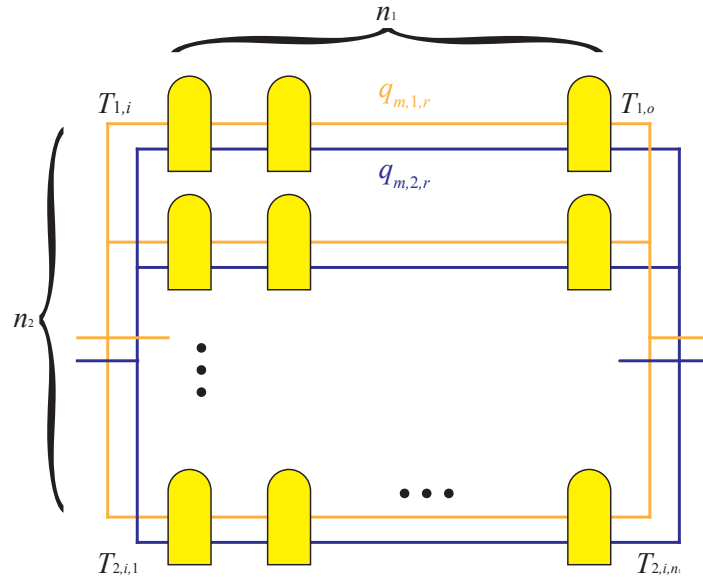


Figure 3-10 Layout of Stirling engines

Depending on the direction of heating and cooling flows, there are two possible flow types: parallel flow and counterflow. Figure 3-11 and Figure 3-12 show the heat transfer diagrams of the two flow types.  $n_1$  is chosen to be 10 and can be optimized later.

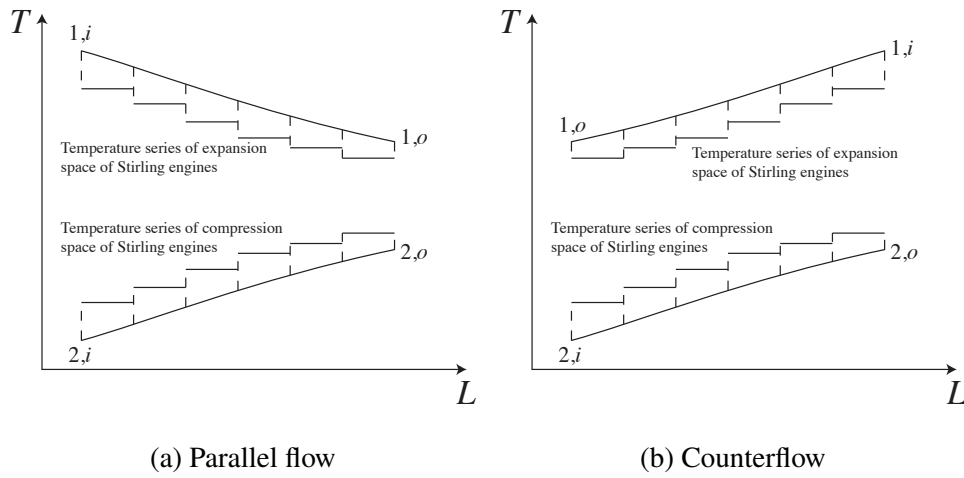


Figure 3-11 Heat transfer diagram of parallel flow and counterflow

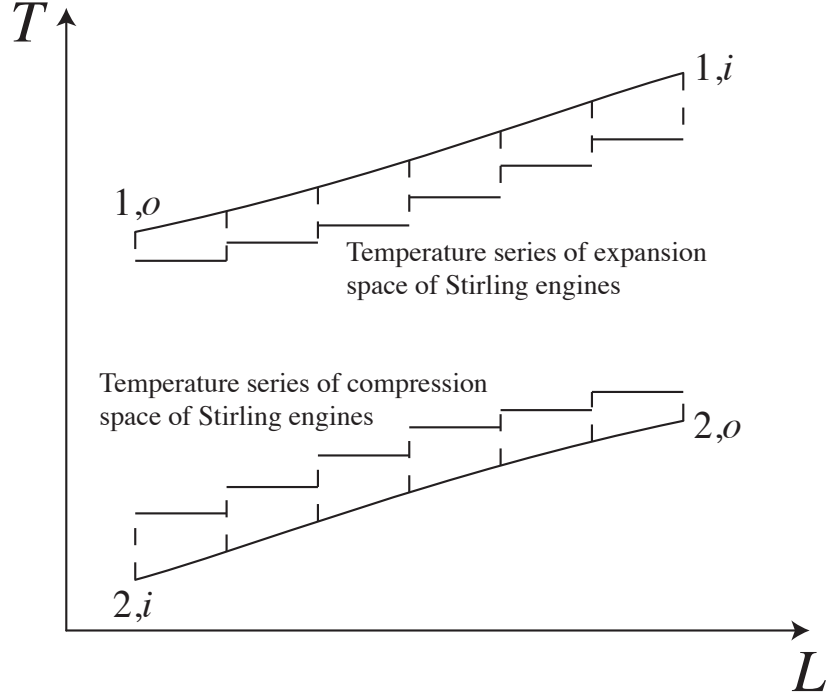


Figure 3-12 Heat transfer diagram of counterflow

In Figure 3-10,  $T_{1,i,1} = T_{1,i}$ ,  $\dot{m}_{1,r} = \dot{m}_1/n_2$ . For  $x$  from 1 to  $n_1 - 1$ , where  $x$  is the column number of Stirling engines,  $T_{1,i,x+1} = T_{1,o,x}$ ,  $T_{2,i,x+1} = T_{2,o,x}$ .

Assume that the positive flow direction is to the right, for parallel flow,  $T_{2,i,1} = T_{2,i}$ ,  $\dot{m}_{2,r} = \dot{m}_2/n_2$ ; for counterflow,  $T_{2,o,n_1} = T_{2,i}$ ,  $\dot{m}_{2,r} = -\dot{m}_2/n_2$ .

Assume linear temperature profile across the regenerator, the mean effective temperature  $T_{R,x} = \frac{T_{H,x} - T_{L,x}}{\ln(T_{H,x}/T_{L,x})}$  [88,89], and the symmetrical regenerator behaviour assumption  $e_x = \frac{T_{R,x} - T_{L,x}}{T_{H,x} - T_{L,x}}$  [80,81]. For a Stirling engine in column  $x$ ,  $x$  from 1 to  $n_1$ , according to Equation 3.33 and Equation 3.34,

$$T_{hw,x} = T_{1,i,x} - \frac{T_{1,i,x} - T_{1,o,x}}{1 - \exp\left(-\frac{U_{se,1}A_{se,1}}{\dot{m}_{1,r}c_{p,1,x}}\right)} \quad (3.73)$$

$$T_{cw,x} = T_{2,i,x} - \frac{T_{2,i,x} - T_{2,o,x}}{1 - \exp\left(-\frac{U_{se,2}A_{se,2}}{\dot{m}_{2,r}c_{p,2,x}}\right)} \quad (3.74)$$

The power of each Stirling engine in column  $x$  can be written as

$$P_{se,x} = W_{th,x} - W_{pd,x} - W_{fs,x} \quad (3.75)$$

The efficiency of each Stirling engine in column  $x$  can be written as

$$\eta_{se,x} = \frac{W_{th,x} - W_{pd,x} - W_{fs,x}}{Q_{th,x} + Q_{id,x} + Q_{sc,x}} \quad (3.76)$$

For energy balance,

$$\dot{m}_{1,r}(h_{1,i,x} - h_{1,o,x})(1 - \eta_{se,x}) = \dot{m}_{2,r}(h_{2,o,x} - h_{2,i,x}) \quad (3.77)$$

By using equations in 3.1.3 and the energy balance equations, key parameters of the Stirling engine array can be obtained.

The efficiency of the Stirling engine array

$$\eta_{sea} = 1 - \frac{\dot{m}_2(h_{2,o,n_1} - h_{2,i,1})}{\dot{m}_1(h_{1,i,1} - h_{1,o,n_1})} \quad (3.78)$$

The output power of each Stirling engine in column  $x$

$$P_{se,x} = \dot{m}_{1,r}(h_{1,i,x} - h_{1,o,x})\eta_{se,x} \quad (3.79)$$

The output power of the Stirling engine array

$$P_{sea} = \eta_{sea}\dot{m}_1(h_{1,i,1} - h_{1,o,n_1}) \quad (3.80)$$

### 3.3 Component connection



## Chapter 4 Optimization of Stirling engine array

### 4.1 Connection types of SEA

For a single Stirling engine, the heat transfer processes between fluids and engine are independent and irrelevant with the direction of the flows, which means the efficiency and power are not affected by the direction of fluids. However, for an SEA, the connection type will affect the temperature profiles through the array and the specific work production, both of which will determine the efficiency and power of the SEA. It is practically significant to investigate the influence of connection type of an SEA on its performance. Using parallel flow, on the one hand, will reduce the flow rate of the fluid, which will reduce the power of each engine; however, on the other hand, will take the advantage of higher inlet heating fluid temperature (or lower inlet cooling fluid temperature), which may increase the power of each engine. Using serial flow, on the one hand, will increase the flow rate of the fluid, which will increase the power of each engine; however, on the other hand, the inlet heating fluid temperature reduces with the flow direction (or the inlet cooling fluid temperature increases with the flow direction), which leads to lower engine power along the flow direction. Using the same order will lead to largest fluid temperature difference (temperature difference of the heating and cooling fluids) at the first engines and smallest fluid temperature difference at the last engines. Using the reverse order will lead to more averaged fluid temperature differences of the engines. For a heat exchanger, the reverse order (counterflow), which leads to a smaller fluid temperature difference, has a better heat transfer effect for its lower exergy loss. However, for a Stirling engine, the smaller fluid temperature difference leads to lower performance due to the lower temperature difference of the working gas in the hot space and cold space. To find out the influence of connection types on the performance of SEA, it is essential to classify the connection types.

Five basic connection types of SEA were summarized according to the direction-irrelevant feature of Stirling engine, as shown in Figure 4-1. Type 1 is parallel flow, Type 2 is serial flows in the same order, Type 3 is serial flows in the reverse order, Type 4 is heating fluid in serial flow and cooling fluid in parallel flow and Type 5 is heating fluid in parallel flow and cooling fluid in serial flow. All other connection types are the combination of these five

basic connection types. For instance, an SEA in Figure 4-2 is the combination of Type 2 and Type 4.

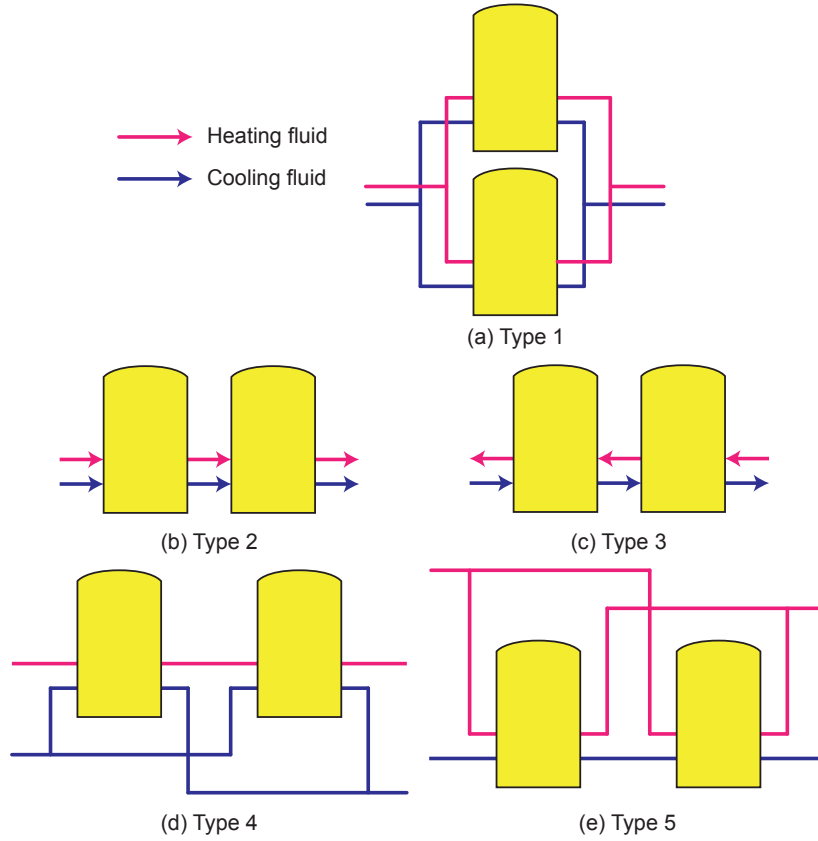


Figure 4-1 Five basic connection types of SEA

## 4.2 Modeling of the SEAs

As mentioned in section 4.1, there are five basic connection types for an SEA. All other connection types are the combination of these five basic connection types. This paper investigates the five basic connection types.

To determine the performance of an SEA, models of all the Stirling engines need to be built depending on their thermodynamic characteristic. Stirling engines are chosen to

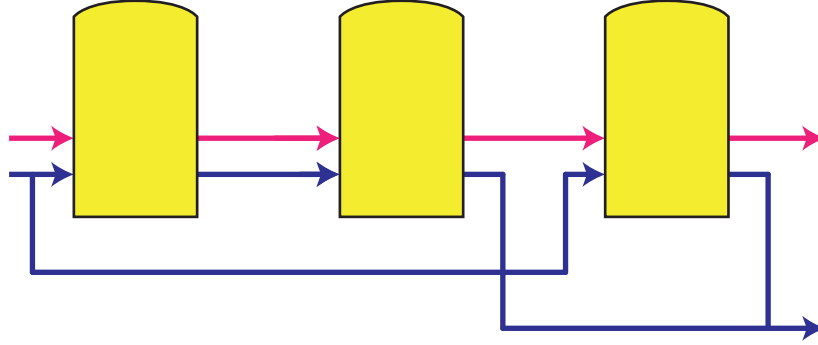


Figure 4-2 An instance of connection type of an SEA

have the same parameters including the same speed  $s_{se}$ . This is a reasonable assumption when using SEA for power generation, where the output power frequency should be constant. The speed of Stirling engine can be calibrated by speed controller system<sup>[90]</sup>. To eliminate interference of other factors, heating and cooling fluids are chosen to have same parameters for different connection types of SEAs. To clearly find out the performance differences of different SEAs, large temperature differences of the heating/cooling fluids after heat exchange with the engines are preferred. Air was chosen as the cooling fluid instead of commonly used water to avoid small temperature rise and evaporation in the cooling process. Design parameters of Stirling engines are the same as shown in Table 3.2. Other parameters of Stirling engines and heating/cooling fluids in SEAs are shown in Table 4.1. Rotation speed of the engines and mean effective pressure were chosen to be 25 Hz and 5 MPa respectively to get the best Stirling engine model for performance prediction, as pointed in section ??.

In an SEA, there are 2 flows as shown in Figure 4-1. In a serial flow, each engine's mass flow rate is  $q_m$ , and from the flow's direction, for  $2 \leq x \leq n_{se}$ ,  $T_{i,x} = T_{o,x-1}$ . In a parallel flow, each engine's mass flow is  $q_m/n_{se}$ , for  $2 \leq x \leq n_{se}$ ,  $T_{i,x} = T_{i,h}$ .

MATLAB was used as the programming tool to build the model of SEAs, and Cool-Prop was used to provide fluid properties for MATLAB program. Five basic SEA models composed of the aforementioned Stirling engines and fluids were built. To compare SEA connection types under various conditions, several parameters are investigated to find out their effects on SEA performance.

Table 4.1 Parameters of SEA models

Parameter	Value	Parameter	Value
Heating fluid	Air	$q_{m,h}$	0.4 kg/s
Cooling fluid	Air	$T_{i,h}$	1000 K
$n_{se}$	6	$p_{i,h}$	$5 \times 10^5$ Pa
$s_{se}$	25 Hz	$q_{m,c}$	0.4 kg/s
$p_{se}$	5 MPa	$T_{i,c}$	300 K
$U_h A_h$	180 W/K	$p_{i,c}$	$5 \times 10^5$ Pa
$U_c A_c$	180 W/K		

### 4.3 Result Analysis

SEA models with specified parameters in Table 4.1 were built and calculated. Results of the performances of the SEAs are shown in Table 4.2, it can be found that under specified parameters Type 3 has the highest efficiency and output power, while Type 1 has the lowest efficiency and output power.

Table 4.2 Results of SEA models under specified parameters

Parameter	Value	Parameter	Value
$\eta_1$	0.2215	$P_1$	8022 W
$\eta_2$	0.2273	$P_2$	8483 W
$\eta_3$	0.2277	$P_3$	8512 W
$\eta_4$	0.2227	$P_4$	8116 W
$\eta_5$	0.2263	$P_5$	8399 W

#### 4.3.1 Effects of $T_{i,h}$

According to Carnot cycle efficiency formula, the temperature of heating fluid determines the efficiency of Stirling engine array. For a Stirling engine, lower temperature heating fluid leads to a lower efficiency. The efficiency and output power may drop to 0 due to its insufficient heating fluid temperature to drive the engine.

Curves of performance of SEAs and  $T_{i,h}$  are shown in Figure 4-3. As it is shown, with the increase of  $T_{i,h}$ , both  $\eta$  and  $P$  increase for all SEAs. For some types of SEA, when  $T_{i,h}$  is lower than a critical temperature, some of the engines in the SEA will not work and there will be turning points on the  $\eta - T_{i,h}$ ,  $P - T_{i,h}$  curves. For example, in SEA of Type 1, when  $T_{i,h}$  is lower 820 K, all the engines stop working, turning points at 820 K can be found on the  $\eta - T_{i,h}$ ,  $P - T_{i,h}$  curves in Figure 4-3.

From curves in Figure 4-3, it can be concluded that Type 2 and Type 3 have the best performance, and Type 2 has the best adaptability for lower  $T_{i,h}$ . All engines in Type 2 work at 730 K.

#### 4.3.2 Effects of $q_m c_p$

According to Equation 3.53, 3.54,  $q_m c_p$  (both  $q_{m,h} c_{p,h}$  and  $q_{m,c} c_{p,c}$ ) will affect the heat transfer process, which is one of the vital factor for the performance of SEA.

Curves of performance of SEAs and  $q_{m,h} c_{p,h}$  are shown in Figure 4-4. For a large  $q_{m,h} c_{p,h}$  ( $> 800$  W/K), Type 2, Type 3 and Type 5 have similar performance, which can be interpreted as the cooling fluid has the same properties for the two types of SEAs, and for a large  $q_{m,h} c_{p,h}$ , the heating fluid has similar effect after diverged. Similar performance of Type 1 and Type 4 can be also interpreted for the same reason.

Curves of performance of SEAs and  $q_{m,c} c_{p,c}$  are shown in Figure 4-5. For a connection type of SEA, the performance improves with the increase of  $q_{m,c} c_{p,c}$ . For a large  $q_{m,c} c_{p,c}$  ( $> 800$  W/K), Type 2 and Type 3 have similar performance, which means the flow order doesn't affect the performance of SEA with a large  $q_{m,c} c_{p,c}$ . There exists an intersection point (at 830 W/K) of curves of Type 4 and Type 5. For a larger  $q_{m,c} c_{p,c}$ , Type 4 has a better performance, and vice versa. This can be interpreted that larger  $q_{m,c} c_{p,c}$  weaken the drawback of larger

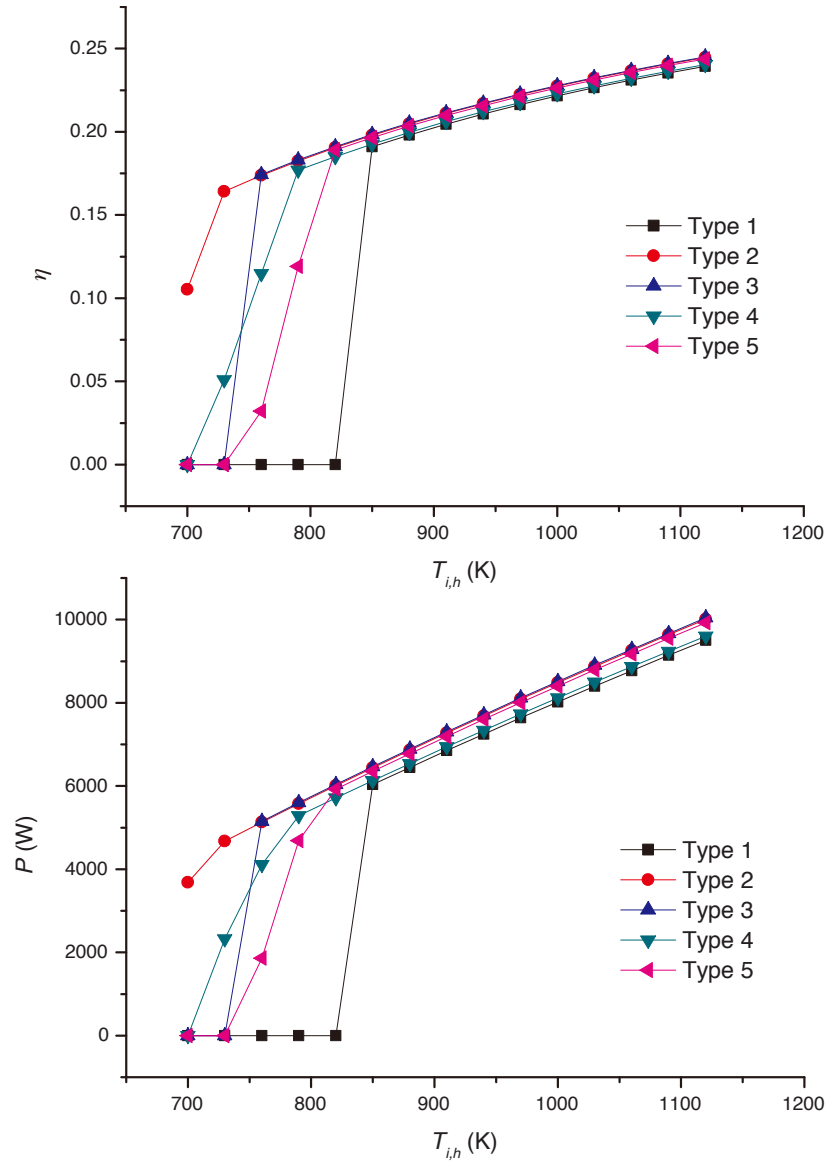


Figure 4-3 Influence of  $T_{i,h}$  on efficiency and power of SEA

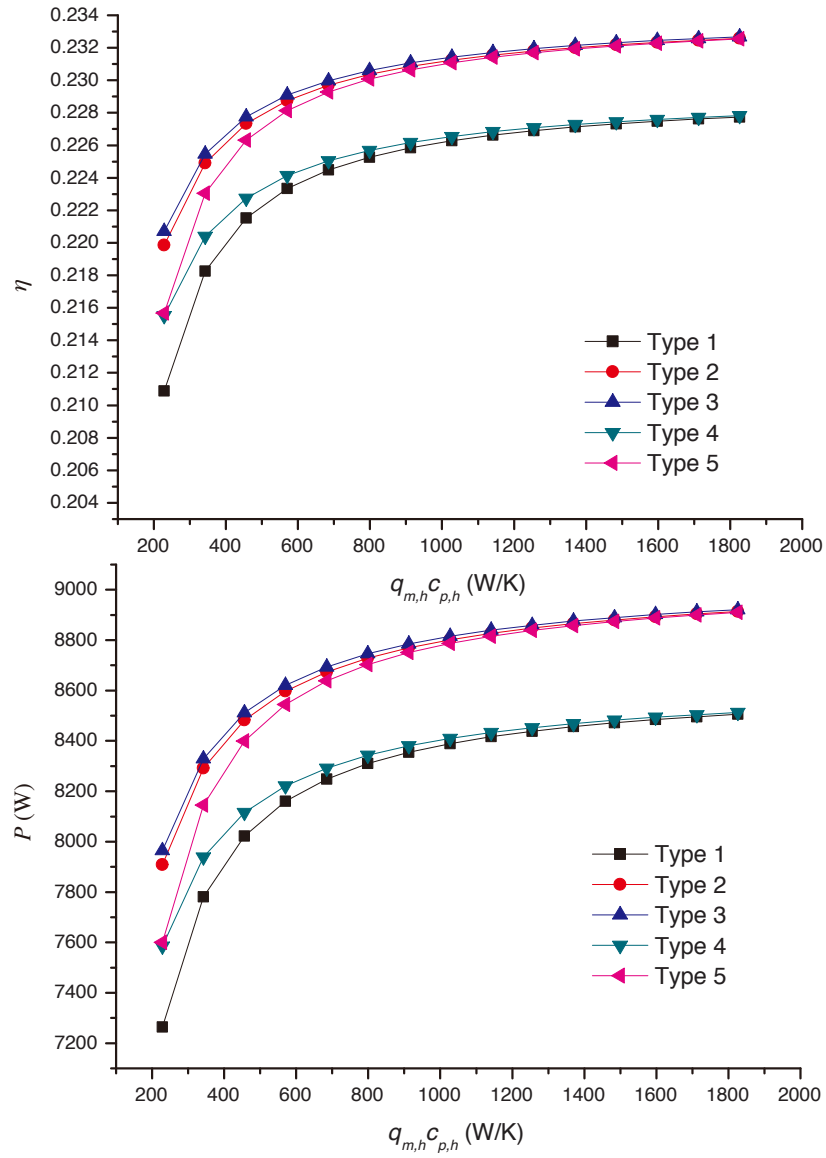


Figure 4-4 Influence of  $q_{m,h}c_{p,h}$  on efficiency and power of SEA

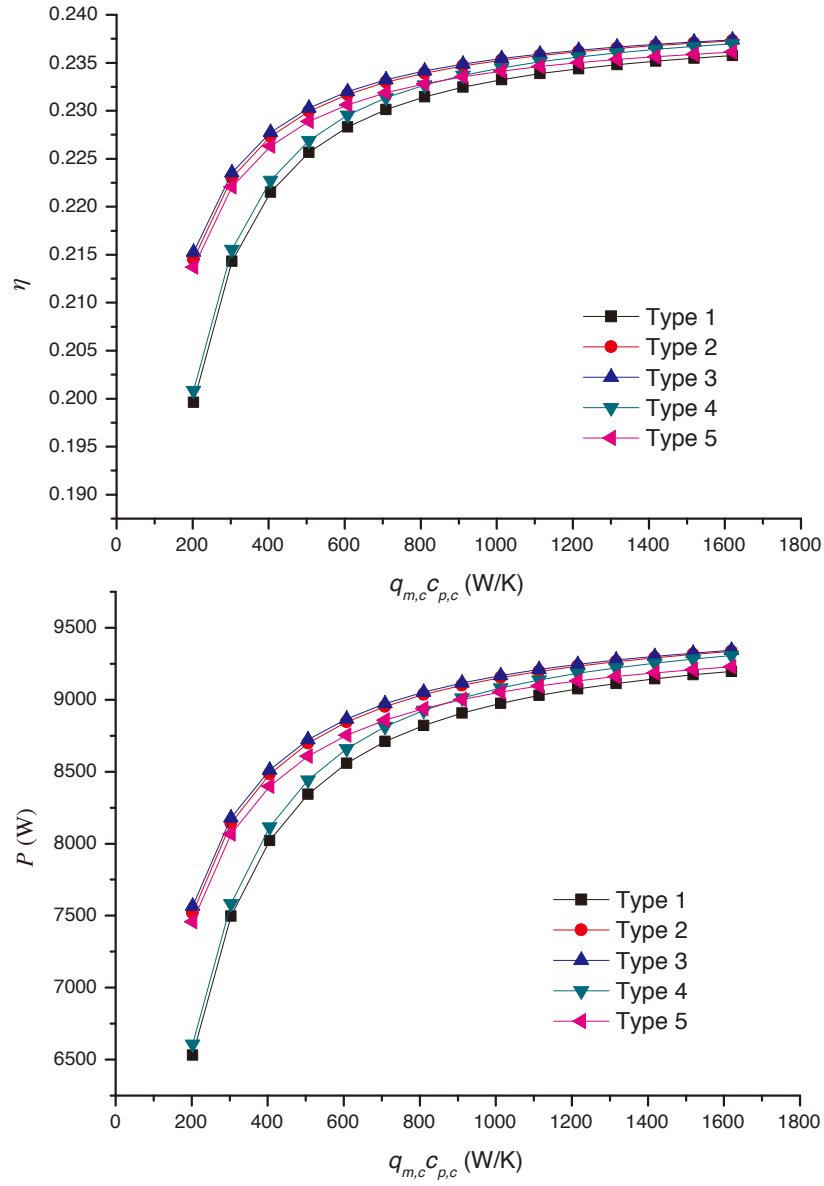


Figure 4-5 Influence of  $q_{m,c}c_{p,c}$  on efficiency and power of SEA



temperature rise of parallel flow, while for the heating fluid, temperature drop of serial flow is smaller than parallel flow.

### 4.3.3 Effects of $n_{se}$

By varying the number of engines in SEA, the performance levels changed accordingly.  $n_{se}$  may affect both the flow rates and temperatures of fluids of each engine. Figure 4-6 shows curves of performance of SEAs with different  $n_{se}$ . As it is shown, with an increase of  $n_{se}$  leads to a reduction of  $\eta$  for all SEAs due to smaller heating and cooling average temperature difference for more engines. For some types of SEA, when  $n_{se}$  is larger than a critical value, some of the engines in the SEA will not work and the curves will dive. E.g. for SEA of Type 1, when  $n_{se}$  is larger than 9, all the engines stop working, turning points at 9 can be found on the  $\eta - n_{se}$ ,  $P - n_{se}$  curves in Figure 4-6.

For Type 1, when  $n_{se} \geq 10$ , all engines stop working for given heating and cooling fluids due to small  $q_m c_p$ . For Type 2 and Type 3, every engine in the SEAs works, by increasing  $n_{se}$ ,  $\eta$  reduces due to smaller temperature difference of the fluids, and  $P$  increases due to more operating engines. For Type 4, by checking results, it can be found that when  $n_{se} = 13$ , the last engine doesn't work; when  $n_{se} = 14$ , only the first 10 engines will work; when  $n_{se} = 15$ , the working engine number drops to 9. For Type 5, by checking results, it can be found that when  $n_{se} = 12$ , the last 2 engines stop working; when  $n_{se} = 13$ , only the first 8 engines will work; when  $n_{se} = 14$ , the working engine number drops to 6; when  $n_{se} = 15$ , the working engine number drops to 4.

For a certain connection type, increase  $n_{se}$  will reduce the efficiency of SEA. For some connection types, increase  $n_{se}$  will reduce the output power  $P$  due to inoperative engines and smaller output power engines. It is important to choose the number of engines for some connection types of SEA.

## 4.4 Conclusion

A new layout scheme of the solar dish system by using SEA were proposed in this paper. Connection type of the engines may change the flow rates and temperatures of the fluids, as a result the performance of the SEA will be different depending on the connection schemes.

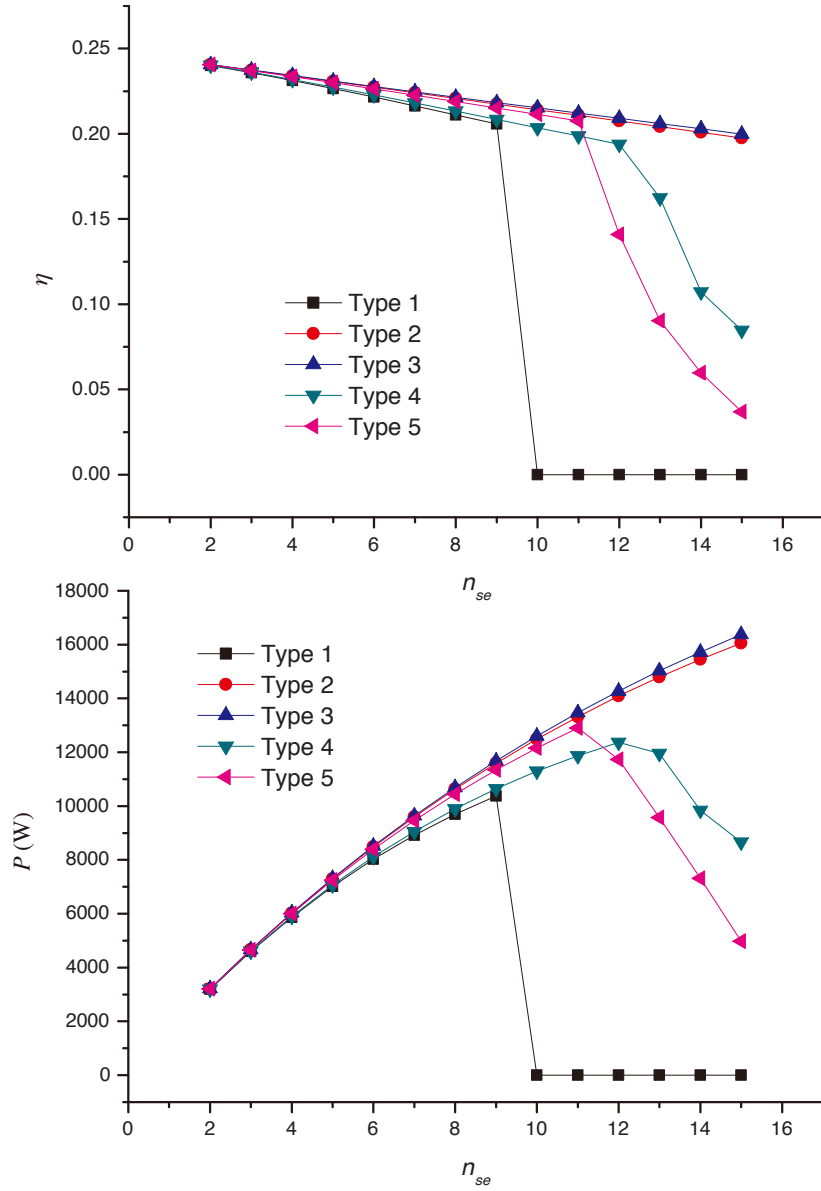


Figure 4-6 Influence of  $n_{se}$  on efficiency and power of SEA

In order to compare performance of SEAs with different arrangements, five basic connection types of SEA were summed up according to flow type and flow order.

Analytical Stirling engine model was created to develop the SEA models for the investigation of influence of connection types. Imperfect regeneration and cycle irreversibility of Stirling engine cycle and heat exchange process between fluids and engine were considered in the model. Algorithm to numerically solve different connection types of SEA was developed. The model was evaluated by considering the prototype GPU-3 Stirling engine as a case study. Result shows that the proposed model predicted the performance with higher accuracy than Simple model<sup>[83]</sup> and Simple II model<sup>[85]</sup>.

Models of SEAs were developed to calculate the performance under different parameters to find out the impacts of  $T_{i,h}$ ,  $q_{m,h}c_{p,h}$ ,  $q_{m,c}c_{p,c}$  and  $n_{se}$  on different connection types. It was found that, as expected, decrease  $T_{i,h}$  and  $q_{m}c_p$  will weaken the performance of SEA of all connection types. However, for some connection types, there exists a critical temperature below which some engines stop working. This needs to be considered for SEA connection type selection, especially when  $T_{i,h}$  is low. For given heating and cooling fluids, Type 2 has the best performance and adaptability. Type 2 and Type 3 have similar performance under different parameters ( $T_{i,h}$ ,  $T_{i,c}$  and  $q_{m}c_p$ ), which means the flow order has little influence on the performance of an SEA. SEA of serial flows (Type 3) has the best performance and adaptability under different parameters. Given heating and cooling fluids, using serial flow is the best choice for the connection type of an SEA.

It is important to note that, in the future researches, the experiments of influence of connection type on SEA's performance can be carried out to verify the conclusions in this paper.

## Chapter 5 Optimization of steam generating system

### 5.1 Steam generator subsystem

In a solar parabolic trough power plant in which intermediate heat-transfer fluid (take oil for instance) is used, heat addition to the working fluid (take water for instance) takes place in three counterflow heat exchangers (steam generator subsystem, SGSS) as shown in fig. 5-1. The SGSS is consist of preheater, evaporator, superheater. The flow rates of both oil and water remains the same in the three heat exchangers. The water has phase change in the three heat exchangers, from liquid to vapor in the evaporator, however, oil remains liquid. The heat capacity of water in each heat exchanger differs a lot. The heat capacity of oil has no significant difference since no phase change. The heat transfer process is illustrated on fig. 5-2. Large temperature differences exist at the inlets and outlets of the heat exchangers, which makes large entropy production during the entire heat transfer process.

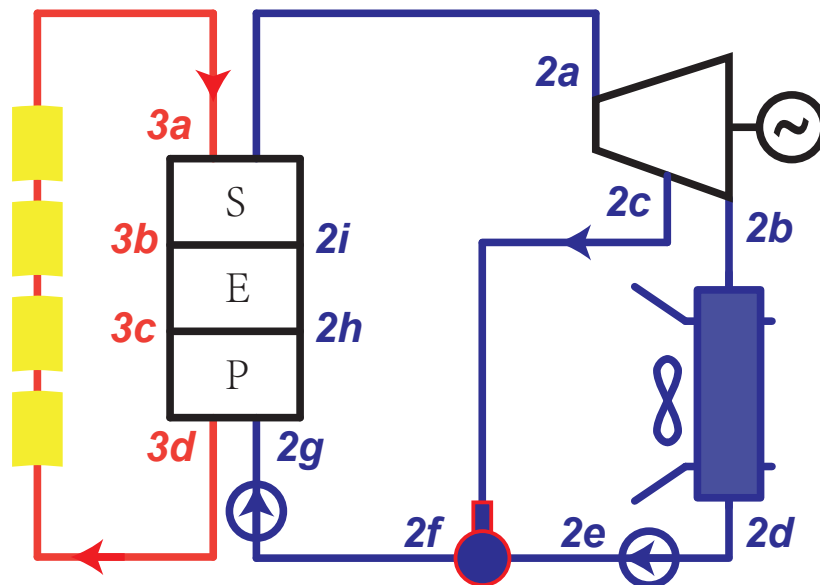


Figure 5-1 An typical solar parabolic trough system

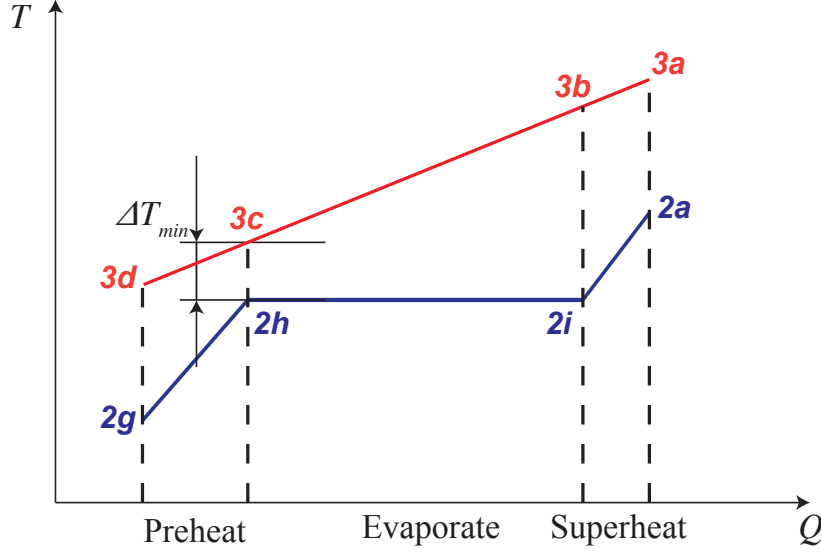


Figure 5-2 The steam generating process in countertlow heat exchangers

The heat-transfer fluid at  $3a$  represents the solar field outlet temperature and at  $3d$ , the field return temperature. The difference between these can be reduced by increasing the flow rate of heat-transfer fluid through the field and thus the parasitic pumping power.

Since the heat exchangers must always stay a positive temperature difference for heat transfer, the temperature of oil must always be higher than the temperature of water. On the other hand, the temperature of oil should not be much higher than that of the water. Higher oil temperature leads more heat losses in the solar field hence lower efficiency, more entropy production generated in the heat exchange process. Besides, higher oil temperature brings greater operational risks for the solar system. Setting the appropriate temperature difference between the oil and water is particularly important. The oil temperature must always higher (but not too much higher) than that of the water.

To find out the inlet and outlet temperatures of oil at the solar field, the lowest temperature difference of oil and water is defined as the pinch temperature  $\Delta T_{min}$ . The temperatures of state points  $2h$  and  $2i$  are determined by the main pressure of the steam turbine in fig. 5-1, and  $T_{3b}$  is larger than  $T_{3c}$ . So state points  $3c$  and  $2h$ , called the pinch point, are set to satisfy the pinch temperature,  $T_{3c} - T_{2h} = \Delta T_{min}$ . The pinch temperature  $\Delta T_{min}$  is usually set to be  $10 \sim 20$  K. It has to be mentioned that the temperature differences  $T_{3d} - T_{2g}$  and  $T_{3a} - T_{2j}$  worth attention to be not larger than  $\Delta T_{min}$ .

However, even with the chosen pinch temperature  $\Delta T_{min}$ , the temperature difference during the heat exchange process in SGSS is still large due to the phase change of water. Large temperature differences always exists at the inlet/outlet of the exchangers. As shown in fig. 5-3, it is a tradeoff to choose a mass flow rate of oil ( $\dot{m}_3$ ).  $\dot{m}_3$  affects the slope of curve 3a-3b-3c-3d. A smaller  $\dot{m}_3$  leads to a steeper curve, hence a larger  $T_{3a} - T_{2j}$ . A larger  $\dot{m}_3$  leads to a more gentle curve, hence a larger  $T_{3d} - T_{2g}$ . The heat transfer processes in SGSS always produce large entropy and exergy destruction. In this regard, a new steam generating system to reduce exergy destruction is put forward.

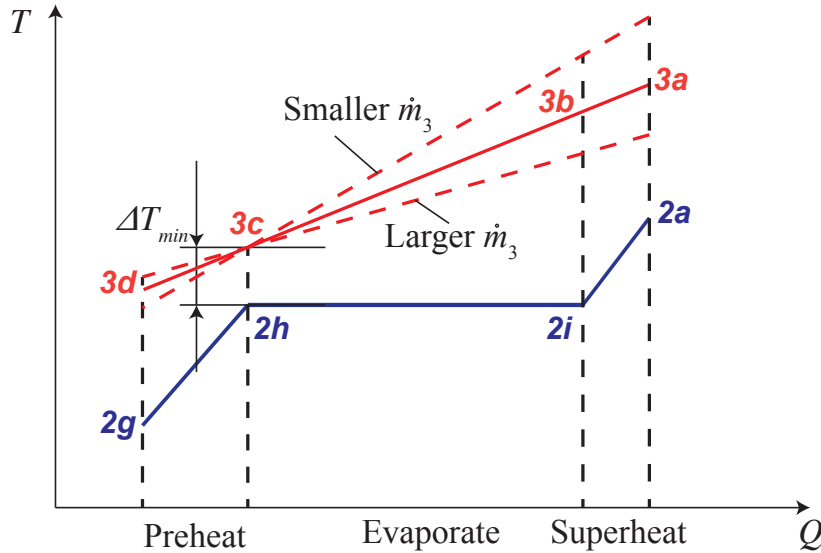


Figure 5-3 The tradeoff to choose  $\dot{m}_3$

## 5.2 Multi-stage exergy loss reduction system

The reason of large temperature differences of the two curves in fig 5-2 is that, the slope of oil curve changes slightly in different heat exchangers (preheater, evaporator and superheater), while the water curve changes dramatically due to large heat capacity  $c_p$  differences.

$$\Delta Q = c_p \dot{m} \Delta T \quad (5.1)$$

The slope of the curves are determined by  $c_p \dot{m}$ ,  $\dot{m}$  can be altered to adjust the slope of

the curves despite the  $c_p$  is unalterable. All the water needs to be heated from supercooled water to superheated steam, which means  $\dot{m}_2$  remains the same in the three heat exchangers. The last way is to change  $\dot{m}_3$  in the heat exchangers.

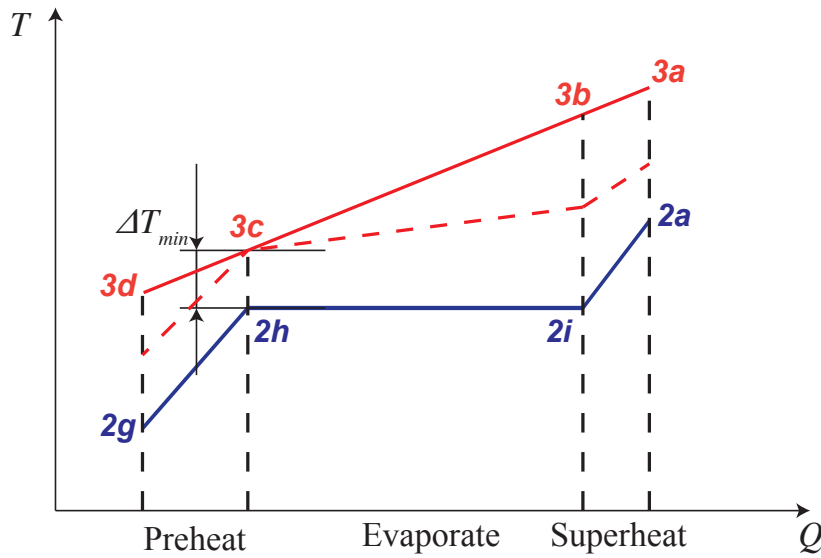


Figure 5-4 Change  $\dot{m}_3$  in the heat exchangers to reduce the temperature difference

As shown in fig. 5-4, the oil curve can be changed to the dashed curve. The temperature difference between the water curve and oil curve reduces significantly. Water is heated in three stages and the exergy loss reduces. The corresponding steam generating system is so called Multi-stage exergy loss reduction system (MERS). Fig. 5-5 shows the schematic diagram of the MERS for comparison of typical solar parabolic trough system in fig. 5-1. The solar field in fig. 5-1 has been divided into three independent sectors. Each sector becomes the heat source of a range for the steam heating process: the first corresponds to overheating, the second to evaporation, and the third to preheating. It has to be mentioned that the collectors in the schematic diagram are only used for explanation. The arrangement of these collectors can be in series, in parallel or combination of both.

To optimize the MERS, considering the limitation of pinch temperature, temperatures of the oil at the inlet/outlet of the heat exchangers can be set according to following rules:

1.  $T_{3d} - T_{2g} = \Delta T_{min}$

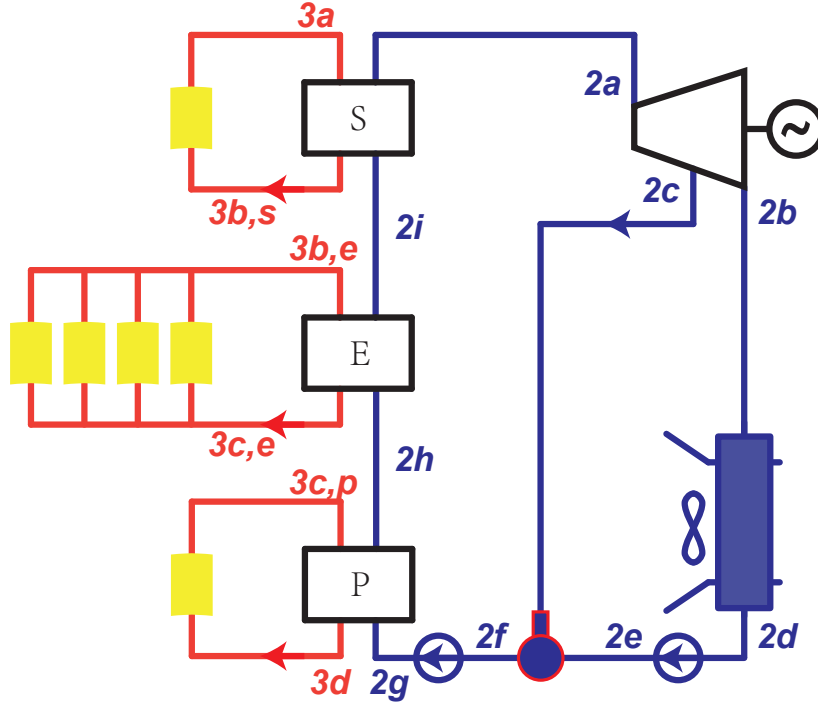


Figure 5-5 The schematic diagram of the MERS

2.  $T_{3c,p} = T_{3c,e} = T_{3c}$
3.  $T_{3c} - T_{2h} = \Delta T_{min}$
4.  $T_{3b,e} = T_{3b,s} = T_{3b}$
5.  $T_{3a} - T_{2a} = \Delta T_{min}$

A large flow rate of oil in the evaporator  $\dot{m}_{3,e}$  can be applied to decrease the temperature  $T_{3b}$  hence the temperature differences of the oil and water. However, a large  $\dot{m}_{3,e}$  requires more oil usage and more pump power for the oil circuits. Besides,  $\dot{m}_{3,e}$  is limited for the limitation of oil velocity in the pipes.

The enthalpy of each state point can be determined by its temperature and pressure.

The optimum oil average temperature in the solar field corresponds to the preheater is

$$T_{3,p} = (T_{2g} + T_{2h})/2 + \Delta T_{min} \quad (5.2)$$

The optimum oil flow rate in the solar field corresponds to the preheater is

$$\dot{m}_{3,p} = \dot{m}_2(h_{2h} - h_{2g})/(h_{3c} - h_{3d}) \quad (5.3)$$



The optimum oil average temperature in the solar field corresponds to the evaporator is

$$T_{3,e} = (T_{3b} + T_{3c})/2 \quad (5.4)$$

The optimum oil flow rate in the solar field corresponds to the evaporator is

$$\dot{m}_{3,e} = \dot{m}_2(h_{2i} - h_{2h})/(h_{3b} - h_{3c}) \quad (5.5)$$

The optimum oil average temperature in the solar field corresponds to the superheater is

$$T_{3,s} = (T_{3b} + T_{2a} + \Delta T_{min})/2 \quad (5.6)$$

The optimum oil flow rate in the solar field corresponds to the superheater is

$$\dot{m}_{3,s} = \dot{m}_2(h_{2a} - h_{2i})/(h_{3a} - h_{3b}) \quad (5.7)$$

### 5.3 Comparison

To find out the effect of MERS, models of traditional SGSS and proposed MERS are developed based on the models of the components. To clear find out the influence of oil temperature on the performance of the trough collectors, the equation summarized by<sup>[91]</sup> is used.

$$\eta(T) = 0.69563 + 0.000313T - 0.0000013T^2 \quad (5.8)$$

where  $T$  is the average temperature of the tube. Since the  $Nu$  number in the tube is large (about  $1 \times 10^4$ ), small temperature difference exists between the absorber and oil. So the average oil temperature can be used as the average value of the tube.

The exergy destruction caused by a heat exchange process per unit time

$$\dot{I} = T_a mb(\sum \dot{m}_o s_o - \sum \dot{m}_i s_i) \quad (5.9)$$

The turbine and deaerator are the same for the two systems (SGSS and MERS), so that the corresponding state points of water are the same. The main parameters are listed in Table 5.1.

As discussed in section 5.2,  $T_{3b}$  is an undetermined value. Fig. 5-6 shows the minimum and maximum value of it.  $T_{3b,min}$  means the limit situation of unlimited flow rate of oil in the evaporator,  $T_{3b,min} = T_{3c}$ . (see equation. 5.5)  $T_{max}$  has the traditional effect of temperature

Table 5.1 Main parameters used for both SGSS and MERS

Parameter	Value	Parameter	Value
$I_r$	$700 \text{ W/m}^2$	$T_s$	$613.15 \text{ K}$
$P_{ge}$	$6 \times 10^6 \text{ W}$	$p_s$	$2.35 \times 10^6 \text{ Pa}$
$\eta_{i,tb}$	$0.711$	$p_c$	$1.5 \times 10^4 \text{ Pa}$
$\eta_{ge}$	$0.975$	$p_{de}$	$1 \times 10^6 \text{ Pa}$
$\Delta T_{min}$	$15 \text{ K}$		

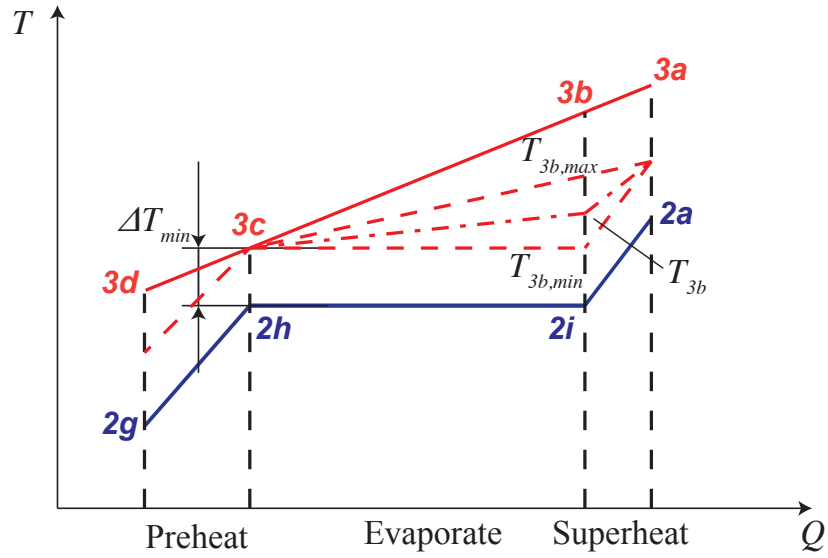


Figure 5-6  $T_{3b}$  in the  $T$ - $Q$  diagram of the heat transfer processes

differences in the evaporator and superheater,  $\dot{m}_{3,e} = \dot{m}_{3,s}$ . In our research,  $T_{3b}$  is set to be the average value of the two limitations,  $T_{3b} = (T_{3b,min} + T_{3n,max})/2$ .

$$\frac{T_{b,max} - T_{3c}}{T_{3a} - T_{3c}} = \frac{T'_{3b} - T_{3c}}{T'_{3a} - T_{3c}} \quad (5.10)$$

where  $T'_{3a}$  and  $T'_{3b}$  are the inlet oil temperature of superheater and evaporator in SGSS respectively. Simulation results of the two system models are listed in table 5.2. It can be

Table 5.2 Main parameters used for both SGSS and MERS

	SGSS	MERS
$T_{2a}$	613.15 K	613.15 K
$T_{2i}$	493.83 K	493.83 K
$T_{2h}$	493.83 K	493.83 K
$T_{2g}$	453.28 K	453.28 K
$T_{3a}$	653.15 K	628.15 K
$T_{3b}$	634.11 K	560.62 K
$T_{3c}$	508.83 K	508.83 K
$T_{3d}$	495.43 K	468.28 K
$\dot{m}_{3p}$	47.8 kg	16.1 kg
$\dot{m}_{3e}$	47.8 kg	120.8 kg
$\dot{m}_{3s}$	47.8 kg	14.3 kg
$\dot{I}_p$	$4.79 \times 10^4$ W	$2.39 \times 10^4$ W
$\dot{I}_e$	$1.10 \times 10^6$ W	$6.26 \times 10^5$ W
$\dot{I}_s$	$1.80 \times 10^5$ W	$9.19 \times 10^4$ W
$\dot{I}_{total}$	$1.33 \times 10^6$ W	$7.42 \times 10^5$ W
$\eta_p$	0.525	0.538
$\eta_e$	0.450	0.491
$\eta_s$	0.359	0.422
$\eta_{total}$	0.440	0.484

found that the MERS can effectively reduce exergy destruction hence improve the system efficiency compared to traditional SGSS.

## Chapter 6 Cascade system performance evaluation

### 6.1 System description

In the cascade system, dish collectors are used to provide heat for Stirling engines and air-to-water heat exchanger. Trough collectors are used to provide heat for steam generating processes (preheating, evaporating and superheating) in the Rankine cycle. Figure 6-1 shows the scheme sketch of the cascade system. In this system, hot air is produced by the dish collectors. High temperature (1073 K) air is used to provide heat to Stirling cycle to get higher conversion efficiency, then the air is used to provide heat for air-to-water heat exchanger to use the lower temperature energy in Rankine cycle effectively. Besides, feed water of Rankine cycle is used to cool the Stirling engines to recycle the heat wasted conventionally.

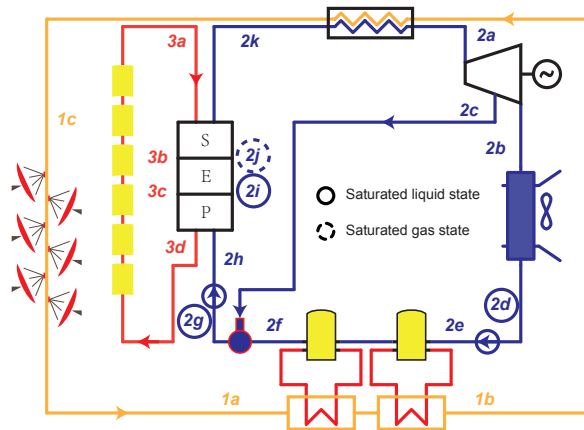


Figure 6-1 Sketch of the cascade system

State points of different fluids are marked on the sketch. The number indicates the type of the fluid, the letter indicates the state point of the fluid. State points with solid circle indicate saturated liquid states ( $x = 0$ ), and with dotted circle indicates saturated gas states ( $x = 1$ ). Figure 6-2a shows the  $T - s$  diagram of the water circuit in the cascade system. In this Rankine cycle, the heat provided in process  $2e-2f$  comes from the Stirling engines, which increases the power of Rankine cycle. Figure 6-2b shows the heat transfer diagram of

this process.

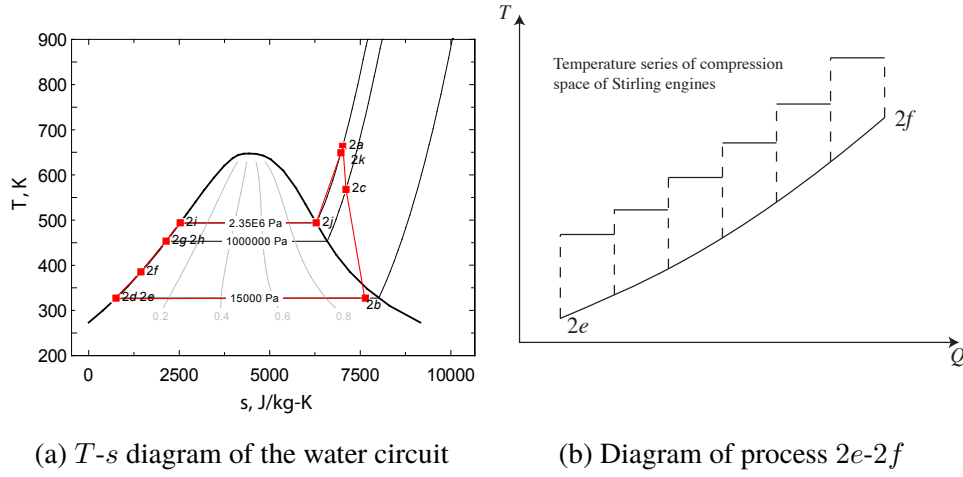


Figure 6-2 Diagrams of water circuit and  $2e$ - $2f$  process

To build the cascade system model, several simplifying assumptions are made:

- Steady state at nominal load of the system is analysed.
- Pressure drop due to flow is negligible.
- The leak of working fluid in the pipes is neglected.
- Same isentropic efficiency of steam turbine with different loads and in different stages.
- Heat loss that occurs from the tube to the atmosphere is not considered.
- There is no heat loss to the environment for Stirling engines.
- Simple models are used of some processes and equipments.
- A symmetrical regenerator behavior is assumed so that a single effectiveness can be defined as  $e = (T_R - T_L)/(T_H - T_L)$ .<sup>[80,81]</sup>
- A linear temperature profile across the regenerator exists, the mean effective temperature  $T_R = (T_H - T_L)/\ln(T_H/T_L)$ .<sup>[88,89]</sup>

## 6.2 Determination of system parameters

## 6.3 System simulation

## 6.4 Stand-alone system selection

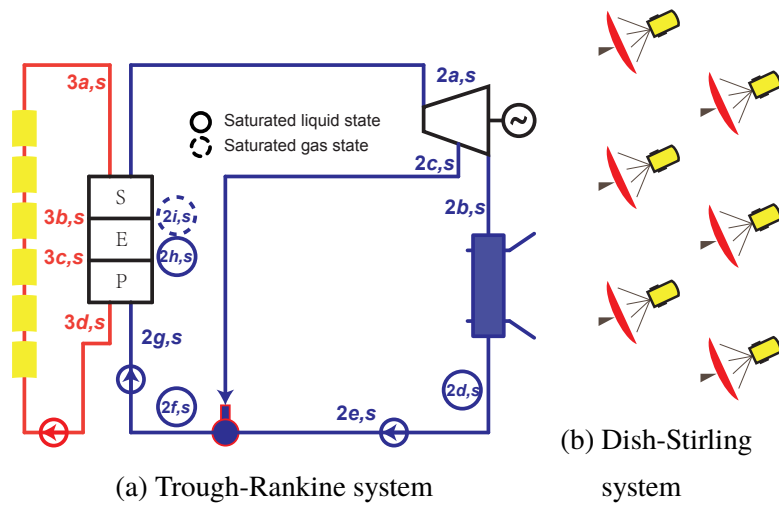


Figure 6-3 Sketch of the stand-alone systems

Figure 6-3 shows the sketch of the stand-alone systems. These two stand-alone systems were developed for comparison. They use the same dish collectors and trough collectors with the same thermal efficiencies.

### 6.4.1 Stand-alone trough-Rankine system

Steam turbine has the same main parameters and isentropic efficiency with that of the cascade system. Working pressure of deaerator is the same of the cascade system. So parameters of state  $2b,s$  and  $2c,s$  in Figure 6-3 of the steam turbine can be obtained by  $\eta_{i,tb} = (h_{2a,s} - h_{2b,s}) / (h_{2a,s} - h_{i,2b,s}) = (h_{2a,s} - h_{2c,s}) / (h_{2a,s} - h_{i,2c,s})$ .

The output power of steam turbine  $P_{tb,s} = (1 - y_s) \dot{m}_{2,s} (h_{2a,s} - h_{2b,s}) + y_s \dot{m}_{2,s} (h_{2a,s} - h_{2c,s})$ .

The output power of generator  $P_{ge,s} = P_{tb,s} \eta_{ge}$ .

The total power of pumps  $P_{pu,s} = (1 - y_s) \dot{m}_{2,s} (h_{2e,s} - h_{2d,s}) + \dot{m}_{2,s} (h_{2g,s} - h_{2f,s})$ .

Heat injected in the water circuit  $Q_{2,s} = \dot{m}_{2,s} (h_{2a,s} - h_{2g,s})$ .

The generator efficiency is the same of that in the cascade system, and the efficiency of Rankine cycle can be expressed as  $\eta_{rk,s} = (P_{tb,s} - P_{pu,s}/\eta_{ge})/Q_{2,s}$ .

#### **6.4.2 Stand-alone dish-Stirling system**

In the stand-alone dish-Stirling system, Stirling engines with the same number of dish collectors are directly put on the focuses of the dish collectors. Water is used for cooling the Stirling engines.  $T_{H,s}$  is chosen to be equal to outlet temperature of air in dish receiver.  $T_{L,s}$  is chosen to be 310 K, the default expansion temperature in Fraser's dissertation<sup>[2]</sup> for the calculation of 4-95 NKII engine.  $k$  and  $\gamma$  are chosen the same value as that of the Stirling engines in the cascade system.

The power of Stirling engines  $P_{sea,s} = n_{dc}A_{dc}I_r\eta_{dc}\eta_{sea,s}$ .

### **6.5 Comparison with stand-alone system**

### **6.6 System analysis**



## **Chapter 7 Conclusion and outlook**

### **7.1 Conclusion**

### **7.2 Innovation**

### **7.3 Outlook**

## **Acknowledge**

This is the acknowledgement part.

## Bibliography

- [1] Babaelahi M, Sayyaadi H. A new thermal model based on polytropic numerical simulation of Stirling engines. *Applied Energy*, 2015, 141:143 – 159.
- [2] MARTINI W R. Stirling engine design manual, 2nd edition. Technical report, Martini Engineering, Richland, WA (USA), 1983.
- [3] Renewables 2016 Global Status Report. [http://www.ren21.net/wp-content/uploads/2016/10/REN21\\_GSR2016\\_FullReport\\_en\\_11.pdf](http://www.ren21.net/wp-content/uploads/2016/10/REN21_GSR2016_FullReport_en_11.pdf). Accessed: 2017-05-04.
- [4] International Energy Agency (2014). [http://www.iea.org/publications/freepublications/publication/TechnologyRoadmapSolarPhotovoltaicEnergy\\_2014edition.pdf](http://www.iea.org/publications/freepublications/publication/TechnologyRoadmapSolarPhotovoltaicEnergy_2014edition.pdf). Accessed: 2017-05-04.
- [5] Price H, Lupfert E, Kearney D, et al. Advances in Parabolic Trough Solar Power Technology. *Journal of Solar Energy Engineering*, 2002, 124(2):109–125.
- [6] Padilla R V, Demirkaya G, Goswami D Y, et al. Heat transfer analysis of parabolic trough solar receiver. *Applied Energy*, 2011, 88(12):5097 – 5110.
- [7] Mohamad A, Orfi J, Alansary H. Heat losses from parabolic trough solar collectors. *International Journal of Energy Research*, 2014, 38(1):20–28.
- [8] Guo J, Huai X, Liu Z. Performance investigation of parabolic trough solar receiver. *Applied Thermal Engineering*, 2016, 95:357 – 364.
- [9] Guo J, Huai X. Multi-parameter optimization design of parabolic trough solar receiver. *Applied Thermal Engineering*, 2016, 98:73 – 79.
- [10] Padilla R V, Fontalvo A, Demirkaya G, et al. Exergy analysis of parabolic trough solar receiver. *Applied Thermal Engineering*, 2014, 67(1-2):579 – 586.
- [11] Huang W, Hu P, Chen Z. Performance simulation of a parabolic trough solar collector. *Solar Energy*, 2012, 86(2):746 – 755.
- [12] Wang J, Wang J, Bi X, et al. Performance Simulation Comparison for Parabolic Trough Solar Collectors in China. *International Journal of Photoenergy*, 2016, 2016(18):1–16.
- [13] Al-Sulaiman F A. Exergy analysis of parabolic trough solar collectors integrated with combined steam and organic Rankine cycles. *Energy Conversion and Management*, 2014, 77:441 – 449.
- [14] Hachicha A, Rodriguez I, Capdevila R, et al. Heat transfer analysis and numerical simulation of a parabolic trough solar collector. *Applied Energy*, 2013, 111:581 – 592.
- [15] Ashouri M, Vandani A M K, Mehrpooya M, et al. Techno-economic assessment of a Kalina cycle driven by a parabolic Trough solar collector. *Energy Conversion and Management*, 2015, 105:1328 – 1339.
- [16] Guo S, Liu D, Chu Y, et al. Real-time dynamic analysis for complete loop of direct steam generation solar trough collector. *Energy Conversion and Management*, 2016, 126:573 – 580.
- [17] Bader R, Pedretti A, Barbato M, et al. An air-based corrugated cavity-receiver for solar parabolic

- trough concentrators. *Applied Energy*, 2015, 138:337 – 345.
- [18] Good P, Ambrosetti G, Pedretti A, et al. An array of coiled absorber tubes for solar trough concentrators operating with air at 600°C and above. *Solar Energy*, 2015, 111:378 – 395.
  - [19] Boukelia T, Arslan O, Mecibah M. ANN-based optimization of a parabolic trough solar thermal power plant. *Applied Thermal Engineering*, 2016, 107:1210 – 1218.
  - [20] Kaloudis E, Papanicolaou E, Belessiotis V. Numerical simulations of a parabolic trough solar collector with nanofluid using a two-phase model. *Renewable Energy*, 2016, 97:218 – 229.
  - [21] Tan L, Ji X, Li M, et al. The experimental study of a two-stage photovoltaic thermal system based on solar trough concentration. *Energy Conversion and Management*, 2014, 86:410 – 417.
  - [22] Al-Sulaiman F A, Hamdullahpur F, Dincer I. Performance assessment of a novel system using parabolic trough solar collectors for combined cooling, heating, and power production. *Renewable Energy*, 2012, 48:161 – 172.
  - [23] Lobon D H, Valenzuela L, Baglietto E. Modeling the dynamics of the multiphase fluid in the parabolic-trough solar steam generating systems. *Energy Conversion and Management*, 2014, 78:393 – 404.
  - [24] Xu C, Chen Z, Li M, et al. Research on the compensation of the end loss effect for parabolic trough solar collectors. *Applied Energy*, 2014, 115:128 – 139.
  - [25] Liu Q, Yang M, Lei J, et al. Modeling and optimizing parabolic trough solar collector systems using the least squares support vector machine method. *Solar Energy*, 2012, 86(7):1973 – 1980.
  - [26] Blázquez R, Carballo J, Silva M. Optical design and optimization of parabolic dish solar concentrator with a cavity hybrid receiver. *AIP Conference Proceedings*, 2016, 1734(1).
  - [27] Craig O O, Dobson R T. Parabolic solar cooker: Cooking with heat pipe vs direct spiral copper tubes. *AIP Conference Proceedings*, 2016, 1734(1).
  - [28] Qianjun M, Ming X, Yong S, et al. Study on solar photo-thermal conversion efficiency of a solar parabolic dish system. *Environmental Progress & Sustainable Energy*, 2014, 33(4):1438–1444.
  - [29] Mawire A, Taole S H. Experimental energy and exergy performance of a solar receiver for a domestic parabolic dish concentrator for teaching purposes. *Energy for Sustainable Development*, 2014, 19:162 – 169.
  - [30] Reddy K, Vikram T S, Veershetty G. Combined heat loss analysis of solar parabolic dish – modified cavity receiver for superheated steam generation. *Solar Energy*, 2015, 121:78 – 93. {ISES} Solar World Congress 2013 (SWC2013) Special Issue.
  - [31] Reddy K, Natarajan S K, Veershetty G. Experimental performance investigation of modified cavity receiver with fuzzy focal solar dish concentrator. *Renewable Energy*, 2015, 74:148 – 157.
  - [32] Vikram T S, Reddy K. Investigation of convective and radiative heat losses from modified cavity based solar dish steam generator using {ANN}. *International Journal of Thermal Sciences*, 2015, 87:19 – 30.
  - [33] Sagade A A. Experimental investigation of effect of variation of mass flow rate on performance of parabolic dish water heater with non-coated receiver. *International Journal of Sustainable Energy*, 2015, 34(10):645–656.

- [34] Skouri S, Bouadila S, Salah M B, et al. Comparative study of different means of concentrated solar flux measurement of solar parabolic dish. *Energy Conversion and Management*, 2013, 76:1043 – 1052.
- [35] Uma Maheswari C, Meenakshi Reddy R. CFD Analysis of a Solar Parabolic Dish. *Applied Mechanics & Materials*, 2015, 787:280–284.
- [36] Patil P N, Khandekar M A, Patil S N. Automatic dual-axis solar tracking system for parabolic dish. in: *Proceedings of 2016 2nd International Conference on Advances in Electrical, Electronics, Information, Communication and Bio-Informatics (AEEICB)*, Feb, 2016, 699-703.
- [37] PAVLOVIĆ S R, STEFANOVIĆ V P, SULJKOVIĆ S H. OPTICAL MODELING OF A SOLAR DISH THERMAL CONCENTRATOR BASED ON SQUARE FLAT FACETS. *Thermal Science*, 2014, 18(3):989 – 998.
- [38] Besarati S M, Yogi Goswami D. A computationally efficient method for the design of the heliostat field for solar power tower plant. *Renewable Energy*, 2014, 69:226–232.
- [39] El-Haroun A. Investigation of a Novel Combination for Both Solar Chimney and Solar Tower Systems. *Journal of Energy Engineering*, 2015, page 04015042.
- [40] Franchini G, Perdichizzi A, Ravelli S, et al. A comparative study between parabolic trough and solar tower technologies in Solar Rankine Cycle and Integrated Solar Combined Cycle plants. *Solar Energy*, 2013, 98, Part C:302 – 314.
- [41] Kim J, Kim J S, Stein W. Simplified heat loss model for central tower solar receiver. *Solar Energy*, 2015, 116:314 – 322.
- [42] Lara-Cerecedo L O, Moreno-Cruz I, Pitalúa-Díaz N, et al. Modeling of Drift Effects on Solar Tower Concentrated Flux Distributions. *International Journal of Photoenergy*, 2016, 2016:1–9.
- [43] Wei X, Lu Z, Wang Z, et al. A new method for the design of the heliostat field layout for solar tower power plant. *Renewable Energy*, 2010, 35(9):1970–1975.
- [44] Wei X, Lu Z, Yu W, et al. A new code for the design and analysis of the heliostat field layout for power tower system. *Solar Energy*, 2010, 84(4):685–690.
- [45] Xu E, Yu Q, Wang Z, et al. Modeling and simulation of 1 MW DAHAN solar thermal power tower plant. *Renewable Energy*, 2011, 36(2):848–857.
- [46] Xu E, Wang Z, Wei G, et al. Dynamic simulation of thermal energy storage system of Badaling 1 MW solar power tower plant. *Renewable Energy*, 2012, 39(1):455–462.
- [47] Suzuki A. Cascade connection of solar collectors for effective energy gain. *Journal of Solar Energy Engineering Transactions of the Asme*, 1986, 108(3):172–177.
- [48] Oshida I, Suzuki A. Optical Cascade Heat-Collection for Effective Solar Energy Gain. *Journal of Solar Energy Engineering*, 1987, 109(4):298–302.
- [49] Kribus A, Doron P, Rubin R, et al. A Multistage Solar Receiver:: The Route To High Temperature. *Solar Energy*, 1999, 67(1–3):3 – 11.
- [50] Collado F J, Guallar J. Two-stages optimised design of the collector field of solar power tower plants. *Solar Energy*, 2016, 135:884 – 896.
- [51] Reddy K S, Sendhil Kumar N. Convection and surface radiation heat losses from modified

- cavity receiver of solar parabolic dish collector with two-stage concentration. *Heat and Mass Transfer*, 2009, 45(3):363–373.
- [52] Mills D. Two-stage solar collectors approaching maximal concentration. *Solar Energy*, 1995, 54(1):41 – 47.
- [53] Gordon J M, Saltiel C. Analysis and Optimization of a Multi-Stage Solar Collector System. *Journal of Solar Energy Engineering*, 1986, 108(3):192–198.
- [54] Desai N B, Bandyopadhyay S. Integration of parabolic trough and linear Fresnel collectors for optimum design of concentrating solar thermal power plant. *Clean Technologies and Environmental Policy*, 2015, 17(7):1945–1961.
- [55] Coco-Enríquez L, Muñoz-Antón J, Martínez-Val J. Integration between direct steam generation in linear solar collectors and supercritical carbon dioxide Brayton power cycles. *International Journal of Hydrogen Energy*, 2015, 40(44):15284 – 15300. The 4th International Conference on Nuclear and Renewable Energy Resources (NURER2014), 26-29 October 2014, Antalya, Turkey.
- [56] Li Y, Yang Y. Thermodynamic analysis of a novel integrated solar combined cycle. *Applied Energy*, 2014, 122:133 – 142.
- [57] Behar O, Khellaf A, Mohammedi K, et al. A review of integrated solar combined cycle system (ISCCS) with a parabolic trough technology. *Renewable and Sustainable Energy Reviews*, 2014, 39(0):223–250.
- [58] Gülen S C. Second Law Analysis of Integrated Solar Combined Cycle Power Plants. *Journal of Engineering for Gas Turbines and Power*, 2015, 137(5):51701.
- [59] Shaaban S. Analysis of an integrated solar combined cycle with steam and organic Rankine cycles as bottoming cycles. *Energy Conversion and Management*, 2016, 126:1003–1012.
- [60] Alqahtani B J, Patiño-Echeverri D. Integrated Solar Combined Cycle Power Plants: Paving the way for thermal solar. *Applied Energy*, 2016, 169:927 – 936.
- [61] Manente G. High performance integrated solar combined cycles with minimum modifications to the combined cycle power plant design. *Energy Conversion and Management*, 2016, 111:186 – 197.
- [62] Rovira A, Barbero R, Montes M J, et al. Analysis and comparison of Integrated Solar Combined Cycles using parabolic troughs and linear Fresnel reflectors as concentrating systems. *Applied Energy*, 2016, 162:990–1000.
- [63] Turchi C S, Ma Z. Co-located gas turbine/solar thermal hybrid designs for power production. *Renewable Energy*, 2014, 64:172 – 179.
- [64] Mukhopadhyay S, Ghosh S. Solar tower combined cycle plant with thermal storage: energy and exergy analyses. *Advances in Energy Research*, 2016, 4(1):29–45.
- [65] Li J, Li P, Pei G, et al. Analysis of a novel solar electricity generation system using cascade Rankine cycle and steam screw expander. *Applied Energy*, 2016, 165:627–638.
- [66] Bahari S S, Sameti M, Ahmadi M H, et al. Optimisation of a combined Stirling cycle–organic Rankine cycle using a genetic algorithm. *International Journal of Ambient Energy*, 2016, 37(4):398–402.

- [67] Abbin J P, Leuenberger W R. Program CYCLE: a Rankine cycle analysis routine. 1977.
- [68] Bilgen E, Rheault J. Solar chimney power plants for high latitudes. *Solar Energy*, 2005, 79(5):449 – 458.
- [69] Dudley V E, Kolb G J, Mahoney A R, et al. Test results: SEGS LS-2 solar collector. Nasa Sti/recon Technical Report N, 1994, 96(4):2506–2514.
- [70] Romero-Alvarez M, Zarza E. Concentrating solar thermal power. *Efficiency and Renewable Energy*, 2007.
- [71] Adkins D R. Control strategies and hardware used in solar thermal applications. Nasa Sti/recon Technical Report N, 1987, 88.
- [72] Coronel P, Sandeep K. Heat transfer coefficient in helical heat exchangers under turbulent flow conditions. *International Journal of Food Engineering*, 2008, 4(1).
- [73] Serth R W. Process heat transfer principles and applications. Amsterdam; London: Elsevier Academic Press, 2007.
- [74] Churchill S W, Bernstein M. A Correlating Equation for Forced Convection From Gases and Liquids to a Circular Cylinder in Crossflow. *Journal of Heat Transfer*, 1977, 99(2):300–306.
- [75] Ma R Y. Wind Effects on Convective Heat Loss From a Cavity Receiver for a Parabolic Concentrating Solar Collector. Sandia National Laboratory, 1993, SAND92-7293(September).
- [76] Wu S Y, Xiao L, Cao Y, et al. Convection heat loss from cavity receiver in parabolic dish solar thermal power system: A review. *Solar Energy*, 2010, 84(8):1342 – 1355.
- [77] Leibfried U, Ortjohann J. Convective Heat Loss from Upward and Downward-Facing Cavity Solar Receivers: Measurements and Calculations. *Journal of Solar Energy Engineering*, 1995, 117(2):75–84.
- [78] Koenig A, Marvin M. Convection heat loss sensitivity in open cavity solar receivers. Technical report, Department of Energy, USA, 1981.
- [79] Stine W B, Diver R B. A compendium of solar dish/Stirling technology. Technical report, DTIC Document, 1994.
- [80] Formosa F, Despesse G. Analytical model for Stirling cycle machine design. *Energy Conversion and Management*, 2010, 51(10):1855–1863.
- [81] Juhasz A. A mass computation model for lightweight brayton cycle regenerator heat exchangers. in: *Proceedings of 8th Annual International Energy Conversion Engineering Conference*, 2010.
- [82] Duan C, Wang X, Shu S, et al. Thermodynamic design of Stirling engine using multi-objective particle swarm optimization algorithm. *Energy Conversion & Management*, 2014, 84:88–96.
- [83] Urieli I, Berchowitz D M. Stirling cycle engine analysis. Bristol: A. Hilger, 1984.
- [84] Heywood, JohnB. Internal combustion engine fundamentals. Amsterdam; London: McGraw-Hill, 1988.
- [85] Strauss J M, Dobson R T. Evaluation of a second order simulation for Sterling engine design and optimisation. *Journal of Energy in Southern Africa*, 2010, 21(2):17–29.
- [86] Timoumi Y, Tlili I, Nasrallah S B. Design and performance optimization of GPU-3 Stirling engines. *Energy*, 2008, 33(7):1100 – 1114.

- [87] Hosseinzade H, Sayyaadi H, Babaelahi M. A new closed-form analytical thermal model for simulating Stirling engines based on polytropic-finite speed thermodynamics. *Energy Conversion and Management*, 2015, 90:395 – 408.
- [88] Der Minassians A. *Stirling Engines for Low-temperature Solar-thermal-electric Power Generation*. University of California, Berkeley, 2007.
- [89] Cavazzuti M. *Optimization Methods: From Theory to Design Scientific and Technological Aspects in Mechanics*. Springer Berlin Heidelberg, 2012.
- [90] Hooshang M, Moghadam R A, AlizadehNia S. Dynamic response simulation and experiment for gamma-type Stirling engine. *Renewable Energy*, 2016, 86:192 – 205.
- [91] Rovira A, Montes M J, Valdes M, et al. Energy management in solar thermal power plants with double thermal storage system and subdivided solar field. *Applied Energy*, 2011, 88(11):4055 – 4066.



## Appendix A Heat transfer under constant temperature

Assuming  $U, T_c, q_m, c_p$  to be constant, for given  $T_i$ ,

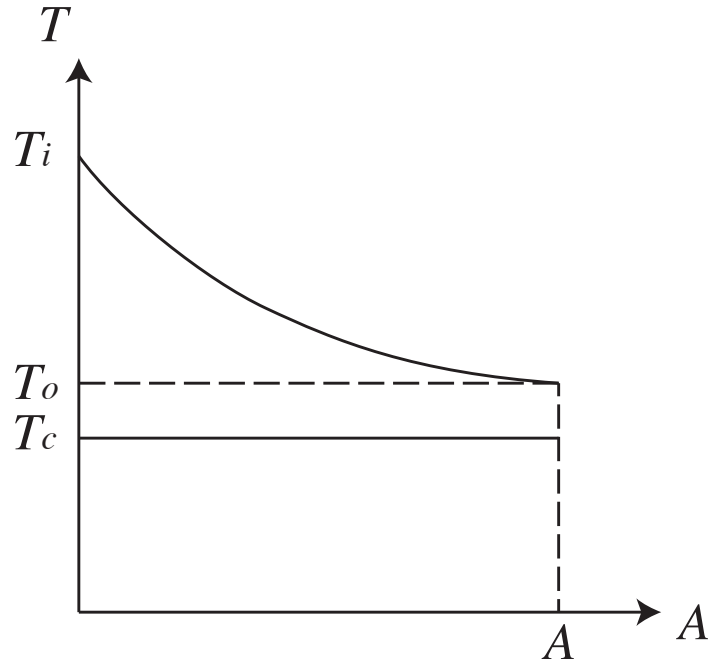


Figure 1-1 Diagram of heat transfer under constant temperature

For  $A(x) = Px$ ,  $x$  from 0 to  $L$ , while  $T(x)$  from  $T_i$  to  $T_o$ ,

$$q_m c_p dT(x) = (T_c - T(x))UPdx \quad (\text{A.1})$$

so

$$\frac{dT(x)}{dx} = -\frac{UP}{q_m c_p}(T(x) - T_c) \quad (\text{A.2})$$

$$T_g(x) = T_p(x) + T_h(x) \quad (\text{A.3})$$

where  $T_g(x)$  is the general solution,  $T_p(x)$  is the particular solution,  $T_h(x)$  is the homogeneous solution.

$$-\frac{UP}{q_m c_p}(T_p(x) - T_c) = 0 \quad (\text{A.4})$$

$$T_p(x) = T_c \quad (\text{A.5})$$

$$\frac{dT_h(x)}{dx} = -\frac{UP}{q_m c_p}T_h(x) \quad (\text{A.6})$$

$$\int_{T_h(x)=T_h(0)}^{T_h(x)=T_h(L)} \frac{dT_h(x)}{T_h(x)} = -\int_{x=0}^{x=L} \frac{UP}{q_m c_p} dx \quad (\text{A.7})$$

$$\frac{T_h(L)}{T_h(0)} = \exp\left(-\frac{UPL}{q_m c_p}\right) \quad (\text{A.8})$$

that is

$$\frac{T_g(L) - T_p(L)}{T_g(0) - T_p(0)} = \exp\left(-\frac{UA}{q_m c_p}\right) \quad (\text{A.9})$$

$$\frac{T_o - T_c}{T_i - T_c} = \exp\left(-\frac{UA}{q_m c_p}\right) \quad (\text{A.10})$$

## Appendix B Thermal gradient under constant heat flux

Assuming  $U, T_c, \dot{m}, c_p, q''$  to be constant, for given  $T_i$ ,

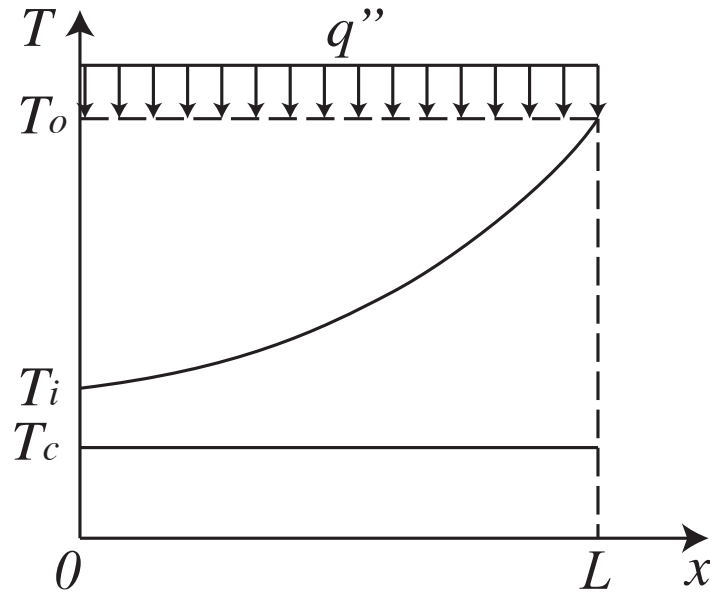


Figure 2-1 Diagram of heat transfer with one constant temperature heat source and constant heat flux

For  $A(x) = Px$ ,  $x$  from 0 to  $L$ , while  $T(x)$  from  $T_i$  to  $T_o$ ,

$$q_m c_p dT(x) = (T_c - T(x))UPdx + q''Pdx \quad (\text{B.1})$$

so

$$\frac{dT(x)}{dx} = -\frac{UP}{q_m c_p}T(x) + \frac{q''P + UPT_c}{q_m c_p} \quad (\text{B.2})$$

$$T_g(x) = T_p(x) + T_h(x) \quad (\text{B.3})$$

where  $T_g(x)$  is the general solution,  $T_p(x)$  is the particular solution,  $T_h(x)$  is the homogeneous solution.

$$-\frac{UP}{q_m c_p} T_p(x) + \frac{q''P + UPT_c}{q_m c_p} = 0 \quad (\text{B.4})$$

$$T_p(x) = T_c + \frac{q''}{U} \quad (\text{B.5})$$

$$\frac{dT_h(x)}{dx} = -\frac{UP}{q_m c_p} T_h(x) \quad (\text{B.6})$$

the same as Equation (A.6), so we have

$$\frac{T_g(L) - T_p(L)}{T_g(0) - T_p(0)} = \exp\left(-\frac{UA}{q_m c_p}\right) \quad (\text{B.7})$$

$$\frac{T_o - T_c - \frac{q''}{U}}{T_i - T_c - \frac{q''}{U}} = \exp\left(-\frac{UA}{q_m c_p}\right) \quad (\text{B.8})$$

## Appendix C Publication

- [1] Zhang Cheng, Kun Wang. International Conference on Power Engineering: ICOPE 2013: FEA simulation on the alignment of the shafts of three-fulcrum turbine.
- [2] Performance comparison of new and traditional arrangements of a dish-Stirling system
- [3] A multi-stage exergy-loss reduction system for solar parabolic trough power plants
- [4] Zhang Cheng, Zhang Yanping, Arauzo Inmaculada, Gao Wei, Zou Chongzhe. Cascade system using both trough system and dish system for power generation. *Energy Convers Manag* 2017;142:494–503. doi:10.1016/j.enconman.2017.03.073.
- [5] Thermal Modeling of a Pressurized Air Cavity Receiver for a Solar Dish Stirling System
- [6] A solar thermal cascade system, No. 201610806296.5
- [7] A flow control method used in a multi-stage heating system, No. 201610805604.2